

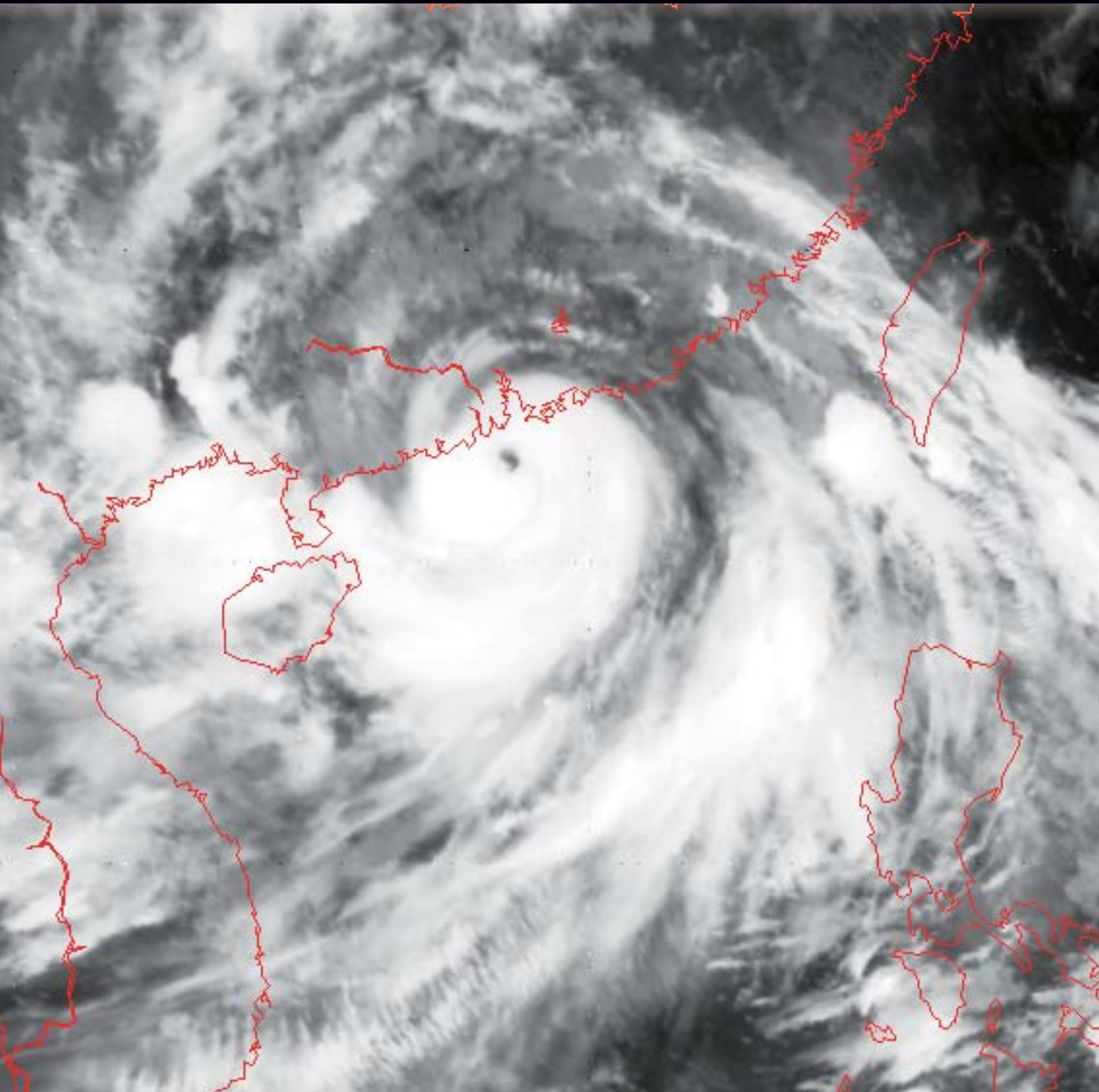
香港氣象學會

The Hong Kong Meteorological Society

Bulletin

VOLUME 22, 2012

ISSN 1024-4468



ISSN 1024-4468

The Hong Kong Meteorological Society Bulletin is the official organ of the Society, devoted to articles, editorials, news and views, activities and announcements of the Society.

Members are encouraged to send any articles, media items or information for publication in the Bulletin. For guidance see the information for contributors in the inside back cover.

Advertisements for products and/or services of interest to members of the Society are accepted for publication in the Bulletin.

For information on formats and rates please contact the Society secretary at the address opposite.

The Bulletin is copyright material.

Views and opinions expressed in the articles or any correspondence are those of the author(s) alone and do not necessarily represent the views and opinions of the Society.

Permission to use figures, tables, and brief extracts from this publication in any scientific or educational work is hereby granted provided that the source is properly acknowledged. Any other use of the material requires the prior written permission of the Hong Kong Meteorological Society.

The mention of specific products and/or companies does not imply there is any endorsement by the Society or its office bearers in preference to others which are not so mentioned.

Editorial Board

Dr. Wen Zhou (Editor-in-Chief)
Dr. David Lam
Mr. Clarence Fong
Mr. Terence Kung

SUBSCRIPTION RATES

Institutional rate: HK\$ 300 per volume
Individual rate: HK\$ 150 per volume



Published by

The Hong Kong Meteorological Society
c/o Hong Kong Observatory
134A Nathan Road
Kowloon, Hong Kong

Homepage

<http://www.meteorology.org.hk>

Contents

- ◀ **Editorial** 2
- ◀ **Numerical Simulation Studies on Severe Typhoon Vicente**..... 3-30
K.K. Hon, M.K. Or, and W.K. Wong
- ◀ **A Study of Tropical Cyclone Rainfall Distribution and Topographic Effect over Hong Kong**..... 31-40
H.Y. Yeung, P.W. Cheng and S.T. Chan
- ◀ **A Review of Climate Change Studies for Southern China** 41-52
S.M. Lee, J.L. Lau and S.M. Tong
- ◀ **Society Event** 53
Popular Science Lecture Series
- ◀ **Colour Figures**..... 54-56
Mascot Design Competition for Primary School Students
-
-

Editorial

The first paper by K.K. Hon, M.K. Or, and W.K. Wong of the Hong Kong Observatory is a modelling study on Severe Typhoon Vicente, which necessitated the issuance the Hurricane Signal No.10 in Hong Kong in 2012.

The second paper by H.Y. Yeung and S.T. Chan of the Hong Kong Observatory and P.W. Cheng of the City University of Hong Kong is a statistical study of the orographic enhancement of rainfall in Hong Kong due to tropical cyclones.

The third paper by S.M. Lee of the Hong Kong Observatory, J.L. Lau of the Guangdong Climate Center and S.M. Tong of the Macao Meteorological and Geophysical Bureau presents a review of the climate change studies conducted by the meteorological authorities of Guangdong, Macao and Hong Kong in recent years.

The Hong Kong Meteorological Society co-organized with the Hong Kong Science Museum to give a Popular Science Lecture Series in October 2012. Four professionals were invited to deliver talks on "Ocean, Sky and Earth—Meteorology in Our Life Daily" respectively and explain how weather and climate are affecting our daily life in different ways. Some photos of the talks are included in this issue.

A Mascot Design competition was organized in collaboration with the Hong Kong Society for Education in Art in 2012 for primary school students. The mascot can represent various weather phenomena, such as wind, cloud, rain, etc. The competition received very enthusiastic support from schools and many fascinating designs were received. The colour pages in the end of this issue show the winning entries of the competition.

About the cover

The cover is an Infra-red satellite imagery of Severe Typhoon Vicente near its peak intensity as it moved close to Hong Kong around midnight on 24 July 2012 (the satellite imagery was originally captured by MTSAT-2 of the Japan Meteorological Agency).

Numerical Simulation Studies on Severe Typhoon Vicente

K.K. Hon, M.K. Or, and W.K. Wong
Hong Kong Observatory

Abstract

Tropical cyclone Vicente (1208) entered the northern South China Sea on 21st July 2012, becoming quasi-stationary about 350 km south-southeast offshore of Hong Kong on the following day. Vicente gained northwestward momentum on the morning of the 23rd and gradually intensified while edging toward the coast of Guangdong. As Vicente acquired Severe Typhoon intensity and accelerated toward the Pearl River Estuary, the Observatory issued Hurricane Signal No. 10 in the wee hours of the 24th, the first since the direct hit by Typhoon York in September 1999. During the episode, winds of hurricane force were recorded over the southwestern waters of Hong Kong and on high ground. Rainbands associated with Vicente also brought rainfall exceeding 200 mm to many parts of the territory on the 23rd and 24th.

This paper studies, using the operational mesoscale model of the Observatory – the Non-Hydrostatic Model (NHM), the impact of model physical processes as well as assimilation of aircraft reconnaissance flight data by the Government Flying Service (GFS) on aspects of Vicente including forecast track, intensity, and structure as well as impacts on local weather. Model performance will also be validated against *in situ* and remote sensing measurements.

1. Background

Tropical cyclone (TC) Vicente (1208) formed as a tropical depression over the western North Pacific about 450 km northeast of Manila on 20th July 2012 and, under the steering of a subtropical ridge anchored south of Japan, entered the northern South China Sea on the 21st (Fig. 1). Vicente then became quasi-stationary about 350 km south-southeast offshore of Hong Kong on the following day but gained momentum northwestward on the morning of the 23rd and gradually intensified while edging toward the coast of Guangdong (Fig. 2).

As Vicente acquired Severe Typhoon intensity and accelerated toward the Pearl River Estuary (Fig. 3), the Observatory issued Hurricane Signal No. 10 in the wee hours of the 24th, the first since the direct hit by Typhoon York in September 1999. During the episode, winds of hurricane force were recorded over the southwestern waters of Hong Kong and on high ground. Rainbands associated with Vicente brought rainfall exceeding 200 mm to many parts of the territory on the 23rd and 24th (Fig. 4). Weather warnings issued by HKO during the passage of Vicente are listed in Table 1.

Given the hazards associated with sustained high winds and widespread torrential rainfall, accurate forecasting of intensity and spatial

structure of such high-impact weather systems is of socioeconomic importance. Quantification of associated risks would require accurate sampling of forecast uncertainties due to a combination of observational errors and model imperfections [1]. Indeed, perturbations in initial states are routinely introduced in ensemble prediction systems around the world with the aim of producing a range of possible future states for estimation of their relative likelihood [2]. The role of parameterised processes such as cumulus convection, cloud microphysics, and boundary layer exchange in forecast uncertainties has also gained increasing attention [3, 4].

For the case of tropical cyclones, representation of convective activities is of particular importance given the close connection between the strength of the core convection and TC intensity changes [5]. Various attempts have been reported including: intercomparison of individual parameterisation schemes [6] or combinations of schemes [7], the role of explicit and parameterised convection [8], and sensitivity to selected parameters of widely used schemes [9].

In addition, it has been established that transfer of heat and moisture at the air-sea boundary plays a key role in TC intensification [10], while frictional inflow due to surface drag

is of secondary importance, although interest in the latter has also revived [11]. Recent attempts at improving the representation of the TC boundary layer also include addressing the underestimation of heat and moisture transfer under high winds associated with saturation of surface momentum flux [12].

Keeping in view the developments in the understanding of forecast uncertainties in numerical models as well as of TC-related

physical processes, this paper will (i) explore, using the case of Vicente, the sensitivity of the forecast movement, intensity, and structure to cumulus parameterization; (ii) perform in-depth investigation of the observed intensity changes of Vicente through a combination of fine-tuned model settings with a view to improving operational forecasts; and (iii) discuss briefly the impact of aircraft reconnaissance flight data on the analysis and forecast of Vicente.

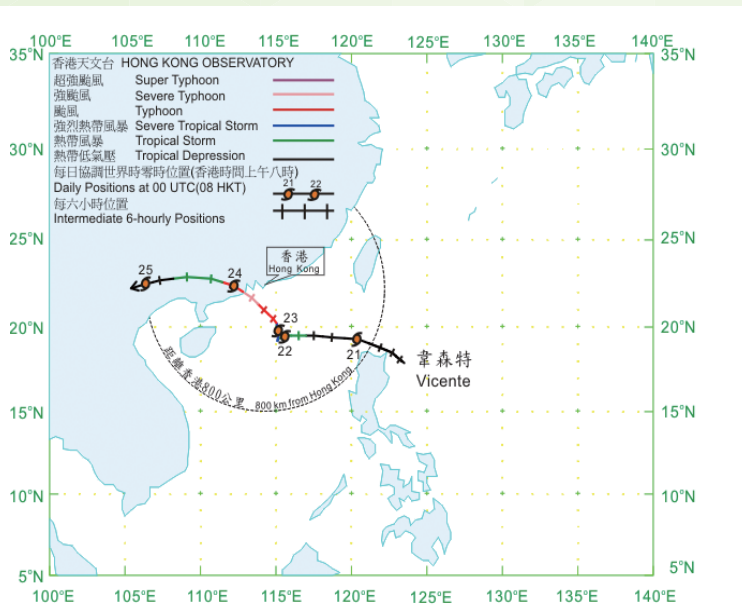


Fig. 1 Location and intensity of Vicente (1208) between 20th and 25th July 2012, based on HKO Best Track data

Tropical Cyclone Warning signal	Time of Issuance (HKT)
1	21 / 15:40
3	23 / 05:20
8 NE	23 / 17:40
9	23 / 23:20
10	24 / 00:45
8 SE	24 / 03:35
3	24 / 10:10
1	24 / 14:40
(Cancelled)	24 / 23:15

Thunderstorm Warning	
Issuance (HKT)	Cancellation (HKT)
21 / 14:45	21 / 19:15
21 / 21:25	22 / 00:00
22 / 11:35	22 / 17:00
24 / 00:15	24 / 05:15

Amber Rainstorm Warning	
Issuance (HKT)	Cancellation (HKT)
21 / 17:35	21 / 18:40
24 / 01:55	24 / 10:40

Landslip Warning	
Issuance (HKT)	Cancellation (HKT)
24 / 15:00	24 / 01:10

Special Announcement on Flooding in the Northern New Territories	
Issuance (HKT)	Cancellation (HKT)
24 / 01:55	24 / 12:25

Table 1 List of warning signals issued by the Observatory between 21st and 24th July, 2012.

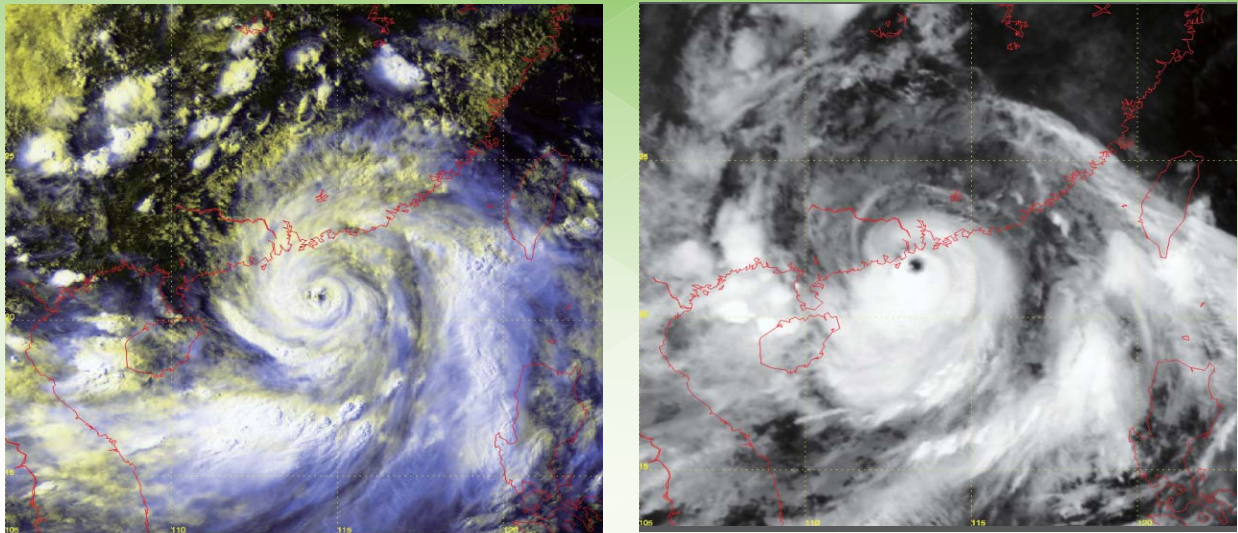


Fig. 2 MTSAT images of Vicente over the South China Sea when an eye first developed in the afternoon of 23rd July 2012 (left) after Vicente regained northwestward movement; and during closest approach at about 100 km southwest of the Observatory (right) in the wee hours of the 24th.

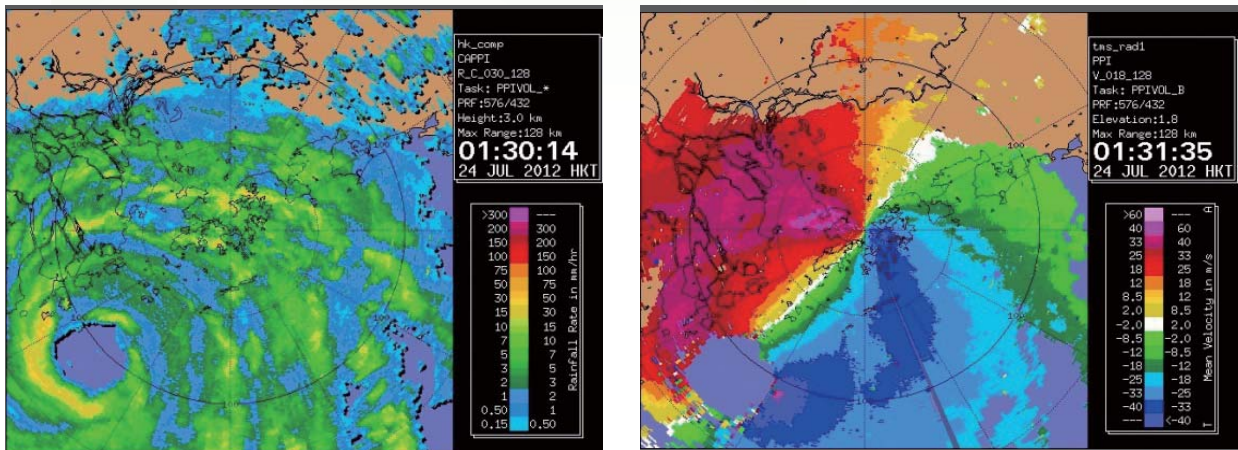


Fig. 3 128-km radar images of Vicente in the wee hours of 24th July 2012 showing: (left) a clear, circular eye around 100 km southwest of the Observatory; and (right) a region of low-level hurricane-force winds (in blue) approaching Hong Kong from the south.

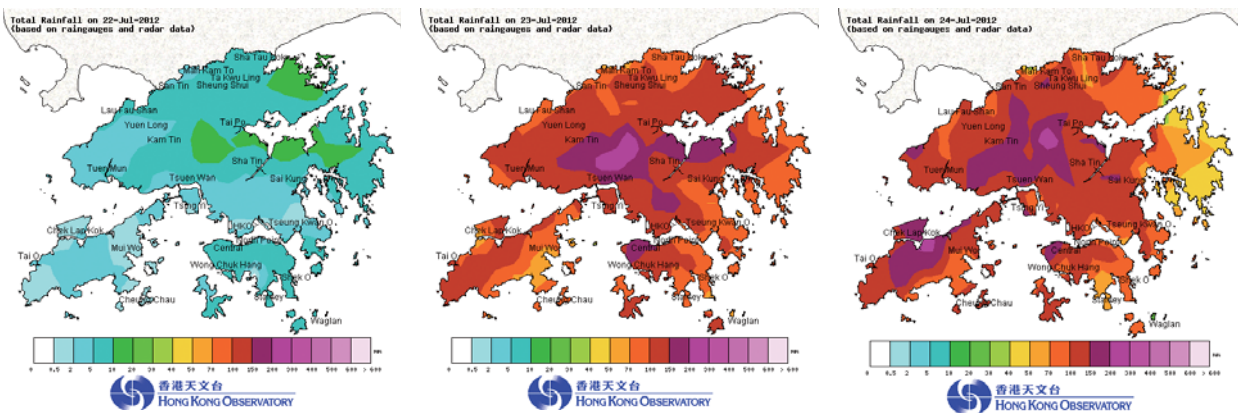


Fig. 4 Daily rainfall distribution in Hong Kong during passage of Vicente: 22nd (left), 23rd (middle), and 24th (right) July 2012. Most parts of the territory received 24-hourly rainfall exceeding 100 mm on both the 23rd and 24th.

2. Model Configuration and Method of Study

HKO maintains a mesoscale NWP suite, the Atmospheric Integrated Rapid-cycle (AIR) forecast model system [13], based on the Non-Hydrostatic Model (NHM) developed by JMA [14]. In particular, the Meso-NHM provides 3-hourly updated forecasts covering East Asia and the western North Pacific up to 72 hours ahead at 10-km resolution.

For the current study, a domain of 301 x 251 grid points, covering the region (8° N - 31° N), (103° E - 132° E) is employed (Fig. 5). At the same 10-km resolution, this is smaller than the domain of the operational Meso-NHM, which spans (7° N - 42° N), (90° E - 147° E). The effect of domain size on the evolution of Vicente, however, is found to be small through additional test runs (not shown) comparing both settings. This is further confirmed by results of later sections, where the full domain is again used. Vertically, a total of 50 hybrid-sigma levels is used with model top height about 22 km. Integration is performed at a time step of 30 s. For further details of model configuration, please refer to Table 1 of [13].

A 48-hour study period is chosen between 00 UTC on 22nd and 00 UTC on 24th July 2012, which covers the poleward turn early on the 23rd at the end of the quasi-stationary episode as well as the rapid intensification of Vicente 6 - 12 hours prior to landfall near Taishan, Guangdong, at around 20UTC on the 23rd. At an initial time of about 40 hours ahead, forecast confidence for the occurrence of high winds and torrential rainfall along the coast of Guangdong could provide valuable from the perspective of disaster mitigation.

Boundary conditions are obtained from the operational Meso-NHM run at the same initial time, i.e., 22/00UTC, which is in turn driven by outputs of JMA-GSM at 21/18UTC. Initial fields are provided by the operational JNoVA 3D-VAR analysis [13] at the corresponding hour. Sea surface temperature (SST) analysis also follows operational configuration, which utilises the latest available NCEP high-resolution analysis (RTG_SST_HR, 1/12o resolution, 21/00UTC).

“Actual” positions and intensities of Vicente are based on 3-hourly analyses operationally performed by HKO during TC passage.

Discrepancies with HKO Best Track Data, which are available only at 6-hour intervals, are small in terms of position and intensity. Forecast positions by NHM are objectively determined according to the centre of the associated vortex at 925 hPa. While a more sophisticated tracking algorithm with additional continuity constraints is in use at HKO [15], the current method benefits from simplicity and is not affected by distortions in surface pressure patterns after landfall. Forecasts by a multimodel ensemble track comprising global model outputs¹ of ECMWF, JMA, EGRR, and NCEP with equal weighting, referred to operationally at HKO, will be included for comparison.

As introduced in Section 1, the following aspects in relation to Vicente will be studied:

a. Sensitivity to cumulus parameterisation

At 10-km resolution, Meso-NHM employs an adapted version of the Kain-Fritsch (“KF”) scheme [16] for parameterisation of subgrid convection. Two key parameters include the “closure”—the fraction of convective available potential energy (CAPE) released during the process of convection—and the timescale at which this energy is consumed. A larger fraction of consumed CAPE leads to greater stabilisation of the atmospheric profile, generally bringing more intense precipitation, while low values reduce the contribution of parameterised convection. The influence of both of these parameters on model precipitation performance has been recognised in studies from other parts of the world [17, 9].

Section 3 describes the results of a set of 30 sensitivity experiments, covering a large range of CAPE closures and convection timescales, designed to emulate the uncertainties in the forecast track, intensity, and precipitation of Vicente due to imperfection in model convective processes. Model forecasts will be validated against various local and remote-sensing observations with an emphasis on effects on weather in Hong Kong.

b. Impact of model physics parameters in the operational Meso-NHM

It will be seen that, while considerable variability is exhibited in the above test runs, the spread so generated is still inadequate in capturing certain aspects of Vicente,

¹ Forecast positions at 12-hour intervals as disseminated through GTS bulletins are used. Forecast intensity by EGRR has not been available.

notably the continued intensification near the coast of Guangdong. About 15 additional experiments are therefore performed using a wider combination of model settings with a view to accurately reproducing the observed evolution of Vicente. These include the upper and lower bounds of characteristic parameters mentioned in (a), other physical parameters, and an improved surface scheme as well as alternative choices of convection and cloud physics.

Here the operational version of Meso-NHM is used with a longer forecast range of 60 hours until Vicente dissipated into a marginal tropical storm inland over southern China. This can help confirm the validity of the results from (a) under full model configuration. Section 4 discusses the effects on track forecasts and intensity changes from several selected runs as compared to the original operational version.

Mechanisms for the intensification of Vicente in one of the "optimally-tuned" model forecasts will also be discussed in detail.

c. *Effects of GFS flight reconnaissance observations*

Numerical experiments are also conducted to investigate the impact on the analysis and forecast of Meso-NHM of reconnaissance flight data collected by the Government Flying Service (GFS) of Hong Kong, which pertain to winds, temperature, relative humidity, and pressure. The model analysis time was chosen to be 22/06UTC using a 3-hour observation time window to assimilate the whole batch of flight observations at different levels. A model run using the routine 3DVAR analysis is taken as the control experiment. Results of these experiments are mentioned in Section 5.

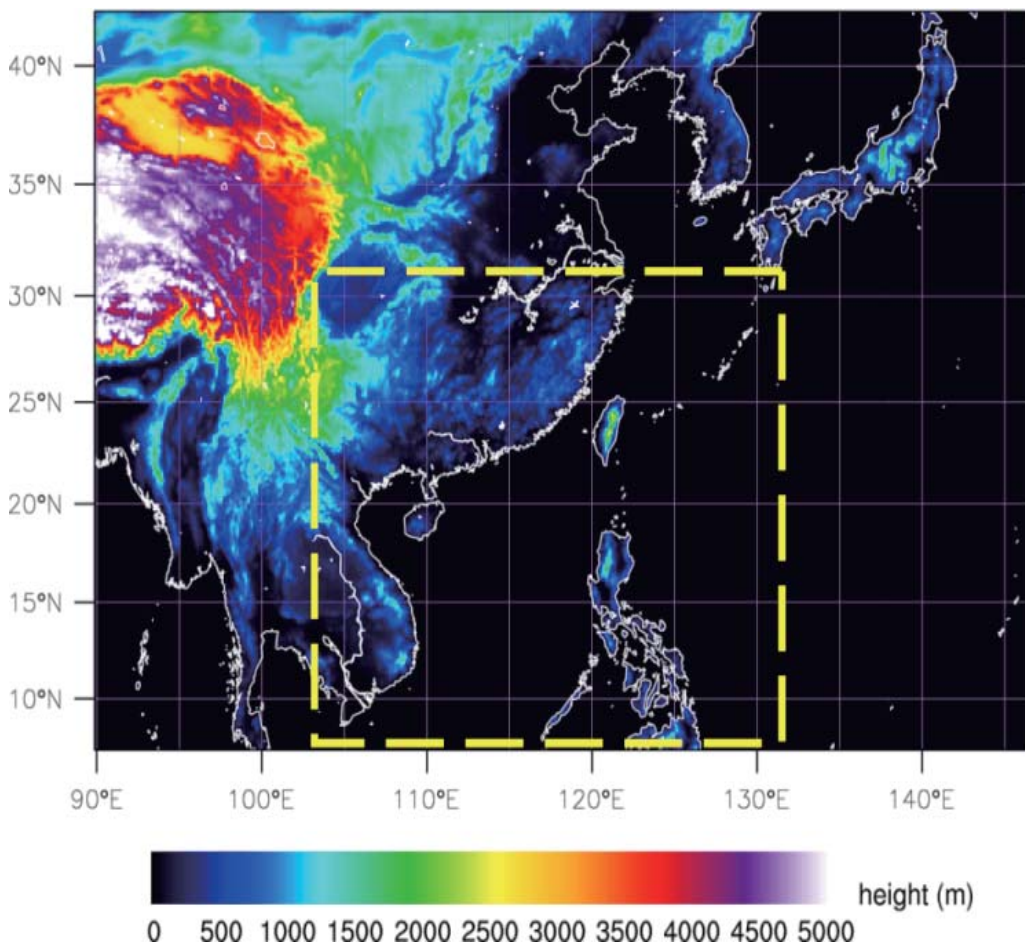


Fig. 5 Schematic diagram of the operational configuration of Meso-NHM (outer, 585 x 405 x 50 grid points). Reduced domain (301 x 251 x 50 grid points) for sensitivity tests on Vicente is highlighted in yellow.

3. Sensitivity to Cumulus Parameterisation

a. Impact on forecast track

Forecast positions at 3-hour intervals up to 48 hours ahead, i.e., 24/00UTC, by all 30 test runs are shown in Fig. 6. It can be seen that the northwestward motion of Vicente toward the coast of Guangdong is generally preserved among members, with an average positional error of only about 40 km at T+48 (blue bar in Fig. 7). In comparison, global models generally exhibit a westward or southward bias of 100–150 km and, with the exception of ECMWF, underestimate the translational speed of Vicente. Application of a range of KF parameters introduces a spread in both the movement speed and direction of the simulated TC that is capable of enveloping the analysed track of Vicente.

The decrease in mean forecast errors of NHM runs observed between T+24 and T+48, which may appear unnatural, can be attributed to the looping motion of Vicente during the period 22/03UTC to 22/21UTC, which is not resolved by any of the NHM runs. Decomposition of positional errors (Fig. 8) shows that forecasts at T+24 are indeed dominated by large, negative cross-track components of about 50–100 km, which results from the distance travelled by the simulated cyclone while Vicente remains quasi-stationary. As the TC begins moving northwestward in the subsequent hours, thereby “catching up” with the forecast positions, cross-track errors decrease accordingly at T+36, although NHM positions are still ahead by about 50 km on average. It is not until T+48 that forecast positions begin to exhibit both positive and negative along-track errors.

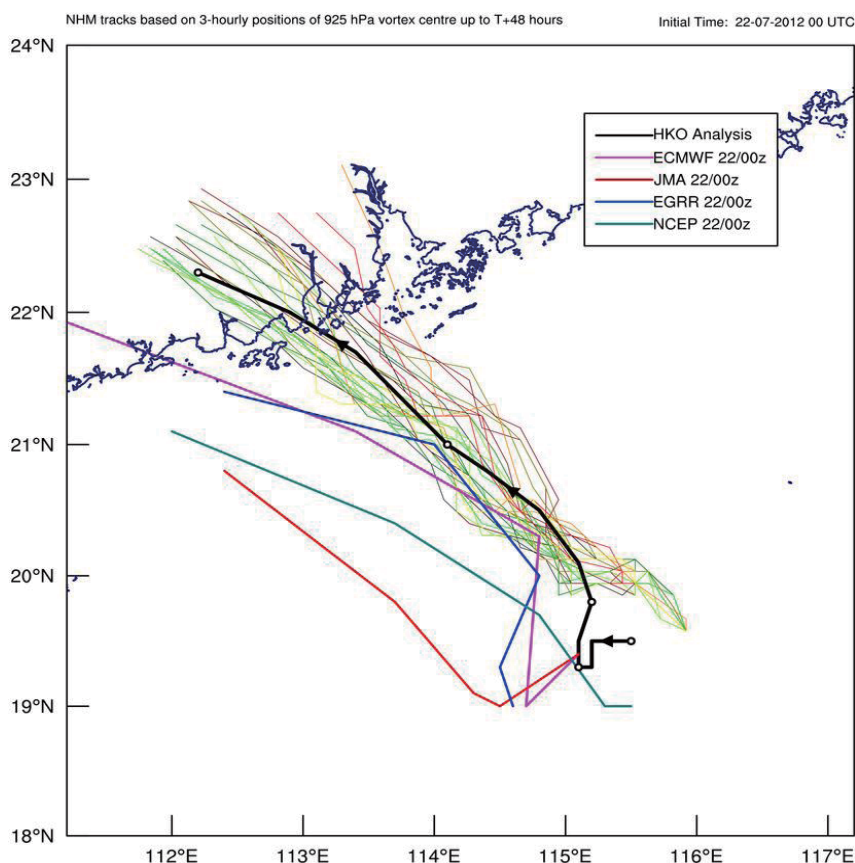


Fig. 6 Actual (HKO 3-hourly analysis, black, with positions at every 00UTC and 12UTC marked with circles) and forecast movement of Vicente by various configurations of NHM (3-hourly positions based on centre of 925 hPa vortex (thin, various colours) between 22nd and 24th July 2012. Forecast tracks by the global models of ECMWF (magenta), JMA (red), EGRR (blue), and NCEP (turquoise), also initialised at 00 UTC, 22nd July 2012 but at 12-hour intervals, are included for comparison.

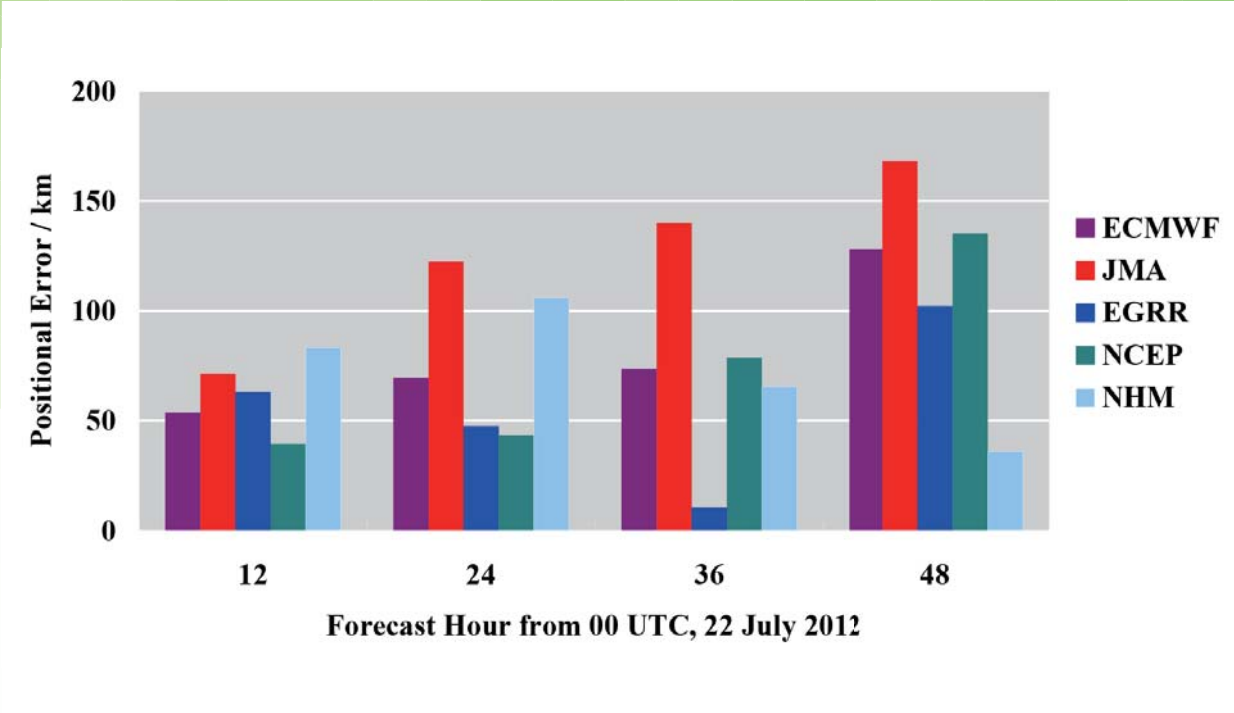


Fig. 7 Verification of forecasts, at 12-hour intervals, by ECMWF (magenta), JMA (red), EGRR (blue), and NCEP (turquoise) against HKO analysis positions of Vicente. Forecast positions by NHM (light blue) are here taken as the average of all test runs at equal weighting.

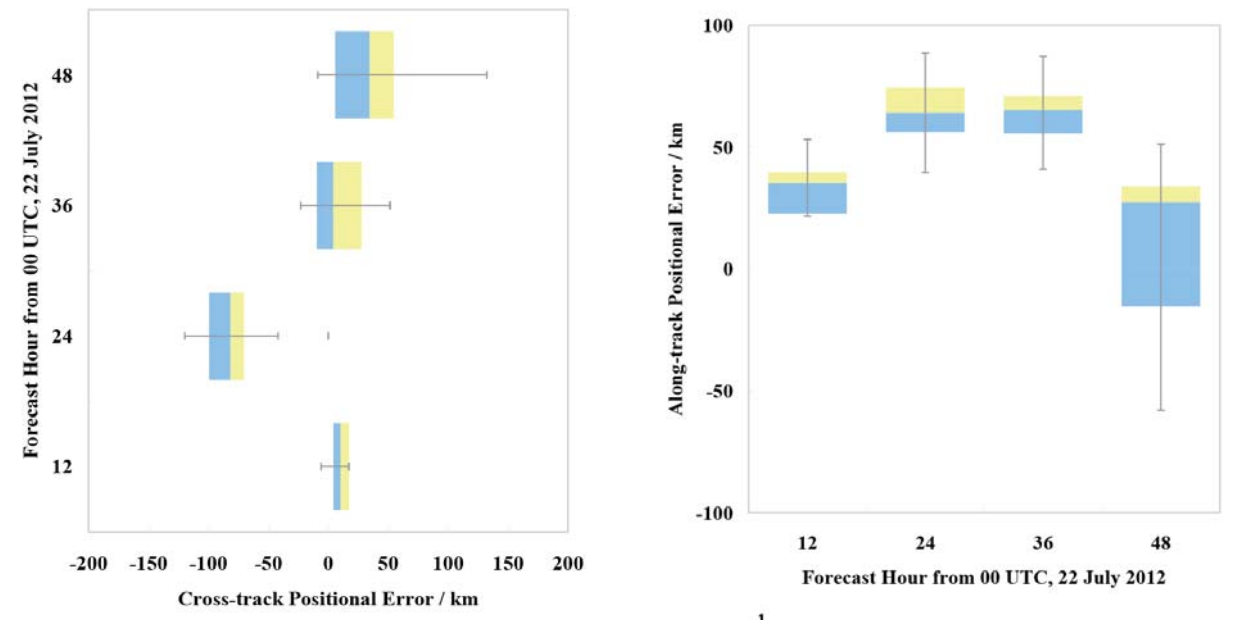


Fig. 8 Box-and-whisker plots (2nd and 3rd quartiles in blue and yellow, respectively) of track errors of NHM runs at 12-hourly intervals, decomposed into cross-track (left) and along-track (right) components. Movement direction of Vicente is calculated from HKO analysis positions at 6-hour intervals. Positive cross-track errors refer to a bias to the right of the motion vector.

b. Impact on intensity

The deepening trend of Vicente in the 30-hour period between 22/00UTC and 23/06UTC is well captured by most members, which, despite a spread in the rate of intensification, forecast pressure drops between 10 and 30 hPa and maximum winds between 50 and 80 knots at this stage (Fig. 9). Maximum intensity is attained between T+24 and T+36 in most test runs, which proves too early when compared to the actual timing of 23/15UTC (T+39). While the bulk of NHM runs are unable to reach the estimated minimum pressure of 950 hPa, more intense members do suggest lowest values around 955 hPa at T+36. Maximum winds follow a similar trend, with the most intense run peaking at 80 knots, only 5 knots short of the estimated 85 knots (Fig. 10).

By contrast, the intensification rate forecast by JMA and EGRR turns out to be too slow, although the slower movement of Vicente in both allows more sustained strengthening, with peak intensity occurring only at T+48, i.e., when in reality Vicente had already made landfall. On the other hand, while ECMWF underestimates the peak intensity by 20–30 knots, the forecast occurrence timing at around T+36, as well as the subsequent decay, closely

follows the observed trend.

Fig. 11 compares the distribution of surface winds in the vicinity of the Pearl River Estuary as estimated by the NOAA Multi-platform Satellite Wind product and forecast by selected runs of NHM at two points in time: when Vicente is about 150 km south of Hong Kong, and during its closest approach to the territory. At both times, the simulated wind fields show good correspondence with observations, particularly the extensive region of gale-force winds spanning 4–5 degrees of longitude and the structure close to the centre of Vicente. Although surface winds exceeding 81 knots have not been attained by any of the test runs, behaviour similar to the observed expansion of the hurricane radius between the two time steps is produced by NHM, in which an arc of hurricane-force winds attempts to wrap around the TC core but does not succeed.

The early weakening before landfall in NHM runs could be attributed to the decrease in surface moisture flux as a greater proportion of the TC moves over the land's surface. This issue will be addressed again in Section 4, where it will be demonstrated that the problem can be alleviated through a selected combination of model settings.

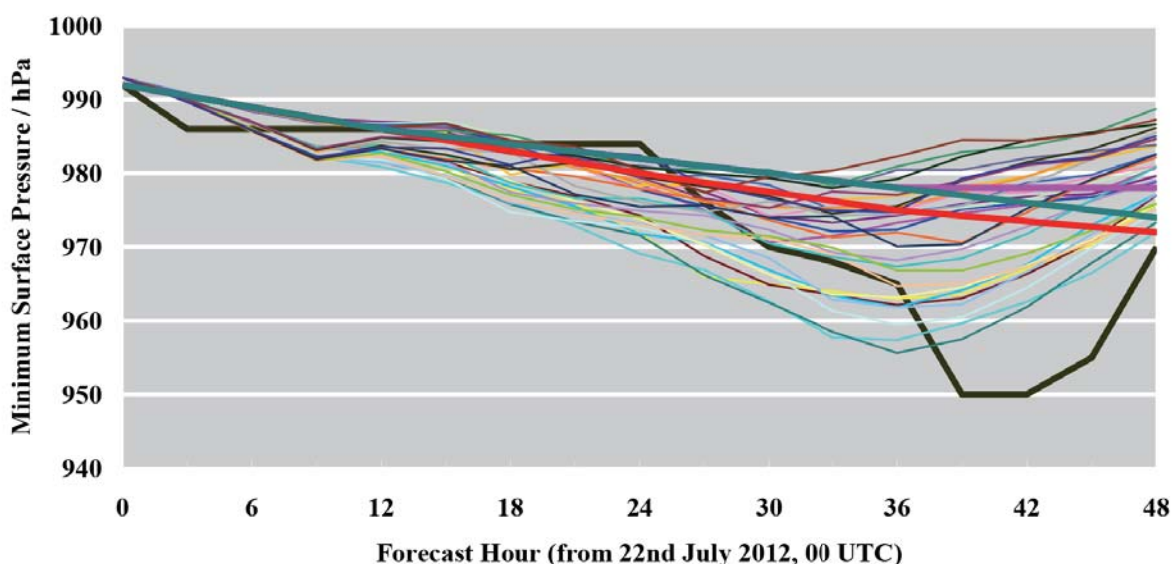


Fig. 9 Analysis (black) and NHM forecast (thin, various colours) minimum sea level pressure of Vicente, both 3-hourly, between 22nd and 24th July 2012. Thick coloured lines represent 22nd July 00 UTC runs of ECMWF (magenta), JMA (red), and NCEP (turquoise) at 12-hour intervals.

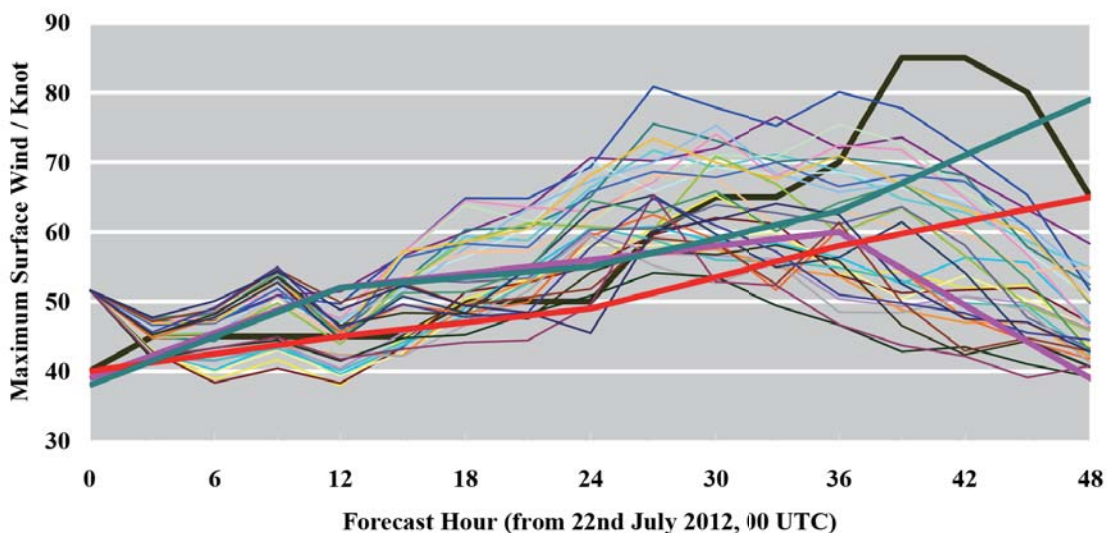


Fig. 10 Same as Fig. 8 except for maximum sustained surface wind.

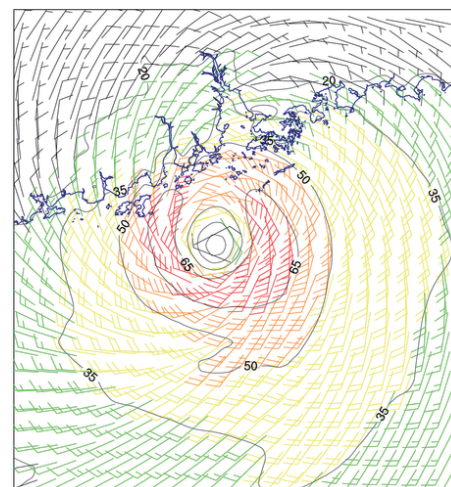
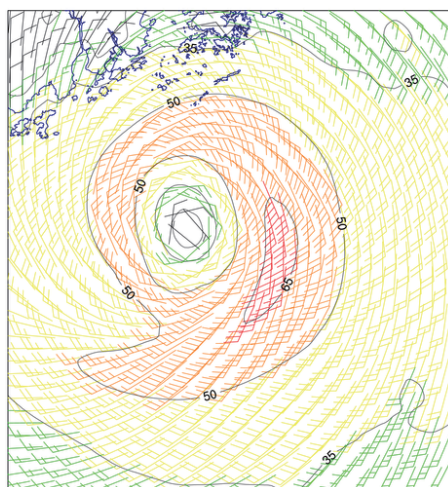
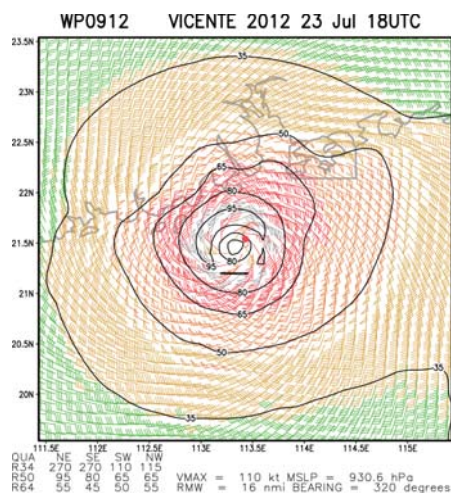
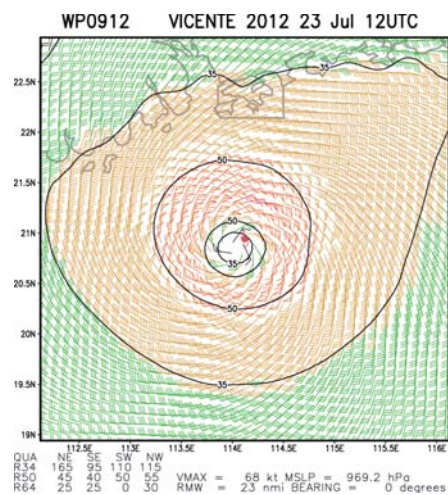


Fig. 11 Distribution of surface winds in the vicinity of Vicente before (left) and during (right) its closest approach to Hong Kong as estimated by the Multi-platform Satellite Surface Wind Analysis of NOAA (top) and as forecast by selected runs of NHM (bottom). Gales coloured in orange.

c. Impact on winds in Hong Kong

During passage of Vicente, surface winds of up to hurricane force were recorded over the southwestern waters of Hong Kong during the wee hours of the 24th (Fig. 12). In particular, a maximum 10-minute wind speed of 39.1 m/s was recorded at Cheung Chau² (see Fig. 12) at 23/1725UTC (24/0125H), 40 minutes after issuance of the Hurricane Signal No. 10 by the Observatory at 23/1645UTC (24/0045H). High-resolution forecasts of surface winds by global models and NHM are shown in Fig. 13. Given the large differences in forecast movement and hence effect on winds in Hong Kong, snapshots during the closest approach to Hong Kong by each individual model are chosen for comparison: 23/12UTC for ECMWF, 24/00UTC for JMA, and 23/14UTC for NHM. Both ECMWF and JMA are found to underestimate wind speeds in the Pearl River Estuary, with southeasterlies of only strong to gale force forecast, despite the proximity of the vortex of Vicente. On the other hand, coverage of storm-force winds by the NHM test run corresponds well to satellite products as well as to local observations (not shown).

Fig. 14 compares the forecast 10-metre wind speeds by NHM at the closest grid point (22.21N, 113.98E) to Cheung Chau, registered at the beginning of each hour, to the observed values. Model winds are shown both with and without the contribution

by forecast surface gusts, although no adjustments have been made to compensate for the 90-metre difference in altitude. The progressive strengthening of winds after 22/16UTC (23/00H) is captured by all of the test runs, although wind speeds between 22/13UTC (22/21H) and 23/07UTC (23/15H) are consistently overestimated by 5–10 m/s. This may be attributed to the model topography used in the 10-km simulations, which is unable to resolve the mountains on Hong Kong Island and hence produces a shielding effect on Cheung Chau under prevailing easterlies at the time. In terms of maximum wind speed, it is only after inclusion of surface gusts that values of around 40 m/s can be reproduced in the upper quartiles of the test runs, although the timing of occurrence is once again ahead of the actual by 4–5 hours.

Also noteworthy is the behaviour of the median and 75th percentile between 23/18H and 23/21H. A decrease in the median suggests that the simulated cyclone in certain test runs has begun to weaken when it approaches the landmass of Guangdong. At the same time, members of the top quartile continue to intensify, eventually reaching a peak at around 23/21H. This divergence in wind trends, while indicating greater forecast uncertainties, may also be interpreted as a signal for more extreme alternatives, which materialised in the current case.



Fig. 12 Distribution of surface winds in Hong Kong during passage of Vicente at 23/1720UTC. Note the occurrence of hurricane-force winds at Cheung Chau over the southwestern parts of the territory.

² The anemometer at Cheung Chau AWS stands at an elevation of 99 metres above sea level.

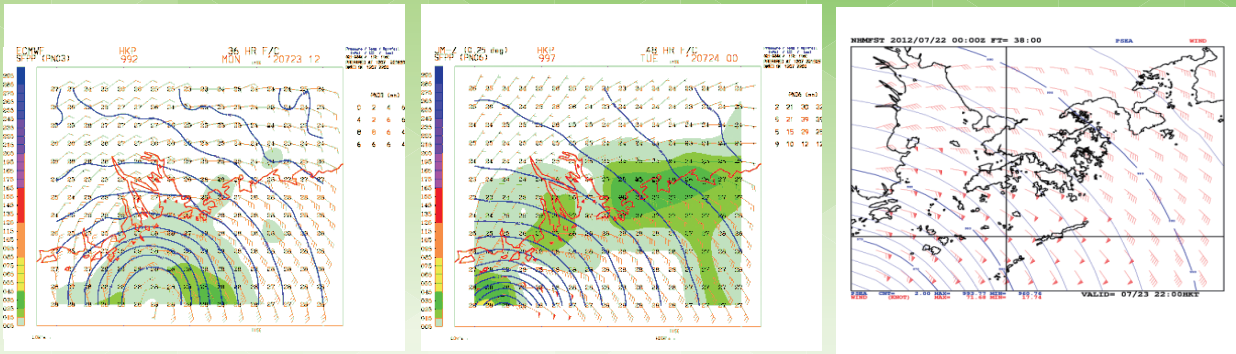


Fig. 13 Selected high-resolution surface wind forecast near the Pearl River Estuary by (left) ECMWF, (middle) JMA, and (right) selected NHM run.

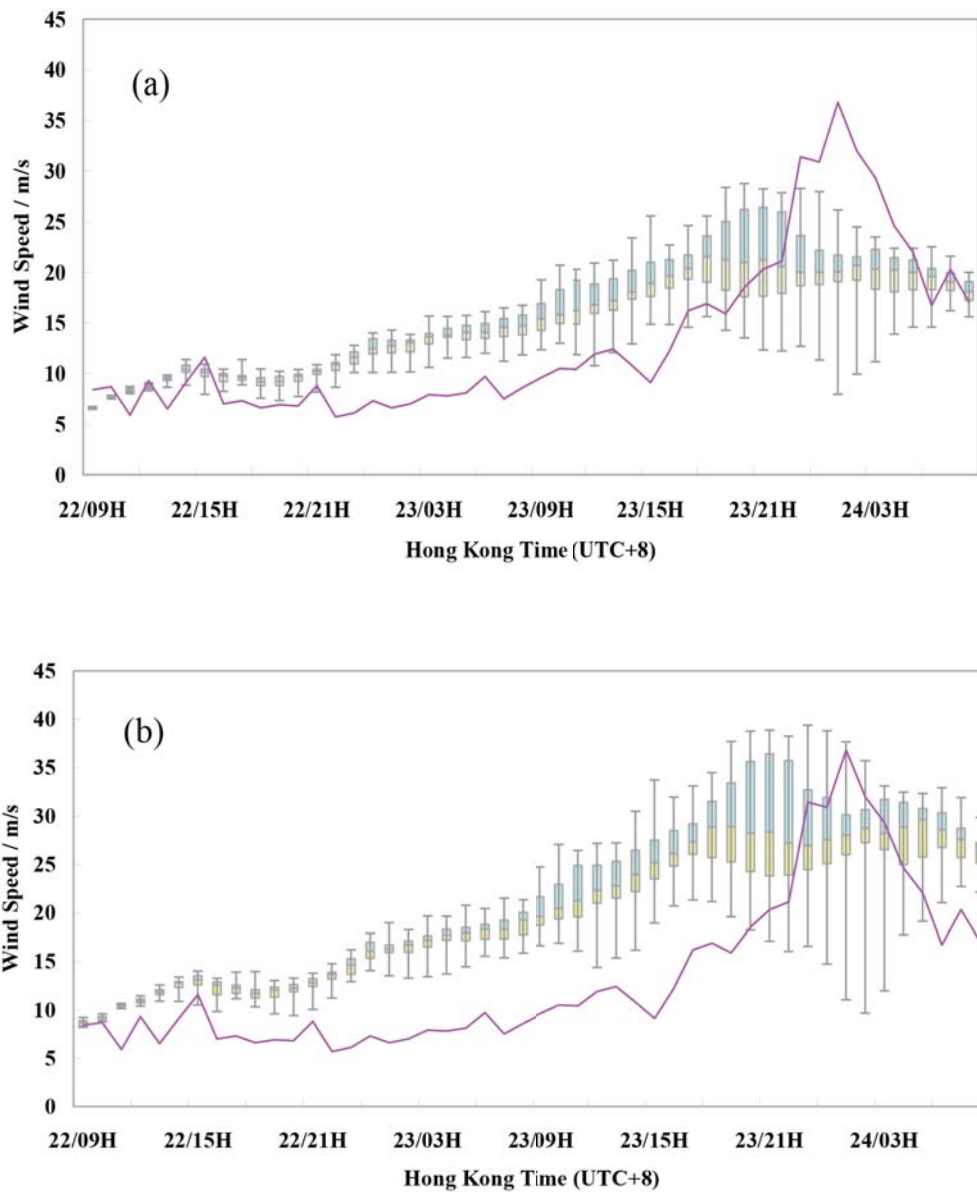


Fig. 14 Forecast time series of 10-metre wind speed by NHM (box-and-whisker), (a) without and (b) with contribution of surface gusts, at the closest grid point (22.21N, 113.98E) to Cheung Chau. Wind speed at Cheung Chau AWS Station (magenta) taken at the beginning of every hour.

d. Impact on local rainfall

Inspection of radar sequences and rainfall time series reveals that the Pearl River Estuary was mainly under the influence of propagating rainbands of Vicente on the 22nd and in the morning of the 23rd before sustained rainfall associated with convective bands closer to the TC core set in during the evening. Fig. 15 compares the evolution of the forecast and recorded average hourly rainfall³ over Hong Kong during the study period. To better account for possible regional differences, forecast values are taken as the spatial average over a rectangle of 6 x 4 grid points covering the whole territory.

Between 22/01UTC (22/09H) and 23/04UTC (23/12H), 3 distinct rainfall peaks are observed, each associated with one outer rainband of Vicente (Fig. 16). The 1st and 3rd rainbands, arriving at around 22/07UTC (22/15H) and 23/01UTC (23/09H), respectively, are well represented by most of the test runs, with onset timing accurate to about 1 hour. Median rainfall values also follow closely the observed intensity of 2–3 mm/hr. On the other hand,

forecasts of the 2nd rainband generally exhibit a time lag of 4–5 hours, which despite the larger forecast spread cannot be covered by any of the members. The larger upper-quartile rainfall as compared to the 1st rainband may perhaps be justified by noting the narrow echo band with intensity up to 30 mm/hr that occurs less than 50 km offshore.

Nearly all test runs, with the exception of the most intense, are found to underestimate the intensity of the core rainbands of Vicente, which proved capable of bringing rainfall of 5–15 mm/hr for 12 consecutive hours between 23/10UTC (23/18H) and 23/22UTC (24/06H). However, with even the least intense members suggesting non-zero rainfall throughout the period, high confidence can be inferred regarding an episode of prolonged rainfall, as can the generally increasing trend ahead of the observed peak at 23/16UTC (24/02H). In particular, the time evolution of the 75th percentile values shows remarkable similarity to the observed rainfall overnight, adding to a 24-hourly total of 142 mm between 23/00UTC and 24/00UTC, which compares favourably to the observed 196 mm.

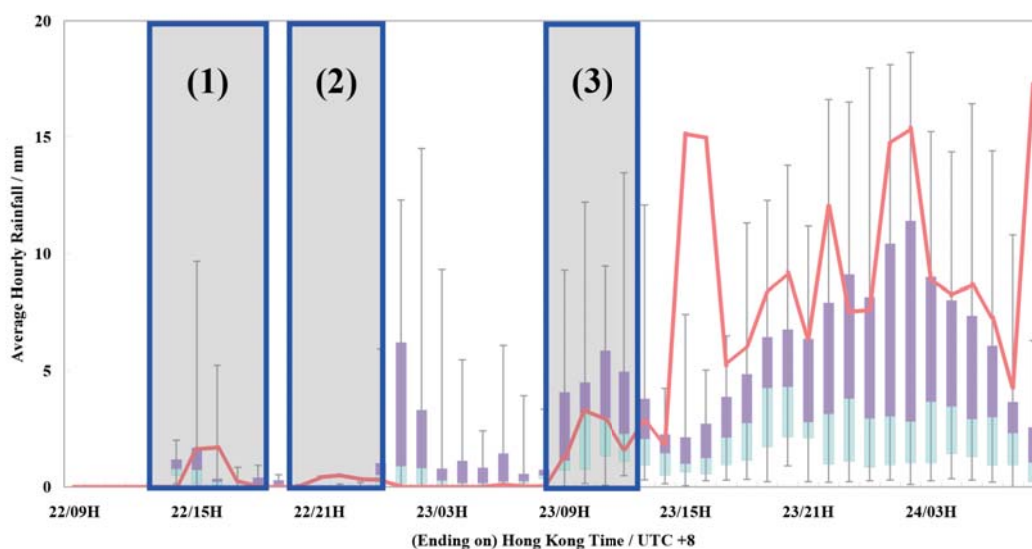


Fig. 15 Forecast time series of hourly rainfall by NHM averaged over 24 grid points covering the Hong Kong territory. Recorded values (red) based on average of 6 rain gauges used in the HKO Forecast Verification (FCV) Scheme. Rainfall peaks (1) - (3) due to propagating rainbands highlighted in blue

³ "Average recorded rainfall" follows the definition of the HKO Forecast Verification (FCV) scheme in which the mean reading from 7 rain gauges across the Hong Kong territory is normally used. During the study period, one of the gauges (Pak Tam Au, R25) was under maintenance and was therefore excluded.

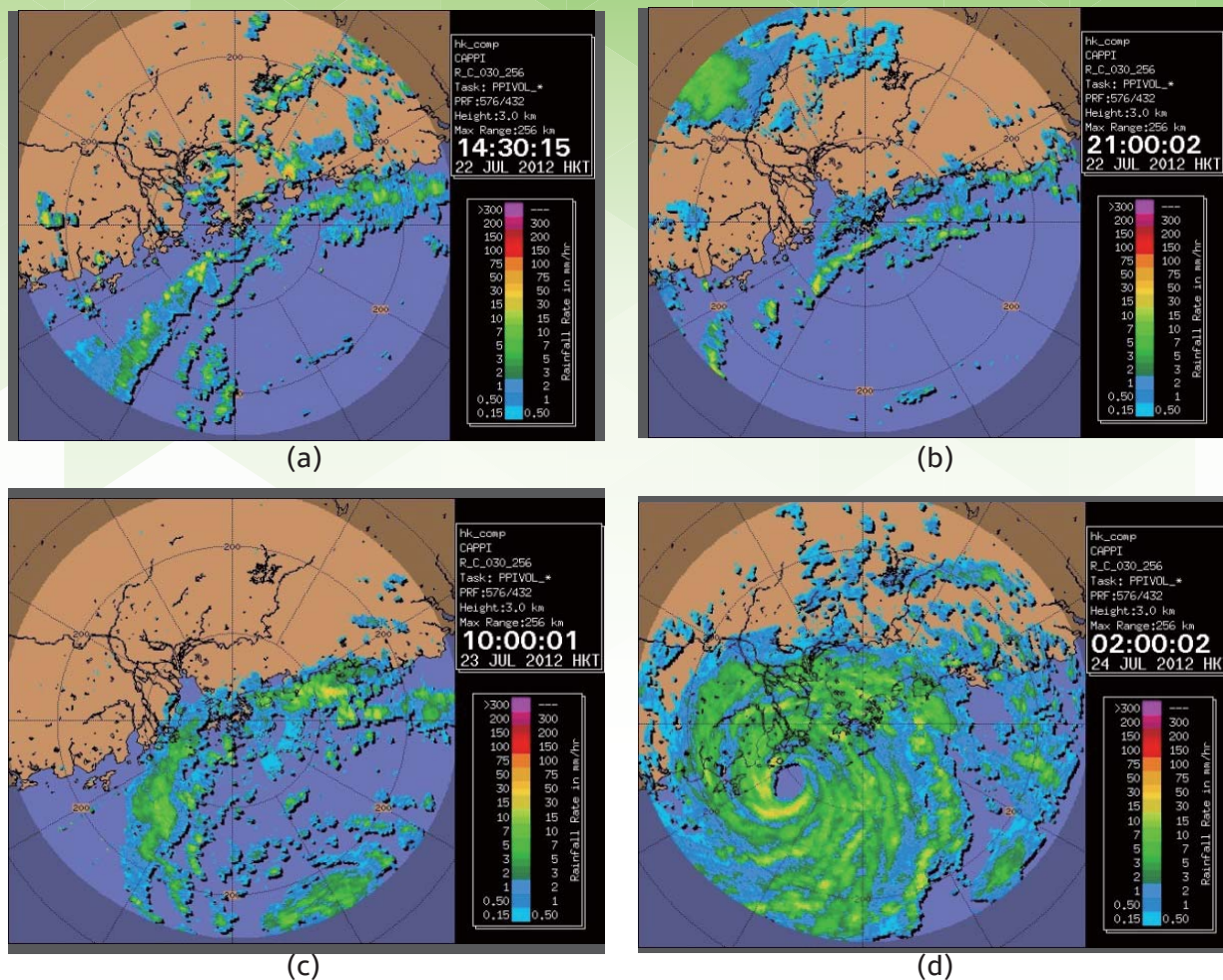


Fig. 16 256-km radar images during passage of Vicente: (a) - (c) propagating rainbands associated with observed rainfall peaks (1) - (3) in Fig. 15; (d) core rainbands bringing widespread sustained rainfall to Hong Kong.

e. Impact on spatial distribution of precipitation

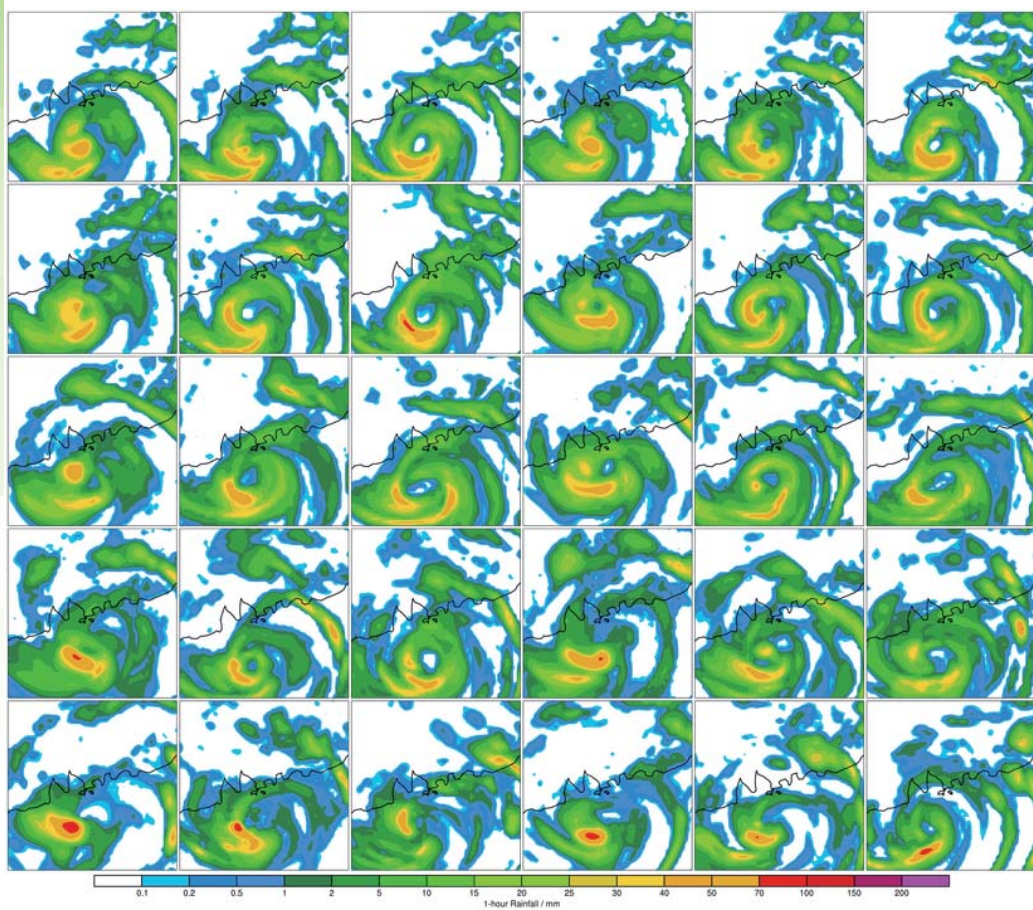
A snapshot of hourly rainfall by all 30 members is shown in Fig. 17 when the simulated cyclone is located 150 km south of Hong Kong. It can be seen that precipitation patterns show considerable variability in the shape and intensity of rain areas associated with Vicente despite the relatively limited scope of physical perturbations.

On one end of the spectrum, members exhibit tightly wrapped convective bands around a circular eye reminiscent of a full-fledged typhoon; while on the other, a more asymmetric distribution of precipitation can be observed that is usually concentrated toward the southwestern quadrant—in a few runs hourly rates exceeding 70 mm are produced. Most, however, lie in the middle,

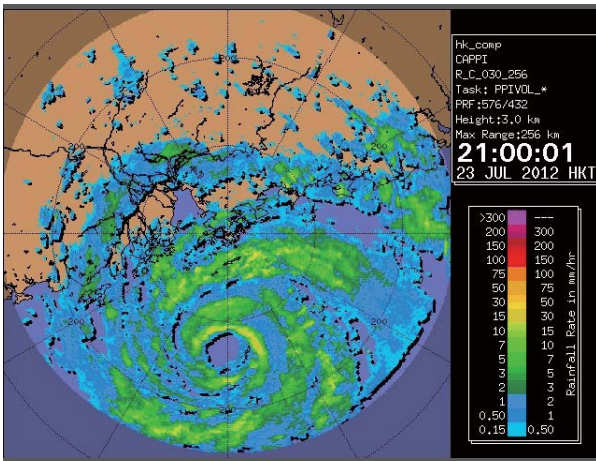
with a roughly circular distribution of rainfall albeit with varying degrees of elongation in the eyes, which is sometimes altogether absent. Also noteworthy is the representation of the outer rainband about 150 km northeast of Hong Kong, which ranges from nonexistent to perfectly arc-shaped. Even in runs where the rainband is forecast, the orientation can vary between east-west and northwest-southeast.

The distribution of forecast rainfall by NHM is then compared quantitatively with radar hourly estimates⁴ based on 3-km CAPPI scans through a spatial verification parameter, the fractional rainfall coverage, which is here defined as the fraction of an area of interest that receives rainfall exceeding a prescribed threshold. To facilitate comparison with radar data, the area within 250 km of Tai Mo Shan is studied. A total of 5 thresholds, 0.5, 1, 5, 10, and 20 mm/hr, are investigated.

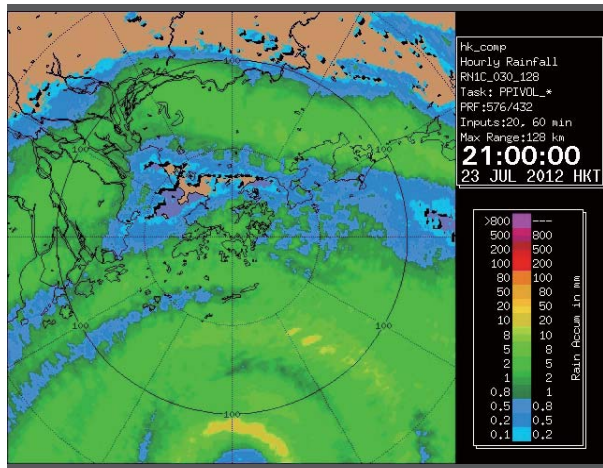
⁴ An adjusted Z-R relationship is applied after calibration of 24-hourly rainfall against average rainfall recorded in Hong Kong.



(a)



(b)



(c)

Fig. 17 Observed and forecast images of Vicente at a distance of about 150 km south of Hong Kong: (a) mosaic of hourly rainfall forecasts by all 30 test runs of NHM, (b) 256-km radar reflectivity and (c) 128-km radar estimation of hourly rainfall.

Fig. 18 shows the evolution of forecast and analysed fractional rainfall coverage between 22/00UTC and 24/00UTC. Three phases can be identified from the observed trend: (i) two sets of peaks between 22/01 UTC (22/09H) and 22/16UTC (23/00H) displaying relatively low intensities of up to 0.2, (ii) a lull period from 22/16UTC (23/00H) to 22/22UTC (23/06H) with values below 0.1, and (iii) a stepwise increase starting at 22/01UTC (23/09H), which reaches an absolute maximum at around 23/19UTC (24/03H). Phases (i) and (iii) correspond respectively to the passage of outer rainbands over the coast of Guangdong and to the sustained rainfall due to the core rainbands of Vicente, the effects of which on Hong Kong have been described in Section 2(d). Both phases are well simulated by NHM runs, which, despite a timing error of 4–5 hours in Phase (i), show good correspondence with observations in terms of peak coverage at all rainfall thresholds. In particular, during

peak intensity at 23/19UTC (24/03H), despite a slight underestimation of light rainfall (0.5, 1, and 5 mm/hr), the coverage of 10 mm/hr around 0.17 and 20 mm/hr around 0.06 can be accurately reproduced.

The overestimation of fractional coverage by NHM during Phase (ii) can be attributed to the large errors in forecast positions of Vicente after its initial looping motion. Inspection of radar images shows that, following departure of rainbands associated with Phase (i), convective activities generally subside between 22/16UTC (23/00H) and 22/22UTC (23/06H), while the bulk of Vicente has only just regained poleward movement and therefore has yet to enter within 256 km of the radar. On the other hand, given the lack of looping motion in NHM runs, the simulated TC has already tracked northwestward into the area under study and thus contributes large areas of convective rainfall.

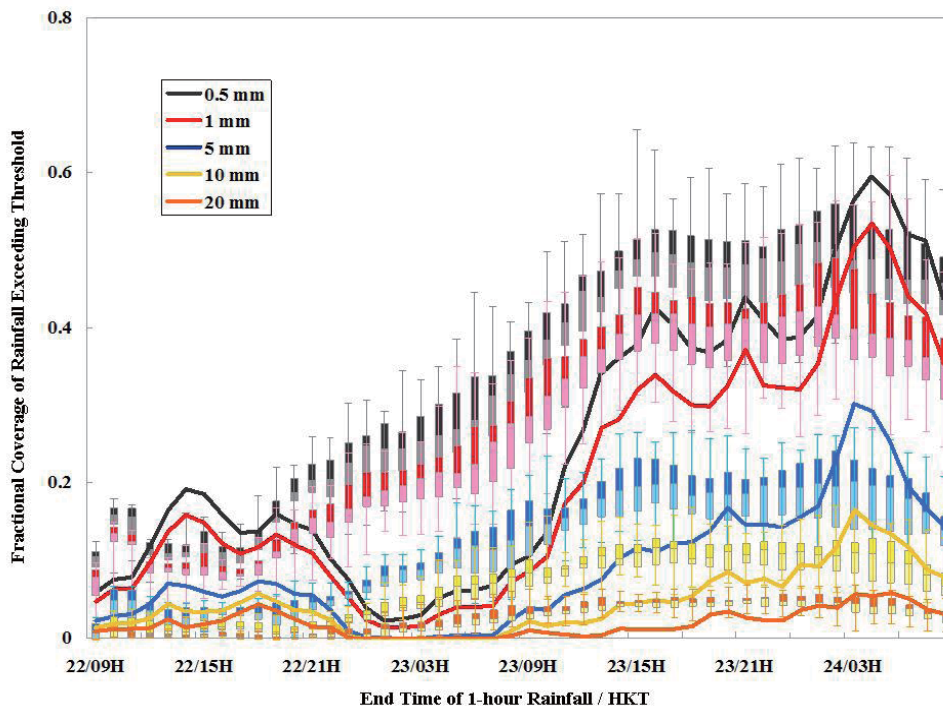


Fig. 18 Comparison of forecast (NHM, box-and-whisker) and analysed (radar estimate, solid lines) fractional rainfall coverage within 250 km of Hong Kong at rainfall thresholds of 0.5, 1, 5, 10, and 20 mm/hr.

f. Impact on distribution of convection

Intensification of Vicente during the study period has been attributed to the occurrence of “convective hot towers” [20], which are intense, localised bursts of convection linked to the genesis or deepening of TCs [21]. Despite the variety of KF parameters, and hence characteristics of convection, allowed in the test runs, certain features in agreement with literature descriptions can nonetheless be observed in selected runs.

Fig. 19 shows a composite of graupel mixing ratios at the 40th model level (about 14 km above sea level), plotted every hour, during the period 22/17UTC and 22/23UTC, together with surface wind and pressure distributions. During the 6-hour period, a region of high graupel concentration (“graupel patch”) can be observed within 150 km of Vicente, moving cyclonically around the TC centre. The occurrence of hydrometeors in the upper troposphere would require strong, penetrating updrafts and therefore suggests active convection. Indeed, a cross-section

reveals a column of coherent updrafts and high equivalent potential temperature along the eastern side of Vicente reaching 14–15 km (Fig. 20). The graupel patch first develops in the southeast quadrant, gaining intensity as it moves downwind toward the north. After reaching peak concentration between 22/19UTC and 22/20UTC, the graupel patch begins to decay on entering the northeast quadrant, implying a model life cycle of 5–6 hours. The behaviour of such a “tower” is in line with recent observational studies [22], which also report the growth and decay of “hot towers” with cyclonic rotation around the circulation centre.

In fact, several instances of “hot towers” have been observed during the life cycle of Vicente, to which a recent paper is devoted [23]. In the next section, the relation between simulated “hot tower” activities and changes in the intensity of Vicente will be further discussed using fine-tuned model runs.

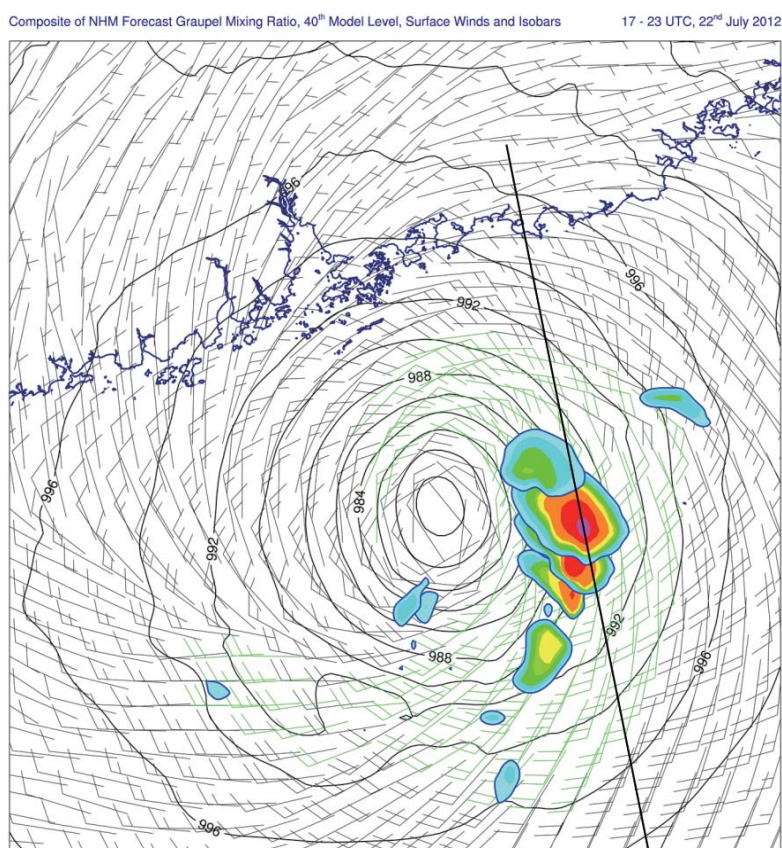


Fig. 19 Composite of forecast graupel mixing ratio (coloured) at the 40th model level (approximately 14 km above sea level), plotted hourly from 17 to 23 UTC, 22nd July 2012, on top of forecast surface winds and isobars at 23 UTC, from selected NHM run.

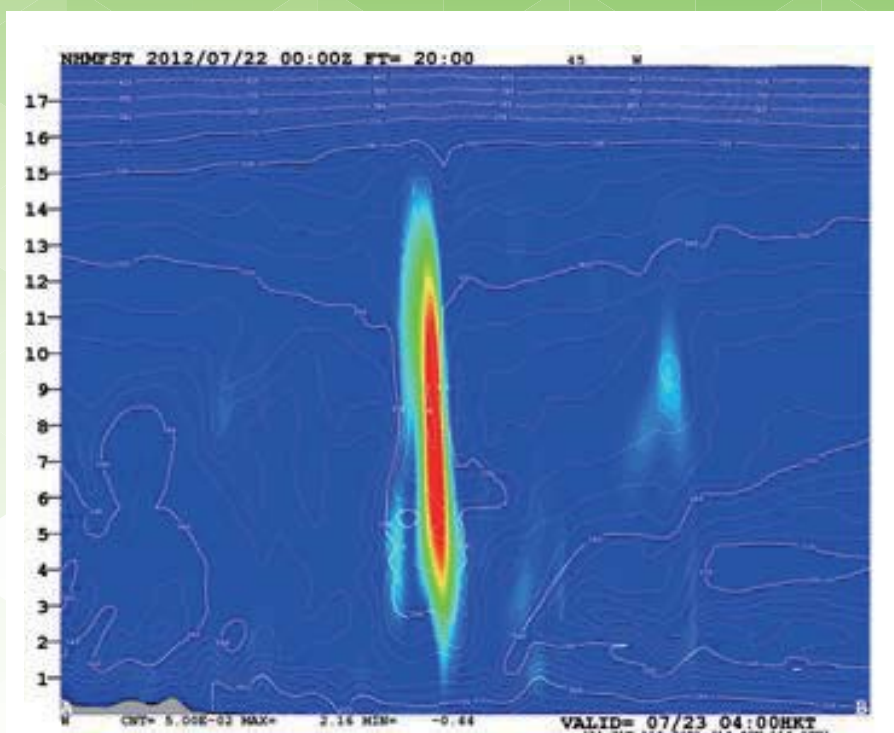


Fig. 20 Cross section, at 20 UTC, 22nd July 2012, of vertical velocity (coloured) and equivalent potential temperature (white contour) along the red line in Fig. 19.

4. Effects of Model Processes

Forecast tracks from several selected experimental configurations are shown in Fig. 21. The settings of these experiments are summarised in Table 2. The spatial spread formed by these selected forecasts generally encompasses all the forecast tracks of the 15 experiments performed. Similar to the results in Section 3 above, the centroid of these forecast locations at T+24 hours was located about 100 km northwest of the actual position at 23/00UTC. The along-track error maintained at about 60 km in the 36th hour of the forecast (23/12UTC). The forecast locations at T+48 hours were spread over the two lateral sides of the HKO warning track as well as the operational forecast. These confirm that the model spread generated in Section 3 can be reproduced in the operational configuration of NHM.

Forecast movements from the operational configuration and EXPT-KF1 (see Table 2) were in good agreement with the actual locations near the landfalling regions and inland. For EXPT-KF2, the development of convection clusters in Vicente was generally suppressed due to a weaker effect of cumulus

parameterisation. This also resulted in weaker storm intensity over the whole time integration period, though it showed a deepening during 27 to 33 hours of forecast (23/03UTC to 23/09UTC). As in Section 3, early weakening of the TC before landfall is also observed.

Several aspects of the model numerical formulation and physical processes can contribute to the development of storm intensity. Results of the track and intensity forecasts are shown in Figs. 22–23 (denoted by EXPT-RSK and EXPT-CSK). In all these experiments, alternative formulations of the bulk coefficients of surface momentum flux, sensible heat flux, and moisture flux were applied. The scheme takes into account the saturation effect of bulk coefficients under high wind conditions and was implemented in JMA-NHM after Wong *et al.* [12]. The scheme was applied to simulate the intensification of Typhoon Hagupit over the South China Sea in September 2008, showing that the revised formulation of bulk coefficients contributed positively to the intensification by the model (NHM) through a realistic representation and enhanced transfer of surface fluxes to support the storm intensification.

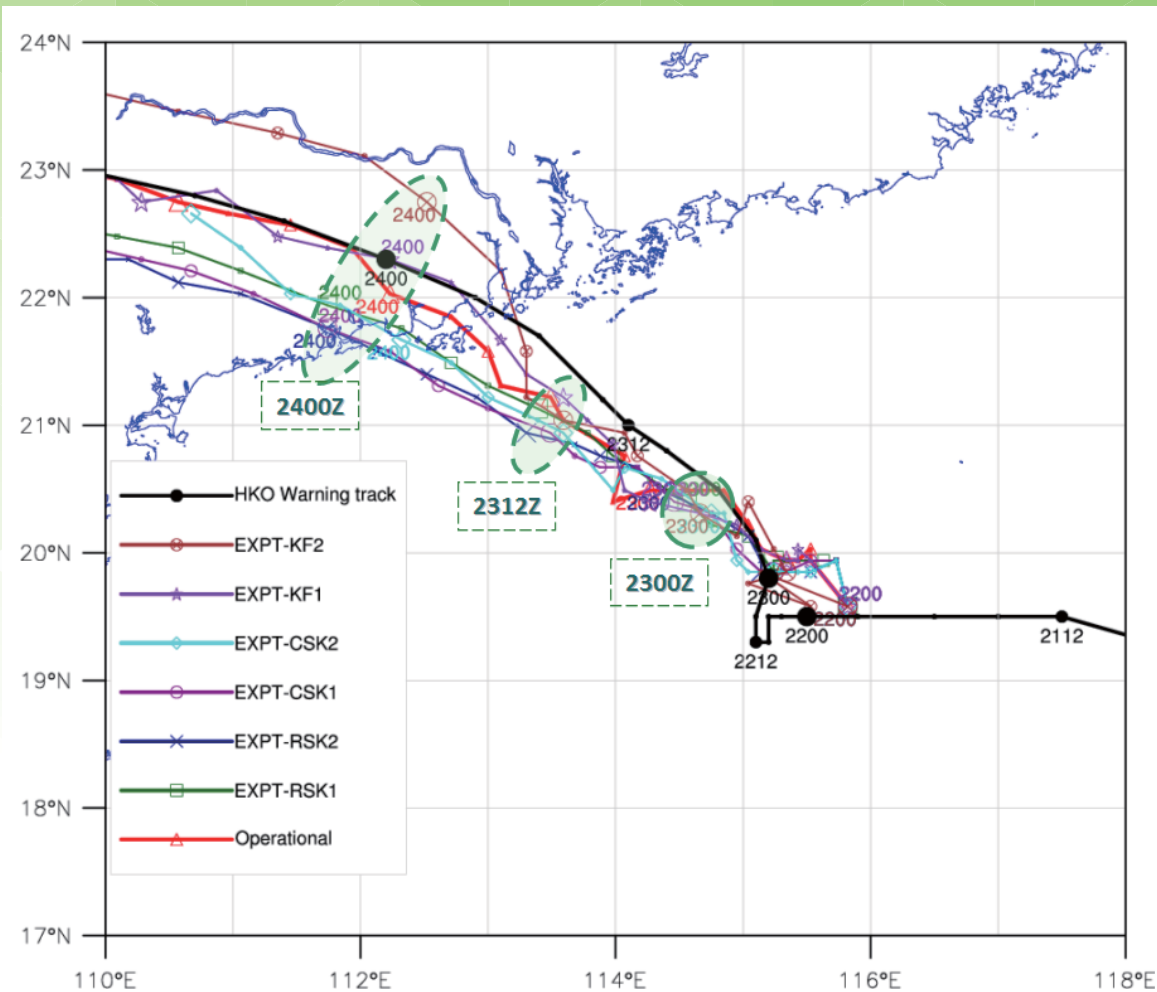


Fig. 21 Forecast tracks (coloured) from selected sensitivity experiments using the operational Meso-NHM. HKO 3-hourly analysis in black

Label of experiments	Brief descriptions
EXPT-KF[1,2]	Using different thresholds of CAPE consumption rate; KF1(2) denotes a larger (smaller) value and hence stronger effects of cumulus convection development.
EXPT-RSK[1,2]	Using operational setting of CAPE consumption rate with revised surface bulk transfer coefficients; nonlinear diffusion is relaxed in both experiments with RSK2 at a larger amount.
EXPT-CSK[1,2]	Using cloud microphysics with prognostic number concentration of cloud ice and revised surface bulk transfer coefficients; CSK1 has a stronger cumulus parameterization.

Table 2 Summary of experiments to study the effect of model processes (see Section 4)

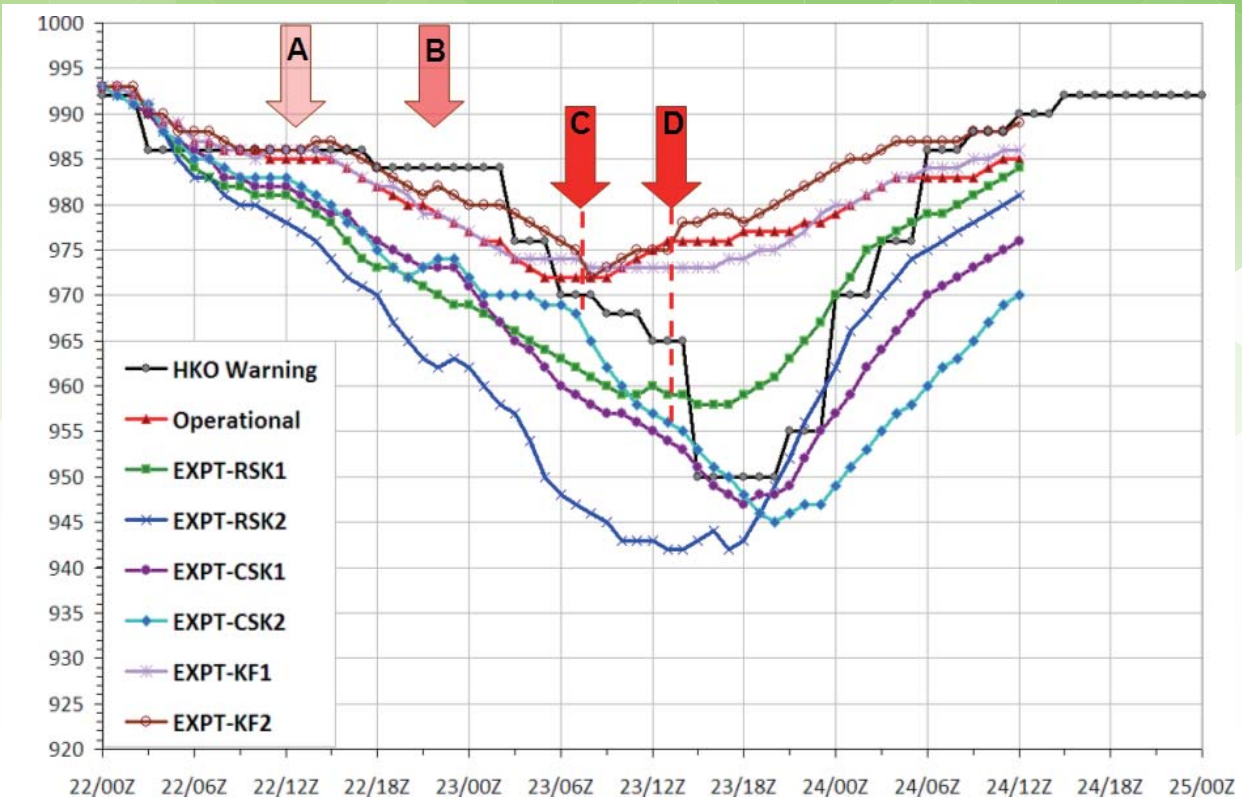


Fig. 22 Time series (coloured) of the central pressure of Vicente forecast by Meso-NHM in different experiments. HKO 3-hourly analysis in black.

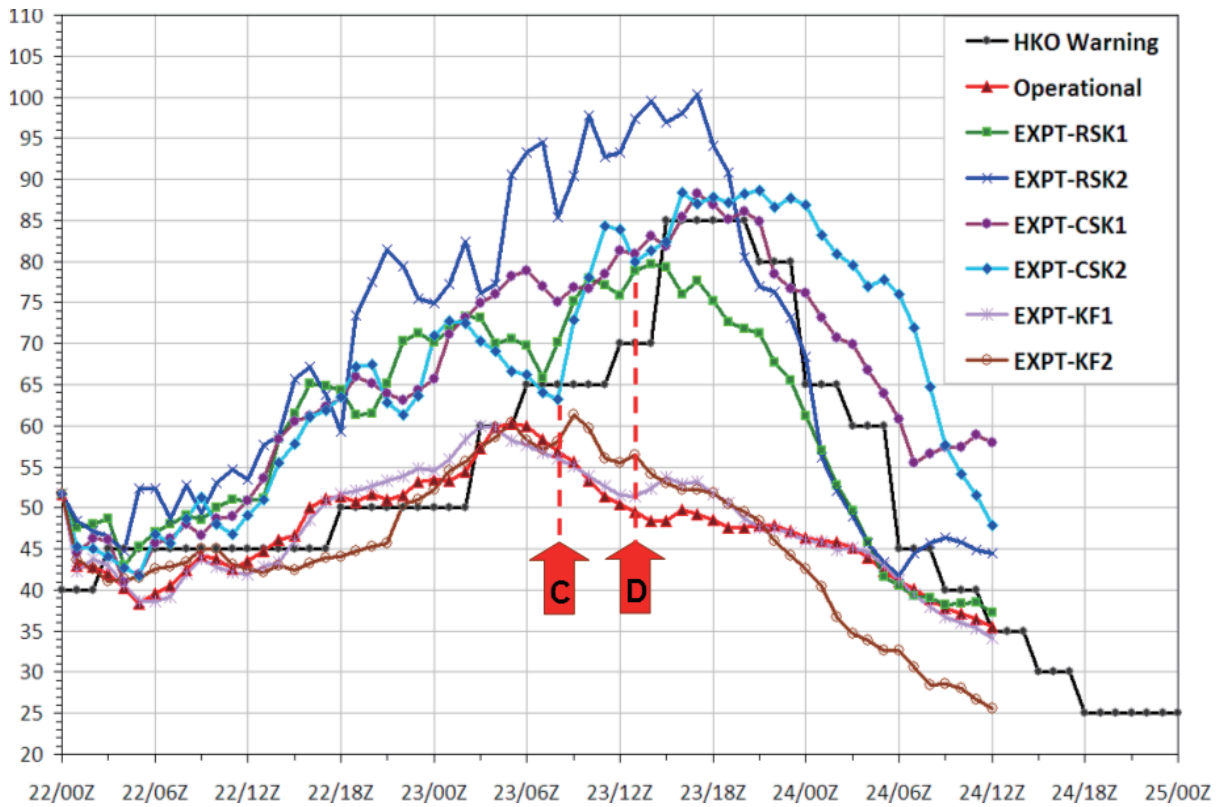


Fig. 23 Similar to Fig. 22 but for maximum wind.

Another factor in the model numerical formulation, such as specification of nonlinear diffusion timescales, can have an impact on the development of high wind areas and moisture processes in NHM. It was reported in [24] that the over-forecast of high-level cloudiness in NHM in a tropical-area simulation was due to over-diffusion of cloud water in the upper portion of the model atmosphere. To preserve numerical stability, it would be useful to see how these parameters in the numerical process affect storm intensification. Two experiments were designed, namely EXPT-RSK1 and EXPT-RSK2, to change the default nonlinear diffusion parameters according to the order of magnitude of the model prognostic variables. On top of the modified nondiffusion coefficients, revised bulk transfer coefficients were used. Both showed enhanced deepening in the first few forecast hours, and the intensification became more pronounced after T+12 hours of forecasts. They successfully captured the lowest pressure from 23/12UTC to 23/18UTC and agreed favorably with the actual peak intensity of Vicente (~ 950 hPa). The maximum winds predicted by EXPT-RSK1 and EXPT-RSK2 were 80 knots and 100 knots during the time period when the estimated maximum intensity of Vicente was 85 knots.

Another way to investigate the impact of storm intensification on the model simulation was attempted by considering different cloud microphysical processes. This formulation, using a prognostic number concentration of cloud ice, was currently applied in the inner model of AIR/NHM (RAPIDS-NHM with a horizontal resolution of 2 km). Two experiments, EXPT-CSK1 and EXPT-CSK2, were conducted with the default settings of nonlinear diffusion parameters. The only difference was that a more "active" cumulus parameterisation was applied in EXPT-CSK1 (similar to EXPT-KF1). The results indicate that both configurations produced intensification trends similar to those in EXPT-RSKs. Moreover, improvements were also seen in the simulation of storm intensity in that the lowest central pressures (and the highest maximum winds) during 23/15UTC to 24/00UTC came closer to the actual.

There were close connections between the numerical simulation of the deepening trend and the development of intense convection near the inner core of Vicente. For instance, in the 12-hour forecast and beyond, the development of the convective cluster that

formed into a towering convection that reached more than 15 km over the southern flank of Vicente was simulated by Meso-NHM. Fig. 24 shows the simulated radar reflectivity and the echo top of the 33 dBZ reflectivity isosurface. The echo top of the forecast convection cluster increased from around 10 km in the preceding hours (not shown) to more than 15 km and remained over the southern flank of Vicente in the following 6–12 hours. The development of this intense convection tower to the south of the storm centre in the NHM forecast also coincided with the TRMM microwave imager / precipitation radar (a.k.a. TMI/PR) observations at an earlier time (22/0947UTC).

A second stage of development of these intense convection towers occurred near T+30 (23/06UTC), while the storm started to strengthen further 1–2 hours afterward (arrows C in Figs. 22 and 23). Several convection towers developed successively over the inner core and rotated around the centre of Vicente. Fig. 25 shows the echo top of 33dBZ at 23/12UTC (23/20H) together with the regions enclosing the echo top higher than 14 km during the preceding 6 hours (up to 23/06UTC (23/14H)). For instance, the convection tower (A) first formed over the southern semicircle of Vicente and moved cyclonically to about 200 km south of HK at 23/12UTC (23/20H). Two other towering convection clusters, B and C, developed (around 23/09UTC (23/17H)) over the inner-core region of Vicente. They also moved cyclonically, such that the echo top of B lowered toward 23/12UTC (23/20H) while convection tower C moved south of the storm. The maximum wind reached 85 knots at T+35 and T+36 and then dropped slightly in the following hour. It was interesting to note that the convection tower reintensified explosively in the following hour (location D at T+37, Fig. 26) to produce a larger area of echo top aloft up to 17 km. To depict the structure of this convection tower, a vertical cross section was made along the system (line XY passing through D). This shows that the convection tower developed to the model tropopause (around 16.5 km, compared to the actual tropopause at 16.8 km according to the radiosonde data of King's Park at 23/12UTC). The model-predicted specific humidity of rain water (Q_r), snow (Q_s), and cloud ice (Q_{ci}) ascended inside the whole intense convective system (positive vertical velocity w shown in red in the bottom right-hand panel in Fig. 26). Similar towering convection can also be identified from satellite and radar observations, as reported

in [23]. This provided a source of latent heat release within the inner core of Vicente and supported the final stage of intensification until the central pressure of the simulated cyclone reached its minimum of about 945 hPa at 23/18UTC, with maximum winds of about 88 knots until landfall of Vicente toward 24/00UTC.

In addition to the central intensity and maximum winds of Vicente, the wind predictions over Hong Kong and adjacent waters were also improved. Fig. 27 shows T+39 forecasts of surface winds over the coast of Guangdong at 23/15UTC. Section 3 showed that high winds observed offshore could be reproduced only after inclusion of model surface gusts. The discrepancies were also

observed in the forecasts by an operational version of the model, as well as in EXPT-KF1, where the tuned convection physics provided only marginal improvement. Using a better combination of model options (EXPT-RSK and EXPT-CSK), the areal coverage of high winds by Meso-NHM was improved. Storm force winds of about 50 knots covered the southwestern part of the Lantau Island and adjacent waters while forecast surface gusts over these regions were up to 70 knots. Operationally, such improvements could have been useful for assessing local winds during passage of Vicente at a lead of more than one day, as well as for considering tropical cyclone warning signals and preparedness for high-impact weather.

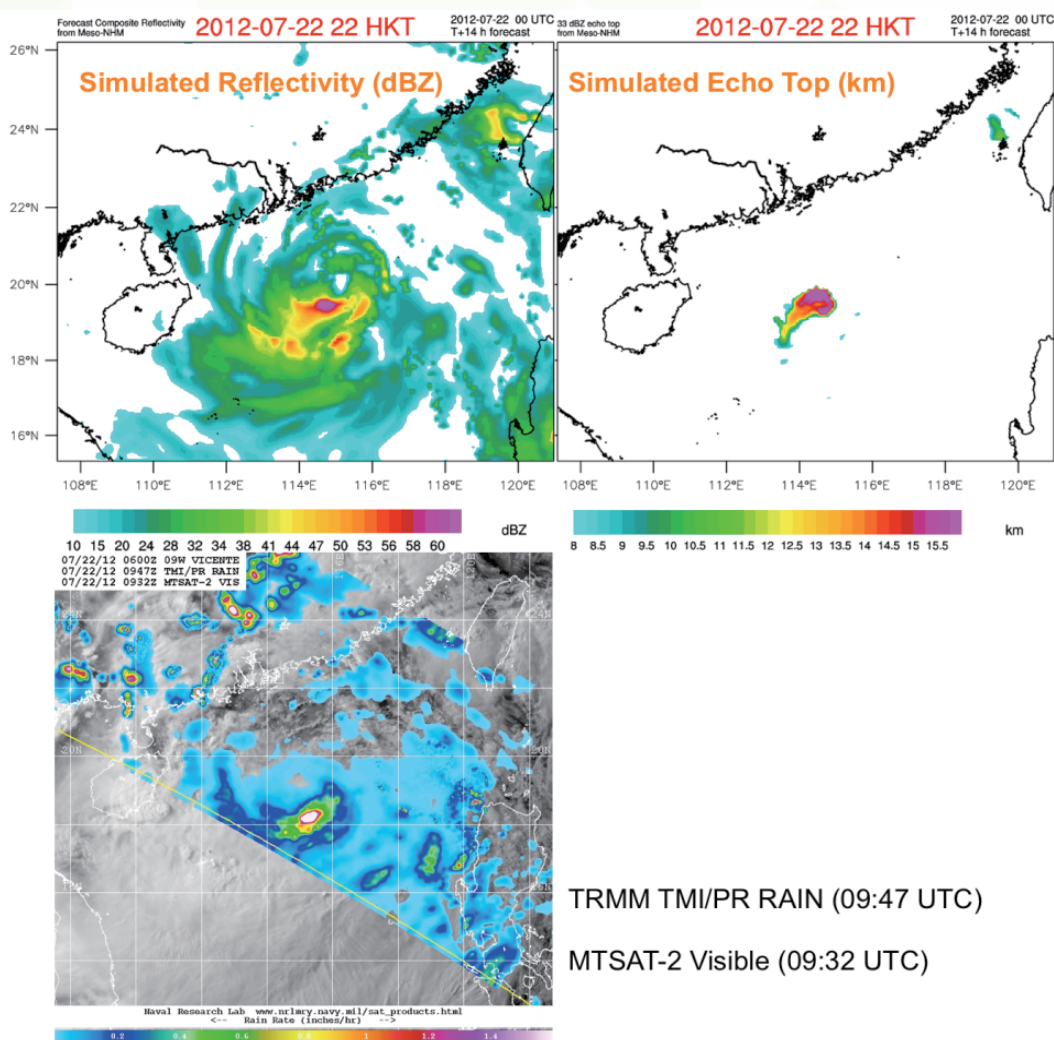


Fig. 24 Simulated radar reflectivity and echo top of 33 dBZ reflectivity isosurface in the vicinity of Vicente on 22nd July 2012. Microwave image by TRMM TMI /PR included for comparison.

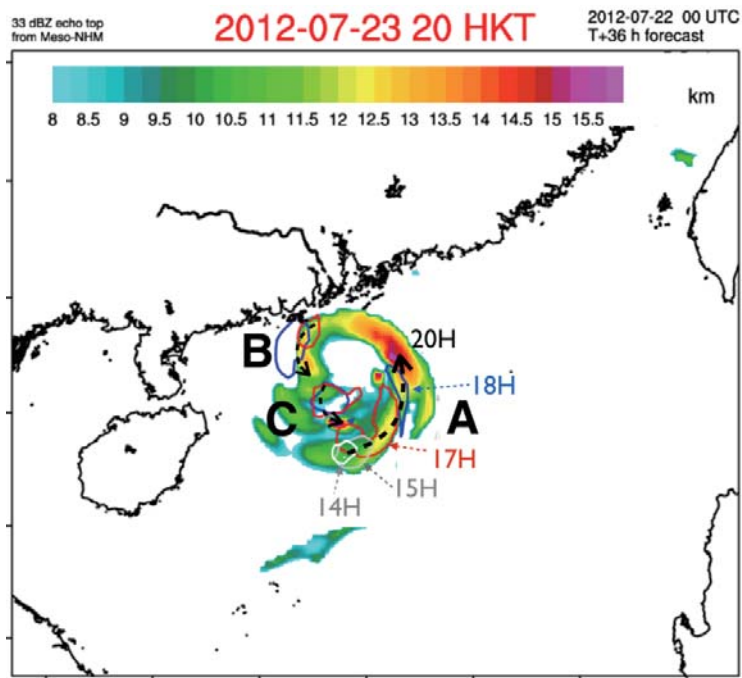


Fig. 25 Simulated echo top in the vicinity of Vicente (coloured) in experiment EXPT-CSK2. Echoes exceeding 13.5 km in height (A, B, and C) due to towering convection during the previous hours are given in coloured contours.

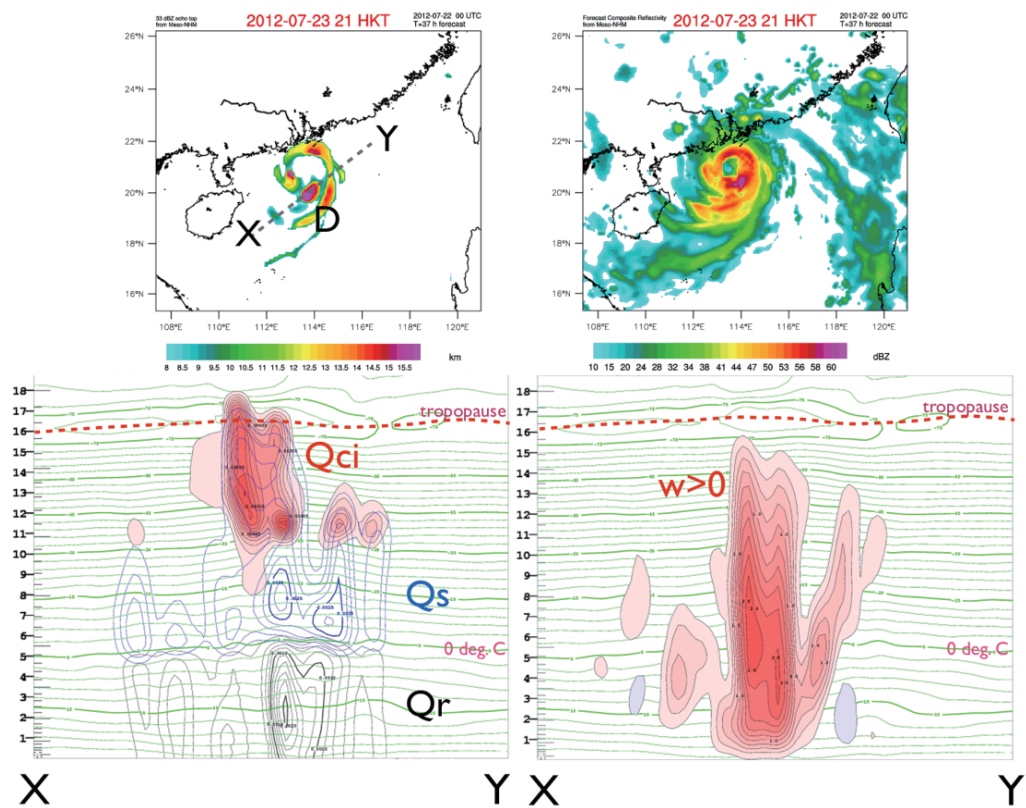


Fig. 26 Simulated radar reflectivity (right) and echo top of 33 dBZ reflectivity isosurface (left) in the vicinity of Vicente on 23rd July 2012 with cross-sections along X-Y (bottom) showing hydrometeors and vertical velocity.

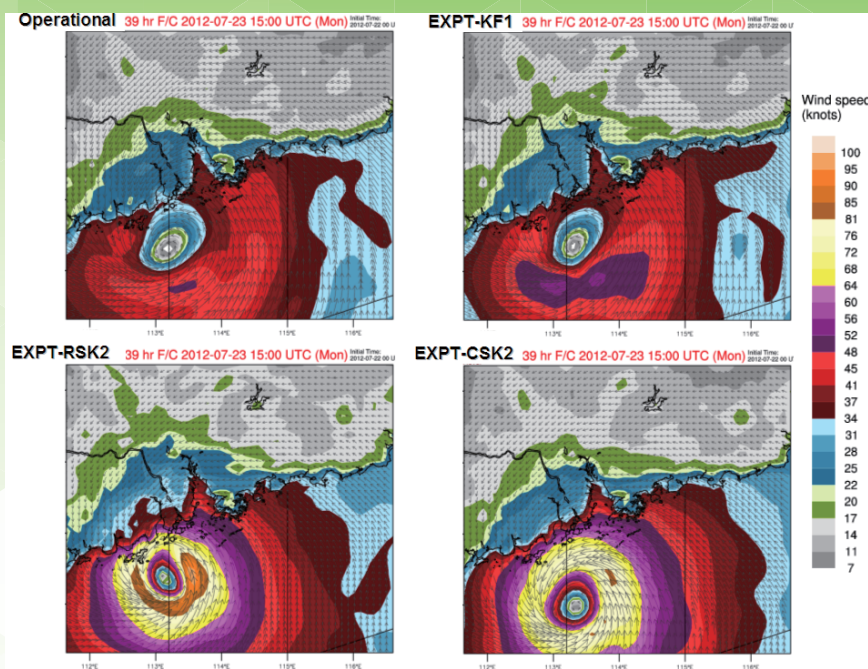


Fig. 27 Forecast of 10-m wind along the coastal areas of Guangdong from selected experiments of Meso-NHM. Hurricane-force winds associated with Vicente can be reproduced using a suitable combination of settings (bottom).

5. Impact of GFS Reconnaissance Flight Observations

Reconnaissance flights were conducted by GFS during 22/04UTC–22/06UTC over a path located in the northeastern quadrant and in the western proximity of the storm center. Flight route and data collected at the two altitudes of about 3000 m (from A to B) and 750 m (from B to A) are shown in Fig. 28. East to northerly winds of 40–50 knots were recorded at 3000 m when the aircraft approached the storm center from A, while easterly winds at 60 knots or above at the lower level were recorded about 50 km north of the centre.

Fig. 29 compares a number of model analysis fields between the control experiment (CNTL) and after assimilation of GFS flight observations (GFS). Areas of high wind were generally located over the right-hand semicircle in the CNTL analysis (top panel, Fig. 29). Wind speeds of about 20–30 knots were seen along the line AB. After inclusion of flight observations in the 3D-VAR analysis, model-analysed wind speeds north of the storm centre were increased. The observed easterly winds at 60 knots or above along AB (Fig. 28) were assimilated in the model analysis to yield a positive increment of wind speed from near the surface up to 850 hPa (middle panel, Fig. 29) and enhanced the cyclonic circulation of the storm. Assimilation of GFS flight measurements also increased the low-

level moisture content over the storm centre and to its south (bottom panel, Fig. 29), leading to greater resemblance to the satellite image (Fig. 28) regarding the presence of a deep cloud cluster covering the centre and southern semicircle of Vicente at the time.

Forecast tracks of the CNTL and GFS experiments, initialised at 22/06UTC, are shown in Fig. 30. Forecast movements in general were not far from the actual, although both model runs were not capable of fully resolving the initial slow movement in the first 12–18 hours. The use of GFS data resulted in reduction of the mean track error up to 48 hours ahead by about 10%. In terms of intensity, strengthening of the low-level cyclonic vortex provided a more favorable environment for intensification (Fig. 31). A minimum pressure of 965 hPa was forecast for the period from 23/09UTC to 23/15UTC, slightly lower than in CNTL but still weaker than the actual by 15 hPa.

Improvements made in the storm intensity forecast can be further illustrated in Fig. 32, which compares the forecast surface wind and gusts from the CNTL and GFS runs. Through the assimilation of GFS flight measurements, a broader area of storm-force winds can be forecast by Meso-NHM over the southern hemisphere of Vicente, although the area extended only to southern Hong Kong, as in the CNTL run. The areas of high surface gusts were also enlarged in the GFS experiment. While

surface gusts at hurricane force or above were already forecast in the vicinity of Hong Kong in both experiments, the GFS experiment further suggested a southerly jet exceeding 85 knots about 50 km offshore.

6. Conclusions and Further Work

Effects of various configurations of NHM including cumulus parameterisation, surface exchange, and cloud microphysics on the forecast position, intensity, and structure of TC Vicente have been studied. Key findings are as follows:

By applying a range of parameter values in the Kain-Fritsch parameterisation scheme, it is possible to generate, between 36 and 48 hours prior to landfall, a spread in forecast TC positions that encompasses the actual movement of Vicente. At T+48, the mean positional spread of about 40 km, while lower than the average model positional error of around 100 km, is comparable to literature values of contributions from perturbations of physical parameterisations in global EPS [1].

Temporal and spatial evolution of precipitation over the Hong Kong territory is well captured by the test runs, which indicate high confidence in prolonged rainfall of 10–15 hours at 5–10 mm/hr. In particular, the 75th percentile of forecast hourly rainfall shows remarkable agreement with the average values recorded locally. The forecast fractional coverage of rainfall along the coast of Guangdong by NHM also agrees with the radar estimation, suggesting model skill in reproducing the structure of both the inner and outer rainbands of Vicente.

Test runs show good agreement on the deepening trend of Vicente, with more intense members attaining minimum pressure within 10 hPa and maximum wind within 5 m/s of the analysed peak intensity. Locally, occurrence of hurricane winds over the southwestern waters of Hong Kong can be reproduced by the 75th percentile of model values after the addition of surface gusts.

To accurately forecast the intensification as well as the timing of the peak intensity of Vicente, however, a combined use of model parameters is necessary. It is shown in the experiments (EXPT-RSK and EXPT-CSK) that the selection of an optimal set of parameters—including numerical processes—can contribute to model storm development. The use of different model processes such as revised formulation of surface bulk transfer coefficients and cloud microphysics also contributes positively to some areas of intensity forecasts.

Rapid intensification of Vicente into a severe typhoon during the evening of 23rd July 2012 was closely related to the development of convective hot towers (CHT). In one of the experiments (EXPT-CSK2), several phases of intensification are simulated by Meso-NHM, which are preceded by the development of towering convections up to the model tropopause with a lead time of 1–2 hours. While a detailed model diagnosis will be reported separately in the future, experimental results show that model forecasts are in good agreement with the conceptual framework of CHT, in which the development of high-top towering convection is a precursor of and has a close connection to TC intensification through latent heat release. In that model setup, the enhancement of towering convections in Meso-NHM over the operational version can be attributed to the revised formulation of surface flux to support a stronger transfer of heat and moisture from the sea surface, as well as the use of modified cloud microphysics to include the prognostic number concentration of cloud ice to better represent cloud processes when the convection towers or the overall TC system developed to a higher altitude.

Additional observations from a GFS reconnaissance flight are found to improve the model analysis of storm structure such as the distribution of low-level winds and moisture. Low-level cyclonic vorticity is enhanced by the assimilation of flight measurements near the core of Vicente. The improved model initial conditions contribute positively to the intensification of Vicente, though the difference over the operational version gradually diminishes.

Looking ahead, while alternative settings of NHM have shown value in estimating the likelihood of extreme winds and precipitation locally as well as in improving TC intensity forecasts in the case of Vicente, the long-term effects of such “optimal settings” on the verification performance of other weather elements remain unknown and therefore require systematic study using more TC cases.

On another note, spatial verification parameters have been demonstrated to provide concise information in the evaluation of high-resolution precipitation forecasts under TC conditions. Similar verification methods can be explored for other synoptic regimes, particularly the southwest monsoon, to enhance understanding of model performance under various conditions, thus promoting a more informed interpretation of model products.

Acknowledgments

The authors would like to thank Dr. C.M. Cheng and Mr. K.C. Tsui for their insightful comments on the manuscript. Discussions with Mr. H.Y. Yeung on “hot towers” have been most illuminating. KKH is indebted to WKW for his guidance and generous sharing of expertise.

Reference

- [1] Lang, S.T.K., M. Leutbecher, and S.C. Jones, 2012: Impact of perturbation methods in the ECMWF ensemble prediction system on tropical cyclone forecasts. *Q.J.R. Meteorol. Soc.*, **138**: 2030–2046.
- [2] Molteni, F., R. Buizza, T.N. Palmer, and T. Petroliaigis, 1996: The ECMWF Ensemble Prediction System: Methodology and validation. *Q.J.R. Meteorol. Soc.*, **122**: 73–119.
- [3] Schwartz, C.S., and Coauthors, 2010: Toward improved convection-allowing ensembles: Model physics sensitivities and optimizing probabilistic guidance with small ensemble membership. *Wea. Forecasting*, **25**, 263–280.
- [4] Clark, A.J., W.A. Gallus, M. Xue, F. Kong, 2010: Growth of spread in convection-allowing and convection-parameterizing ensembles. *Wea. Forecasting*, **25**, 594–612.
- [5] Jiang, Haiyan, 2012: The relationship between tropical cyclone intensity change and the strength of inner-core convection. *Mon. Wea. Rev.*, **140**, 1164–1176.
- [6] Deshpande, M.S., S. Pattnaik, and P.S. Salvekar, 2012: Impact of cloud parameterization on the numerical simulation of a super cyclone. *Ann. Geophys.*, **30**, 775–795.
- [7] Nasrollahi, N., A.A. Kouchak, J. Li, X. Gao, K. Hsu, and S. Sorooshian, 2012: Assessing the impacts of different WRF precipitation physics in hurricane simulations. *Wea. Forecasting*, **27**, 1003–1016.
- [8] Holloway, C.E., S.J. Woolnough, and G.M.S. Lister, 2012: Precipitation distributions for explicit versus parameterised convection in a large-domain high-resolution tropical case study. *Q.J.R. Meteorol. Soc.* **138**, 1692–1708.
- [9] Yang, B., Y. Qian, G. Lin, R. Leung, and Y. Zhang, 2012: Some issues in uncertainty quantification and parameter tuning: A case study of convective parameterization scheme in the WRF regional climate model. *Atmos. Chem. Phys.*, **12**, 2409–2427.
- [10] Craig, George C., and Suzanne L. Gray, 1996: CISK or WISHE as the mechanism for tropical cyclone intensification. *J. Atmos. Sci.*, **53**, 3528–3540.
- [11] Montgomery, M.T., R.K. Smith, and S.V. Nguyen, 2010: Sensitivity of tropical-cyclone models to the surface drag coefficient. *Q.J.R. Meteorol. Soc.*, **136**: 1945–1953.
- [12] Wong, W.K., S. Sumdin, and E.S.T. Lai, 2010: Development of air-sea bulk transfer coefficients and roughness lengths in JMA non-hydrostatic model and application in prediction of an intense tropical cyclone. *Scientific Online Letters on the Atmosphere (SOLA)*, **6**, 65–68.
- [13] Wong, W.K., 2011: Development of operational rapid update non-hydrostatic NWP and data assimilation systems in the Hong Kong Observatory. *Technical Reports of the Meteorological Research Institute* No. 65, December 2011, 87–100.
- [14] Saito, K., and Coauthors, 2006: The operational JMA non-hydrostatic mesoscale model. *Mon. Wea. Rev.*, **134**, 1266–1298.
- [15] Lee, J.C.W., and S.T. Cha, 2012: Application of an improved vortex tracking algorithm in operational NWP systems. The 26th Guangdong-Hong Kong-Macau Seminar on Meteorological Science and Technology, Macau, 17th - 19th January, 2012.
- [16] Kain, J.S., 2004: The Kain-Fritsch convective parameterization: An update. *J. Appl. Meteor.*, **43**, 170–181.
- [17] Ohmori, S., and Y. Yamada, 2006: Development of cumulus parameterization scheme in the nonhydrostatic mesoscale model at the Japan Meteorological Agency. WGNE Research Activities in Atmospheric and Oceanic Modelling, Section 4, 21–22.
- [18] Kondo, J., 1975: Air-sea bulk transfer coefficients in diabatic conditions. *Bound.-Layer Meteor.*, **9**, 91–112.
- [19] Beljaars, A., 1995: The parameterization of surface fluxes in large-scale models under free convection. *Quart. J. Roy. Meteor. Soc.*, **121**, 255–270.
- [20] Gutro, R., 2012: NASA’s sighting of hot towers indicated Typhoon Vicente’s rapid intensification. (http://www.nasa.gov/mission_pages/hurricanes/archives/2012/h2012_Vicente.html)
- [21] Montgomery, M.T., M.E. Nicholls, T.A. Cram, and A.B. Saunders, 2006: A vortical hot tower route to tropical cyclogenesis. *J. Atmos. Sci.*, **63**, 355–386.
- [22] Guimond, S.R., G.M. Heymsfield, and F.J. Turk, 2010: Multi-scale observations of Hurricane Dennis (2005): The effects of hot towers on rapid intensification. *J. Atmos. Sci.*, **67**, 633–654.
- [23] Yeung, H.Y., 2013: (to be published)
- [24] Hayashi, S., 2011: Statistical verification of short-range forecasts by the NHM and WRF-ARW models with fine resolution. Technical Reports of the Meteorological Research Institute No. 65, December 2011, 10–13.

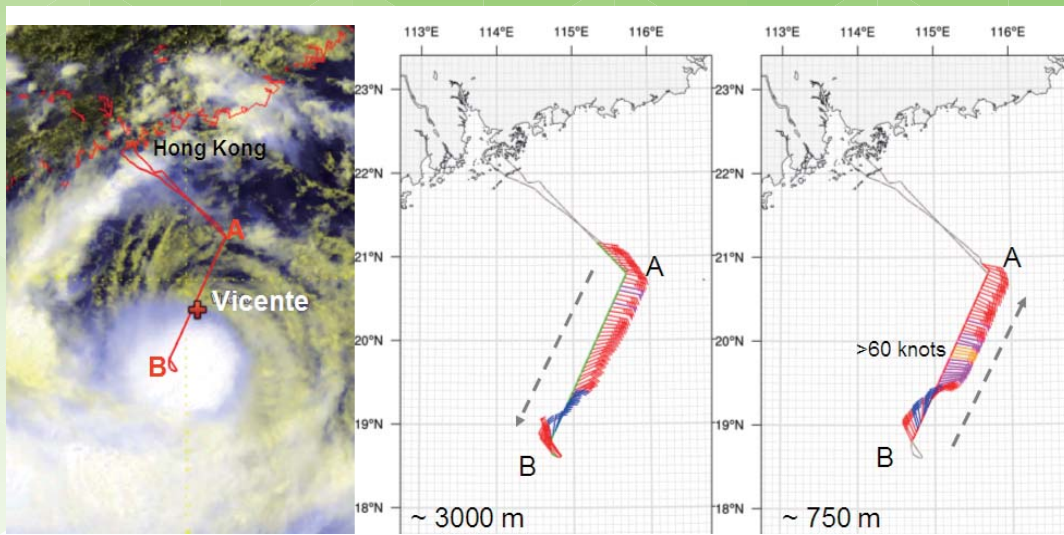


Fig. 28 GFS flight path and wind measurements at the 3000 m and 750 m levels. Orange wind barbs on the right panel represent wind speeds of 60 knots or above.

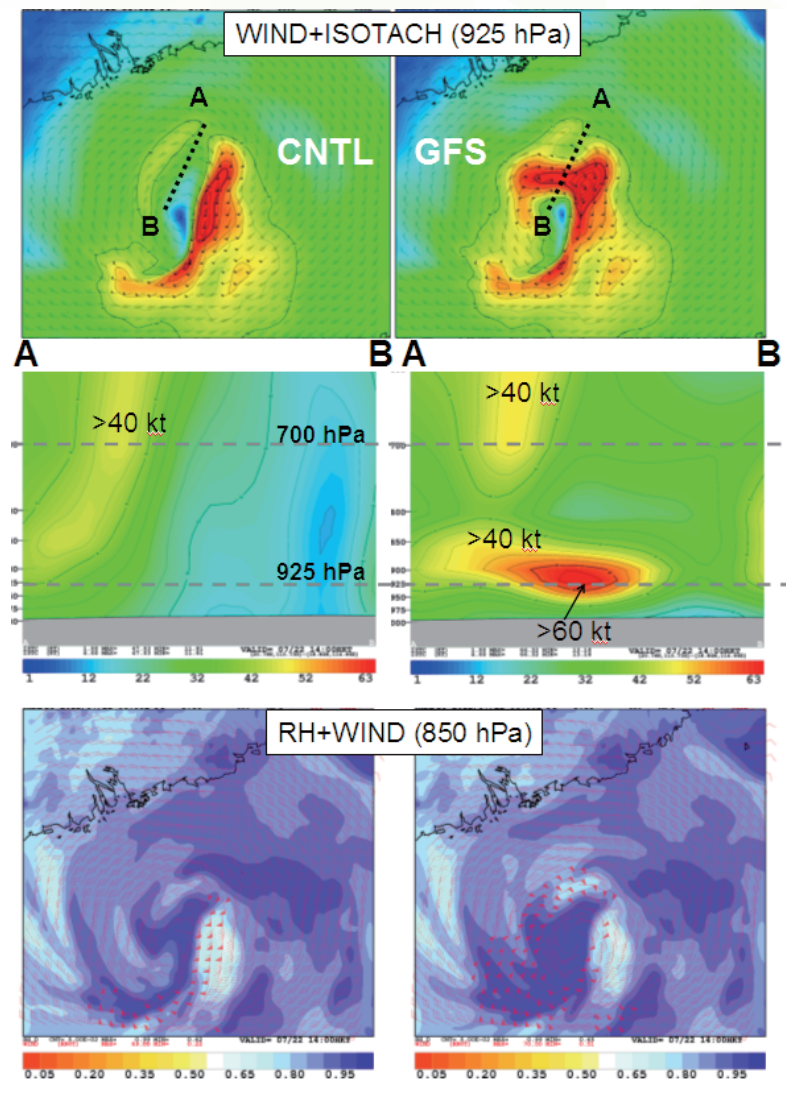


Fig. 29 Analysis of wind (wind speed denoted in colour) at 925 hPa (top), cross section from surface up to about 600 hPa along line AB (middle), and analysis of RH and wind at 850 hPa (bottom) from the control experiment (CNTL, left) and with GFS data assimilated (GFS, right).

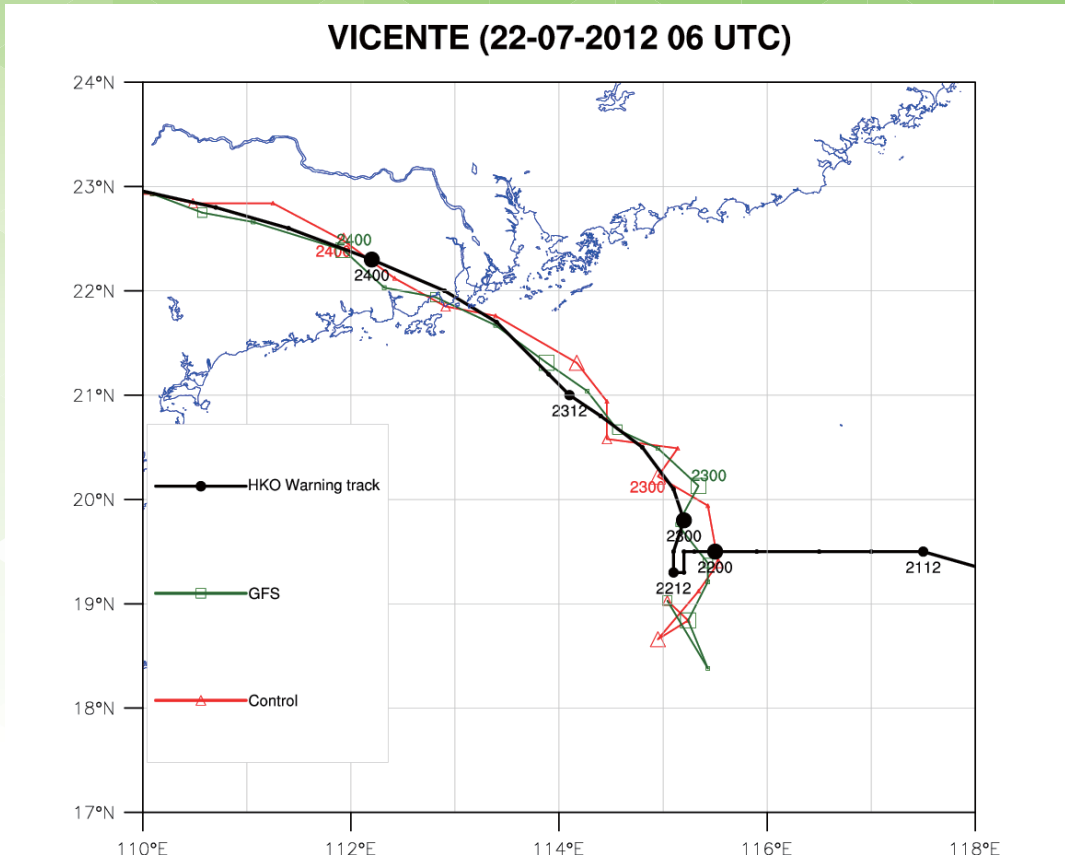


Fig. 30 Forecast tracks of Vicente from the Control (red) and GFS (green) experiments

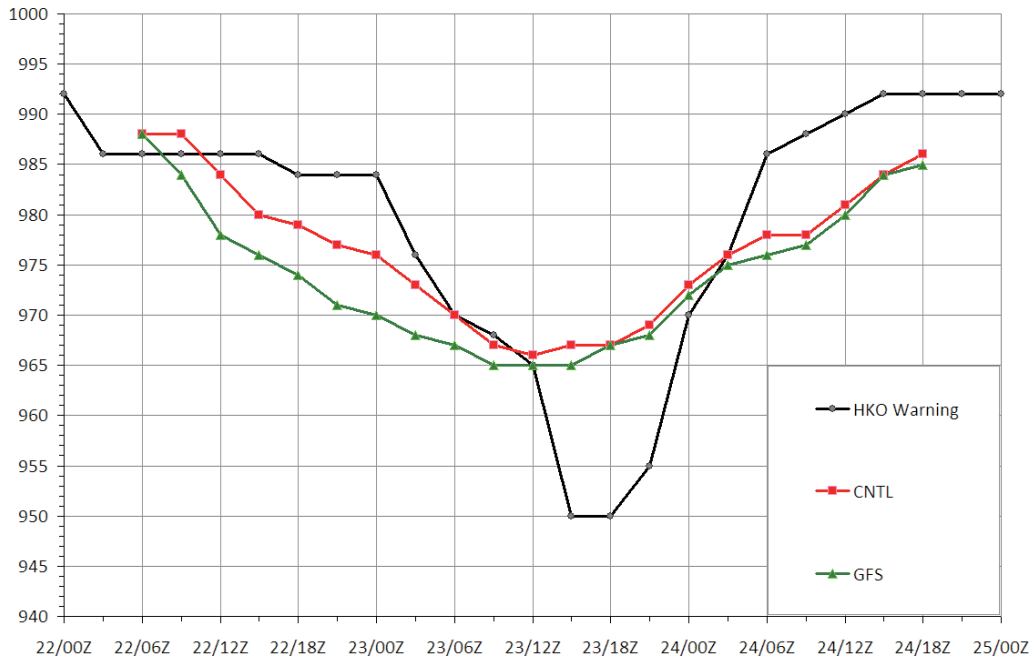


Fig. 31 Time series of 3-hourly forecast intensities by the Control (red) and GFS (green) experiments.

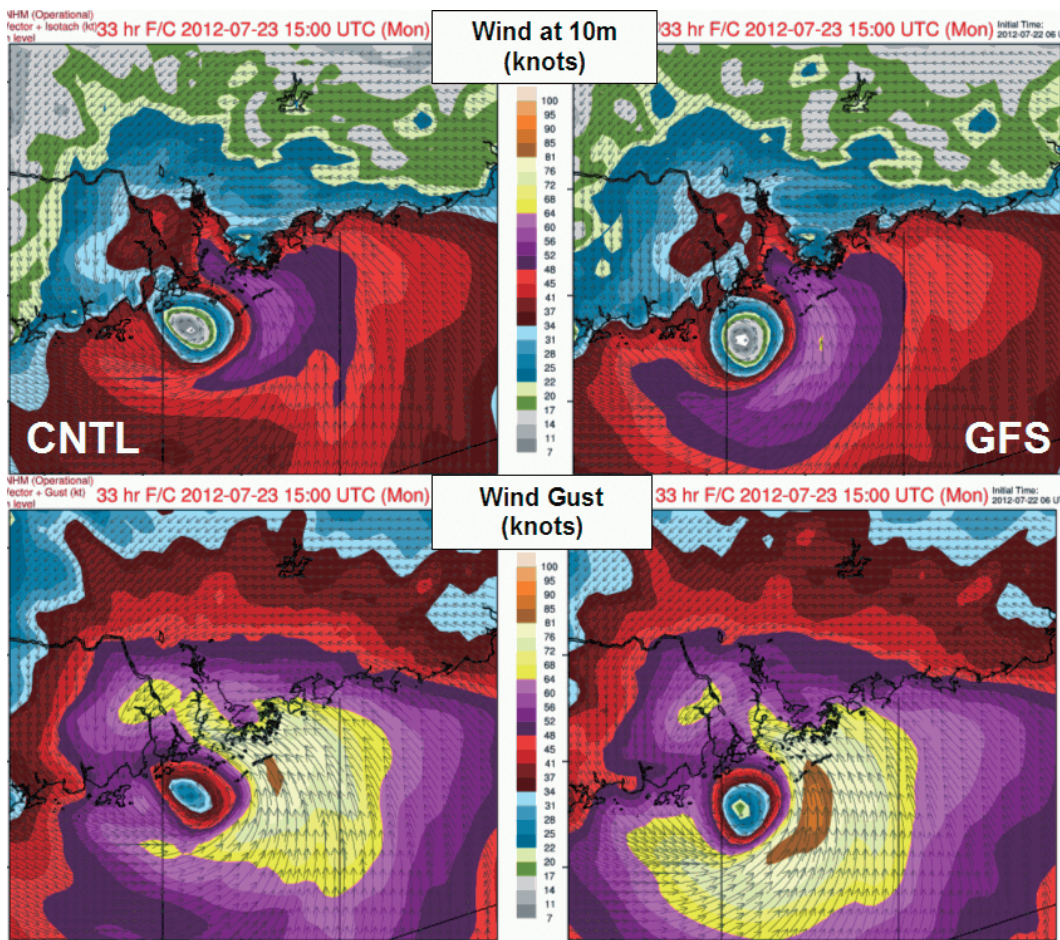


Fig. 32 33-hour forecasts of surface wind (top) and gusts (bottom) in the vicinity of Vicente at 1500 UTC, 23rd July 2012 by the Control (left) and GFS experiments (right).

A Study of Tropical Cyclone Rainfall Distribution and Topographic Effect over Hong Kong

H.Y. Yeung¹, P.W. Cheng² and S.T. Chan¹

¹ Hong Kong Observatory

² City University of Hong Kong

Abstract

The terrain of Hong Kong is hilly and rugged, with the tallest peak, Tai Mo Shan, reaching nearly 1,000 metres high. The map of mean annual rainfall distribution in Hong Kong reveals that the climatological rainfall maxima align nicely with the major mountain ranges in the territory. One of the mechanisms by which the orographic enhancement of rainfall occurs is the high winds due to tropical cyclones approaching the south China coast. In this study, a total of 36 tropical cyclones that affected Hong Kong during 1999-2010 were submitted to statistical analysis. The average radar reflectivity over Hong Kong was first computed and converted into mean rainfall-rate distribution. The results were analyzed and categorized according to different wind regimes. Orographic enhancement factors were then computed based on the mean rainfall rates at each analysis grid point. The results show that all the mean rainfall fields and enhancement factor maps exhibit characteristic maxima closely tied to the terrain peaks, with detailed locations dictated by the prevailing wind direction, and the magnitude of enhancement controlled mainly by the wind speed. Looking ahead, the Observatory will further explore how such results can be applied to rainfall nowcasting.

1. Introduction

In Hong Kong, tropical cyclone (TC) rainfall has long been studied. The first comprehensive statistical study covering the years 1884-1939 and 1947-1970 was released by the Hong Kong Observatory as a Technical Note [1] in 1974. The effect of orography on rainfall in Hong Kong was reported for the first time in 1955 by Ramage and Bell [2]. With the advent of weather radar, the first radar climatological study was performed in 1973 by Cheng and Kwong [3]. They analyzed the observations from a Plessey Type 43S Radar (10 cm wavelength) to study the diurnal, daily, and monthly variations of radar echo coverage in Hong Kong during the period 1967-1969. Over the past 10 years or so, rainfall data from Doppler weather radar and dense rain gauge networks in Hong Kong have become accessible. The availability of such high-resolution rainfall information allows us to revisit the above issues from a fresh angle and, hopefully, gain deeper insights from the results.

Hong Kong is small in area but complex in topography. As shown in Fig. 1, there are

numerous mountain ranges with significant altitudes scattered all over the territory. The highest peak, Tai Mo Shan, is 957 m above mean sea level (labeled TMS in Fig. 1(a)). Fung Wong Shan (or Lantau Peak) is the other peak in Hong Kong with an altitude of over 900 m (labeled FWS in Fig. 1(a)). In the eastern part of Hong Kong, the mountain ranges are also significant, with Ma On Shan (labeled MOS in Fig. 1(a)) around 700 m above mean sea level. From the annual mean rainfall analysis over Hong Kong shown in Fig. 1(b), it is evident that the climatological maxima are closely tied with these three mountain ranges. The orographic effect can be prominent under strongly forced situations, as when a TC approaches the south China coast and brings high winds to Hong Kong. Depending on the track and intensity of an approaching TC, different wind regimes can result. Orographic lift, and therefore rainfall enhancement, is expected to occur over the parts of the mountain ranges that face the prevailing wind.

2. Data Sets

Thirty-six TC cases during 1999–2010 were selected for the present study. These include all the TCs that came within 256 km of the Hong Kong Observatory's TMS weather radar since it began operation in 1999. The time that a TC spent within this proximity (referred to as "proximity period" hereafter) ranges from a few hours to over two days, with an average of about 20 hours. The maximum local winds brought about by these TCs vary from strong to hurricane force, with directions spanning the compass.

The radar reflectivity data were provided by the TMS Doppler weather radar, which is an S-band radar. The radar volume scan is updated every 6 minutes. Basic quality control is applied to the raw radar data to remove clutter. The reflectivity data at a constant altitude of 2 km above sea level are used to compute the climatological distributions. Discounting the missing or corrupted data, the total number of radar scans available is 6,529. To allow direct comparison with the rain gauge observations (R), the reflectivity (Z) is converted to rainfall rate using the following climatological Z-R relation:

$$Z = aR^b, \text{ where } a = 228.82, b = 1.33 \quad (1)$$

The values of the parameters a and b are determined by linear regression analysis on the ($\log Z$, $\log R$) data pairs from all 36 proximate TCs.

The rain gauge observations were collected from the automatic rain gauge networks in Hong Kong. Currently, there are 157 rain gauges available, covering a total land area of about 1,100 km² in Hong Kong. The rain gauges have a data resolution of 0.5 mm and the data are reported at 5-minute intervals. To allow direct comparison with the rainfall rates deduced from radar reflectivity, we took the 5-minute rain gauge accumulations as an estimate for instantaneous rainfall rate and multiplied the values by 12 to convert them to units of mm/h. The required climatological distributions were then obtained and gridded to the same rectangular grid covering Hong Kong (252 × 217 at 0.267 km spacing) as for interpolating the radar using the Kriging analysis technique [4].

3. Rainfall Data Processing Methodology

Fig. 2 shows the combined wind rose for the

36 TC cases, derived from the 10-minute mean wind reports collected at 13 representative anemometer stations in Hong Kong. These stations, denoted by blue circles in Fig. 1, are all located near sea level. The wind rose reveals that the percentage of high winds (over force 6 on the Beaufort scale) amounts to less than 10%. A simple average over the entire data set may not be able to delineate clearly the full effects of orographic enhancement due to high winds. To this end, the observation data were stratified into eight basic wind sectors according to the directions on an 8-point compass. Here, the wind direction for data grouping refers to the average wind direction determined by taking the vector mean of the 10-minute mean winds reported at the same 13 anemometer stations. As also hinted by the wind rose in Fig. 2, some wind directions are naturally preferred over others, so the wind sectors are therefore grouped further into 4 mutually exclusive regimes, namely north plus northeasterly, east plus southeasterly, south plus southwesterly, and west plus northwesterly (denoted respectively by their usual symbols as N+NE, E+SE, S+SW, and W+NW). With these combinations, the statistical significance in each regime can be enhanced. All radar and rain gauge data are classified and averaged accordingly.

While the climatological mean of rain gauge rainfall rates is computed as the arithmetic average over all available data, calculating the mean of the radar rainfall rate is not trivial. There are at least two ways to calculate it: (a) first averaging Z over different radar scans, then converting the result to a mean rainfall rate using Eq. (1); (b) first converting Z of an individual radar scan to R , then averaging the results to get the mean rainfall rate. Because the conversion formula of Eq. (1) is nonlinear, the two calculation methods will lead to different results in general. Comparing the results of both methods to those obtained from rain gauge data, we note that method (a) generally overestimates the mean rainfall rates and conclude that (b) produces more reasonable estimates. For the rest of this paper, all radar rainfall rates refer to those obtained based on method (b).

4. Major Results

Fig. 3(a) shows the overall distribution of mean rainfall rates derived from the radar reflectivity data. Although the spatial pattern aligns quite nicely with the climatological

rainfall distribution shown in Fig. 1(b), the orographic enhancement is not very prominent in Fig. 3(a). To delineate more clearly the effect of terrain, in Fig. 3(b) we plot the frequency distribution of radar reflectivity higher than 40 dBZ, which is equivalent to about 17 mm/h according to Eq. (1). It is evident from the frequency plot that the areas of stronger reflectivity or higher rainfall rate are all clustered around the three major mountain ranges mentioned in Section 1. Note that there are two weak-echo sectors in the southeast quadrant of all the radar-based mean fields due to obstructions close to the radar at TMS.

To see the effect of different flow directions, the mean rainfall rates in the four wind direction regimes are plotted in the left-hand column of Fig. 4. Also plotted in the right-hand column of Fig. 4 are the corresponding rain gauge rainfall rates. It is noted that the mean radar rainfall rates are generally higher than the mean rain gauge rainfall rates. Several factors contribute to this difference, including (a) the current Z-R calibration algorithm focuses on heavy rain and might not be able to handle low-rainfall-rate situations optimally; (b) while all zero observations from rain gauges have been included in calculating the mean rainfall rates, only radar reflectivity at 10 dBZ (equivalent to about 0.1 mm/h) or above was used; and (c) the use of a 5-minute accumulation of rainfall to represent the instantaneous rainfall rate could lead to an underestimation. Although the absolute values in the two sets of mean rainfall rates are different, the locations of the major enhancement areas are similar. The maxima seen in different wind regimes correlate well with the mountain ranges that face the corresponding wind directions. It can also be seen that in general heavier rain fell over Hong Kong during the S+SW and W+NW regimes.

To appreciate the effect of wind speed on orographic enhancement, the samples in each wind direction regime are further divided into three wind-speed classes: force 0-4 (calm-moderate), 5-7 (fresh-strong) and 8 (gale) or above. The results are plotted in Fig. 5. It is apparent that the higher the wind speed, the more prominent the orographic effect. Plotted in Fig. 6 are the distributions in the windiest class stratified according to wind direction regimes. Under such high wind conditions, the mean rainfall rates over mountainous areas generally become much more intense than those shown in Fig. 4 for all wind direction regimes.

5. Orographic Enhancement Factor

The Hong Kong Observatory operates a rainfall nowcasting system known as SWIRLS (Short-range Warning of Intense Rainstorms in Localized Systems [5]-[6]) for predicting the rainfall distribution in the next few hours over Hong Kong and nearby regions based on extrapolation of the motion of radar echoes. To improve the rainfall nowcast by considering the orographic enhancement as well, we need to quantify the degree of such enhancement. To this end, we introduce the following definition of an orographic enhancement factor f for a given wind direction regime d and speed class u :

$$f_{d,u}(i, j) = \frac{\bar{R}_{d,u}(i, j) - S_{d,u}}{S_{d,u}} \quad (2)$$

In Eq. (2), \bar{R} denotes the climatological mean rainfall rate as defined in Section 3, S the spatial average of \bar{R} over the analysis grid or rain gauge network, and (i, j) the coordinates of the point of interest. Fig. 7 shows the maps of the orographic enhancement factor for the windiest class in the four wind direction regimes based on both radar (left column) and rain gauge (right column) data.

6. Discussion

We have presented two sets of orographic enhancement maps using both radar and rain gauge data, each of which has its pros and cons. In general, the radar-based maps show finer spatial structure and cover most parts of the analysis domain, except for the blocked sectors due to obstructions to the radar and the cone of silence very close to the radar site at TMS. On the other hand, the estimations based on rain gauge observations in those areas void of reflectivity are more reliable, as the gauge measurements over such areas are reasonably adequate. The main drawbacks of the rain gauge-based maps include an oversmoothed spatial structure from use of the Kriging algorithm and unreliable estimations near and over water due to the lack of rain gauge observations. To take advantage of both data sets, a combined orographic enhancement factor map is explored by simply taking the maximum of the two enhancement factors at every grid point. This strategy is targeted to cover the worst-case scenario in potential rainstorm situations. Fig. 8 shows the results

of combining the maps in Fig. 7 using such a strategy.

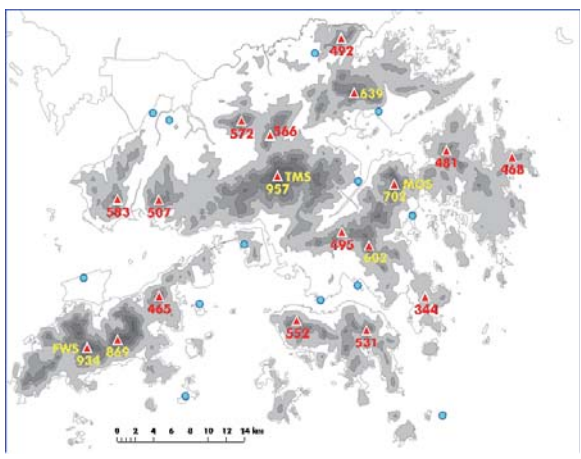
As shown in Fig. 7 and Fig. 8, there are some regions of reduced rainfall rate (negative enhancement factor) over land, especially in the S+SW regime. Whether such reductions are due to a genuine physical mechanism or are simply a reflection of the natural distribution of TC rainbands is not clear from the present results. If the former is the case, a nowcasting algorithm has to take account of such reduction. But for the latter, one can choose to apply the factor preferentially over the positive enhancement areas only.

7. Concluding Remarks

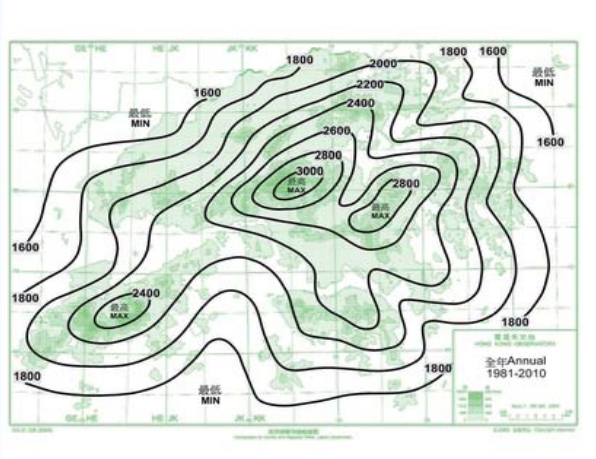
Based on a set of 36 proximate TCs during 1999-2010, mean rainfall rates over Hong Kong were derived from both radar reflectivity and rain gauge data and were analyzed according to wind direction regimes and speed classes. Orographic enhancement characteristics were studied and quantified in terms of a dimensionless orographic enhancement factor. The enhancement factor maps thus derived can provide an objective basis for adjusting the rainfall rate field required in rainfall nowcasting. Looking ahead, the Observatory will carry out rainfall nowcasting experiments to study how to apply and evaluate the effectiveness of the orographic enhancement maps in an operational environment.

References

- [1.] Kwong, W.P., 1974: Tropical cyclone rainfall in Hong Kong. *Hong Kong Observatory Technical Note*, No. **38**.
- [2.] Ramage, C.S. and G.J. Bell, 1955: Artificial and orographic stimulation of rainfall in Hong Kong. *Hong Kong Observatory Technical Note*, No. **13**.
- [3.] Cheng, T.T. and W.P. Kwong, 1973: Radar climatology of Hong Kong for the years 1967-1969. *Hong Kong Observatory Technical Note*, No. **34**.
- [4.] Yeung, H.Y., C. Man, S.T. Chan and A. Seed, 2011: Application of radar-rain gauge co-Kriging to improve QPE and quality control of real-time rainfall data. *Proceedings of the International Symposium on Weather Radar and Hydrology*, Exeter, U.K., 18-21 April 2011.
- [5.] Li, P.W. and E.S.T. Lai, 2004: Short-range quantitative precipitation forecasting in Hong Kong. *J. Hydrology*, **288**, 189-209.
- [6.] Yeung, Linus H.Y., W.K. Wong, Philip K.Y. Chan and Edwin S.T. Lai, 2009: Applications of the Hong Kong Observatory nowcasting system SWIRLS-2 in support of the 2008 Beijing Olympic Games. *WMO Symposium on Nowcasting*, Whistler, B.C., Canada, 30 Aug-4 Sep 2009.



(a)



(b)

Fig. 1 Terrain map (a) and mean annual rainfall map (b) of Hong Kong. Topography is shown as shaded contours at 125-m intervals. Major peaks are marked by red triangles with altitudes annotated in metres. The anemometer stations used in this study are marked by blue circles. The rainfall distribution refers to the period 1981-2010.

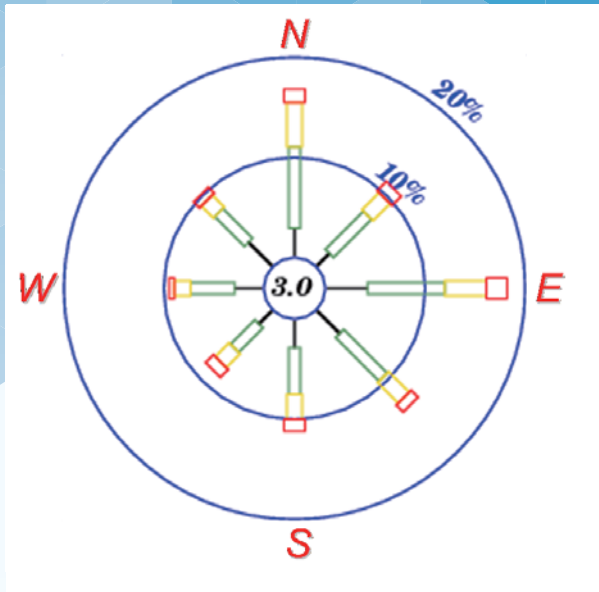
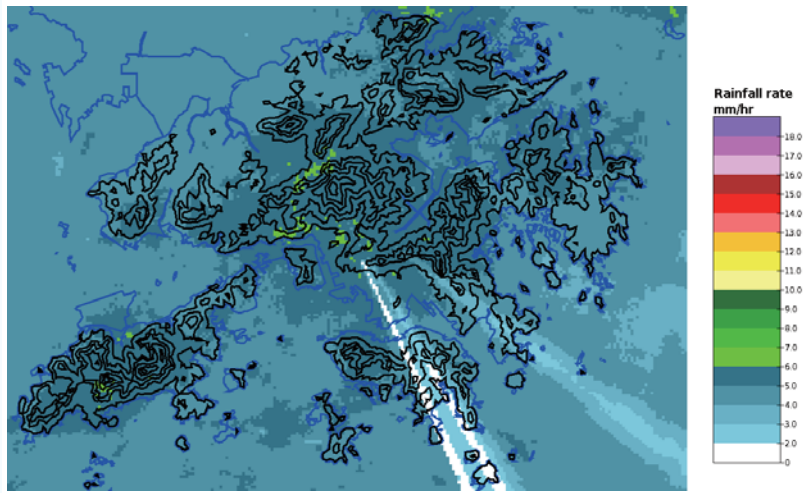


Fig. 2 Wind rose plotted for the 36 TC cases within Hong Kong's proximity range during 1999-2010. The black, green, yellow, and red lines/boxes refer to wind-speed classes of force 1-2, 3-4, 5-6, and over 6 on the Beaufort scale, respectively. The number in the middle (3.0 %) indicates the percentage of calm and variable winds. The percentages of occurrence of the four wind-speed classes (irrespective of direction) are 21.9, 44.1, 21.7, and 9.3 %, respectively. When partitioned according to the 8-point compass (from N to NW round the compass, irrespective of wind speed), the proportions become, respectively, 16.6, 10.8, 18.0, 13.1, 11.0, 8.2, 9.3, and 10.0 %.

(a)



(b)

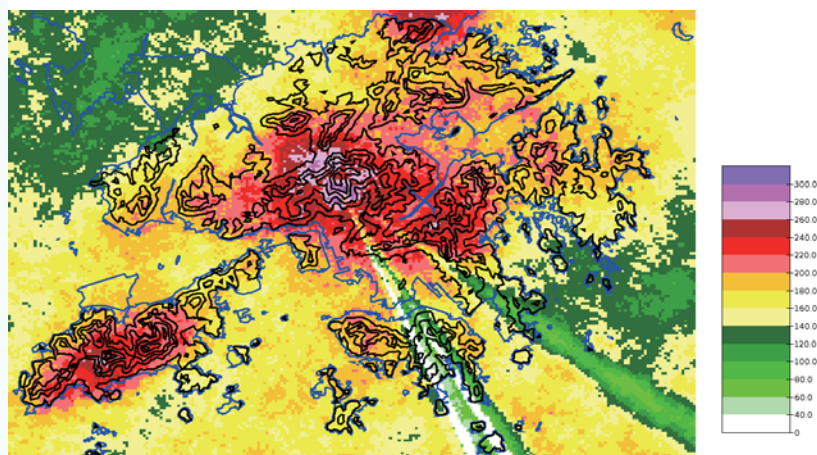


Fig. 3 Radar climatology over all 36 proximate TCs in 1999-2010: (a) mean radar rainfall rate; (b) frequency distribution of mean radar reflectivity over 40 dBZ. Note that the two weak/blank sectors common to all maps are due to obstructions close to the radar at TMS.

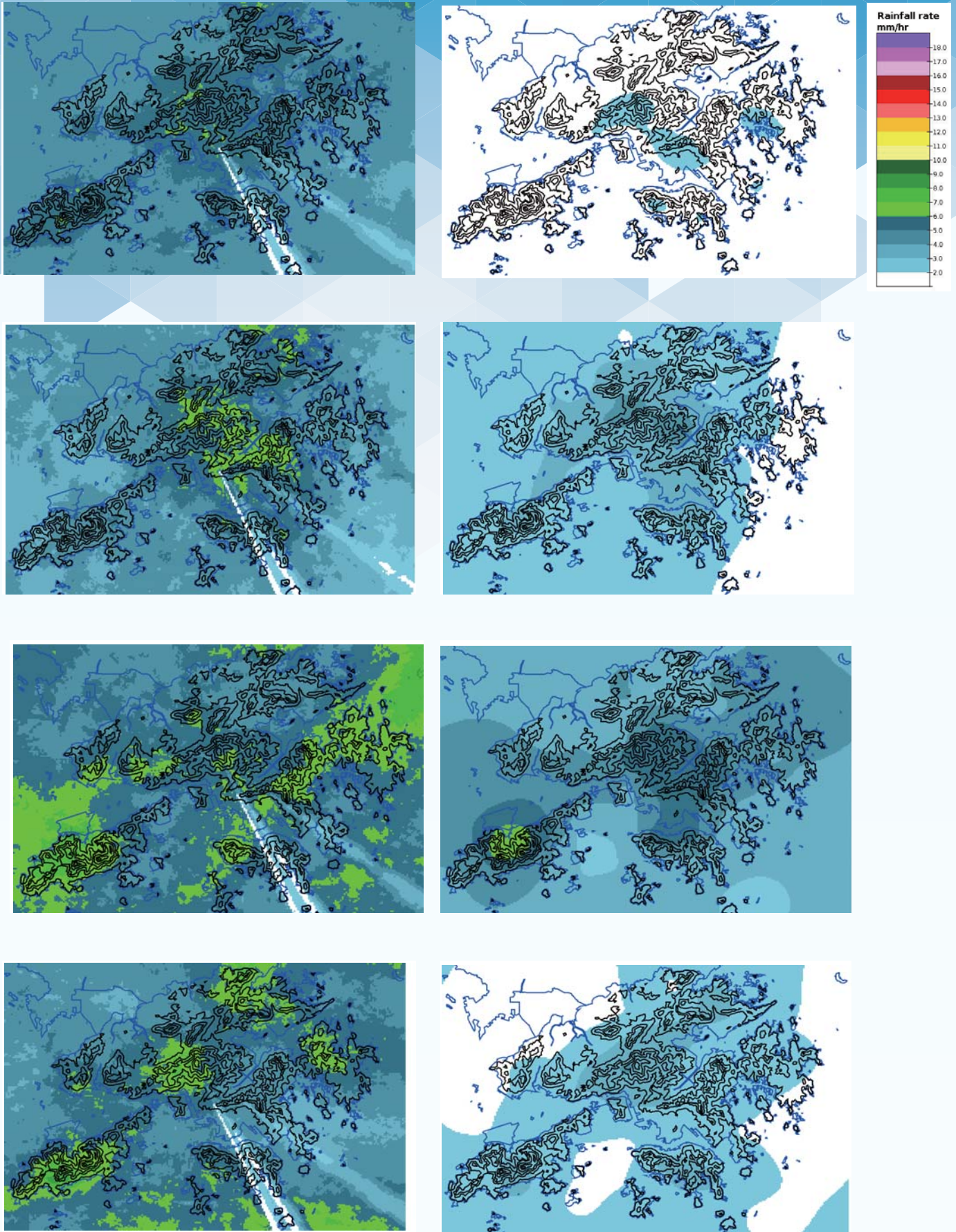


Fig. 4 Mean radar rainfall rates (left column) and mean rain gauge rainfall rates (right column) for the four wind direction regimes (from top to bottom) N+NE, E+SE, S+SW, and W+NW, respectively

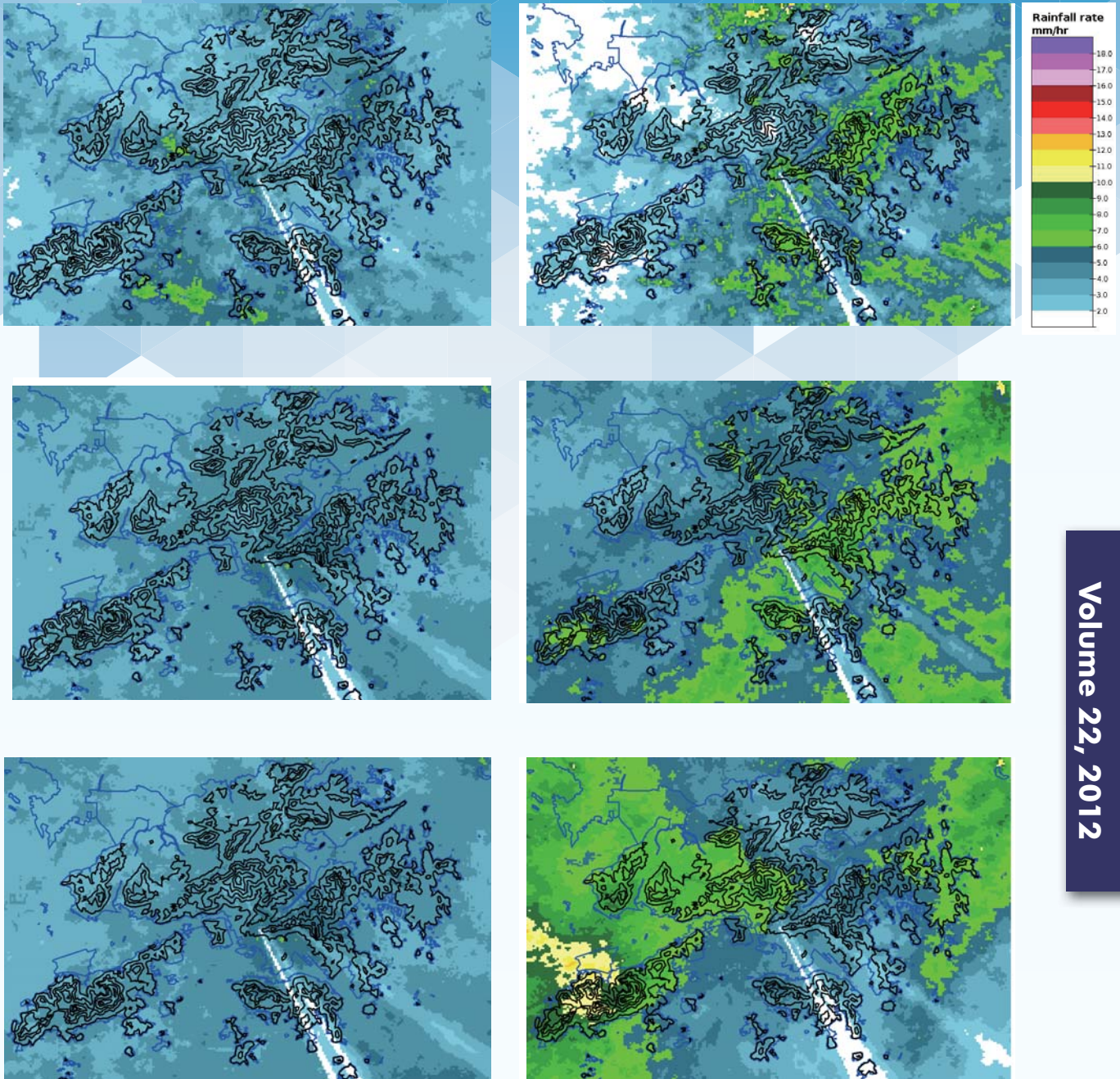


Fig. 5 Mean rainfall rates calculated for three wind speed classes: force 0-4 (top row), 5-7 (middle row), and 8 or above (bottom row). The left column refers to distributions irrespective of wind direction, and those in the right column are specific to the S+SW regime. Note that the number of samples after speed stratification becomes 1,282, 3,040, and 2,207 (left column, top to bottom) and 226, 506, and 405 (right column, top to bottom), respectively.

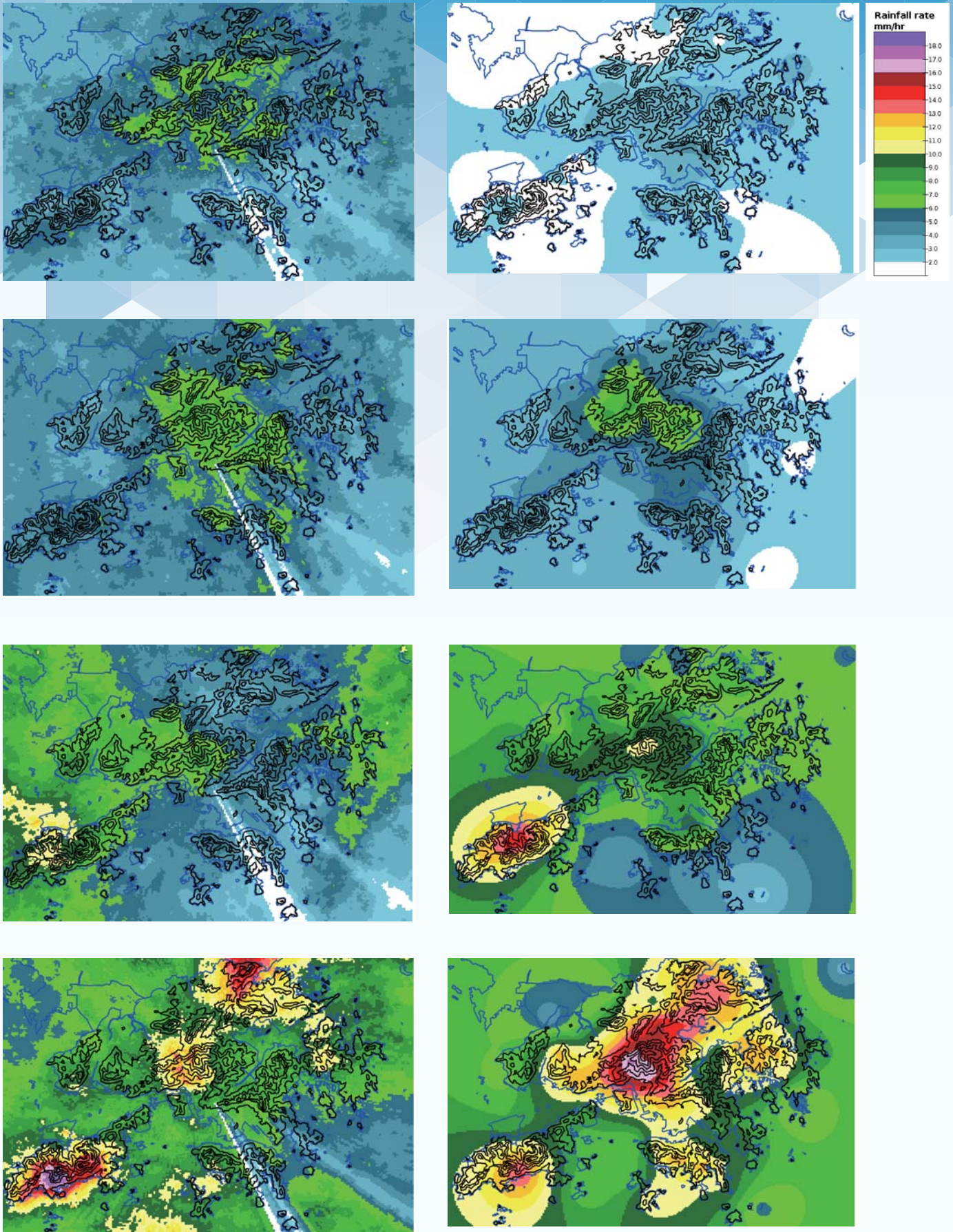


Fig. 6 Same as Fig. 4, except that the distributions refer to the windiest class. Note that the number of samples in the four regimes reduces to 740, 837, 405, and 225, respectively

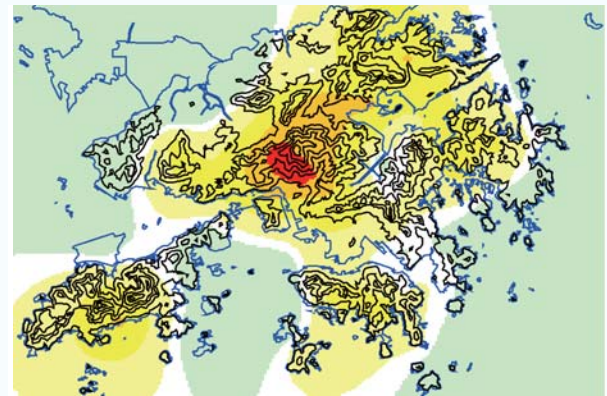
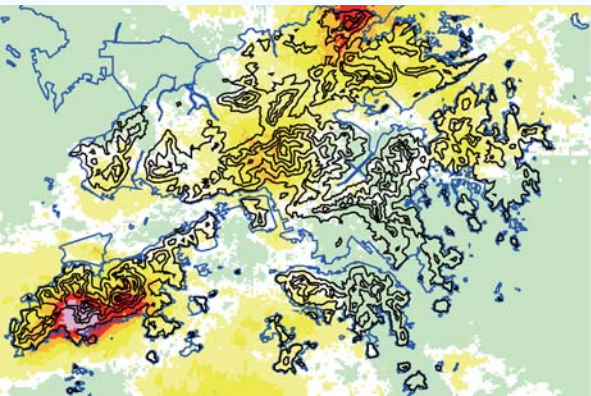
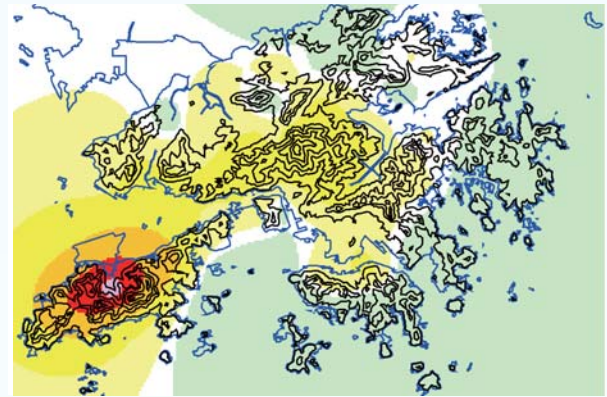
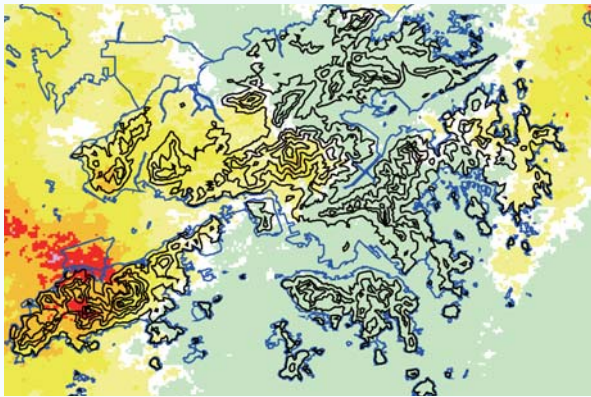
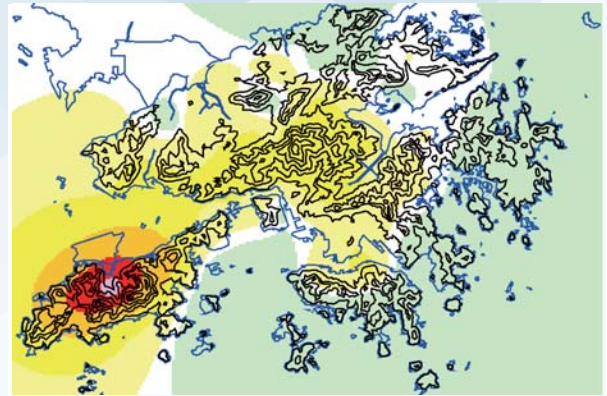
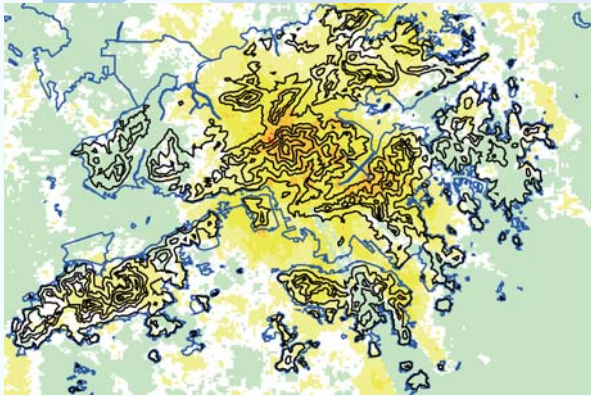
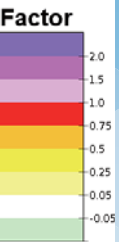
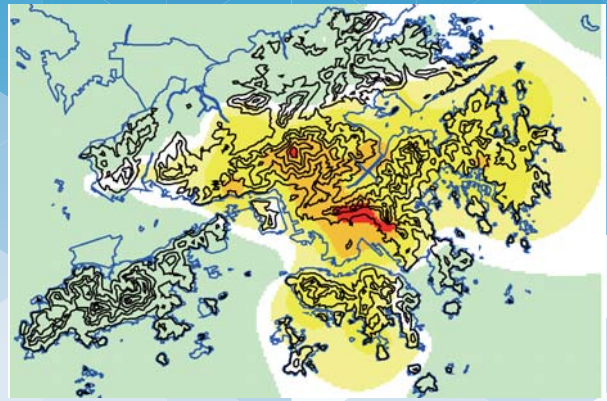
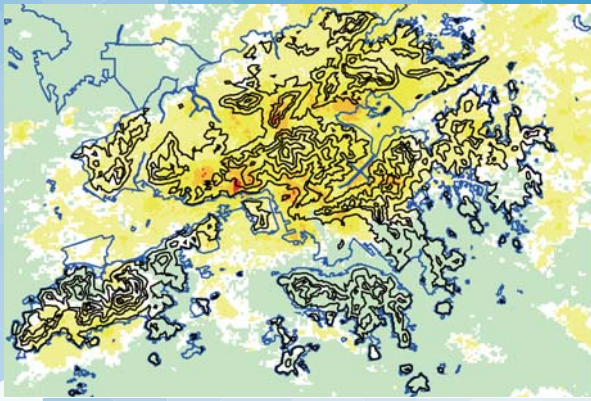


Fig. 7 Same as Fig. 6, except that the colour contours refer to the orographic enhancement factor

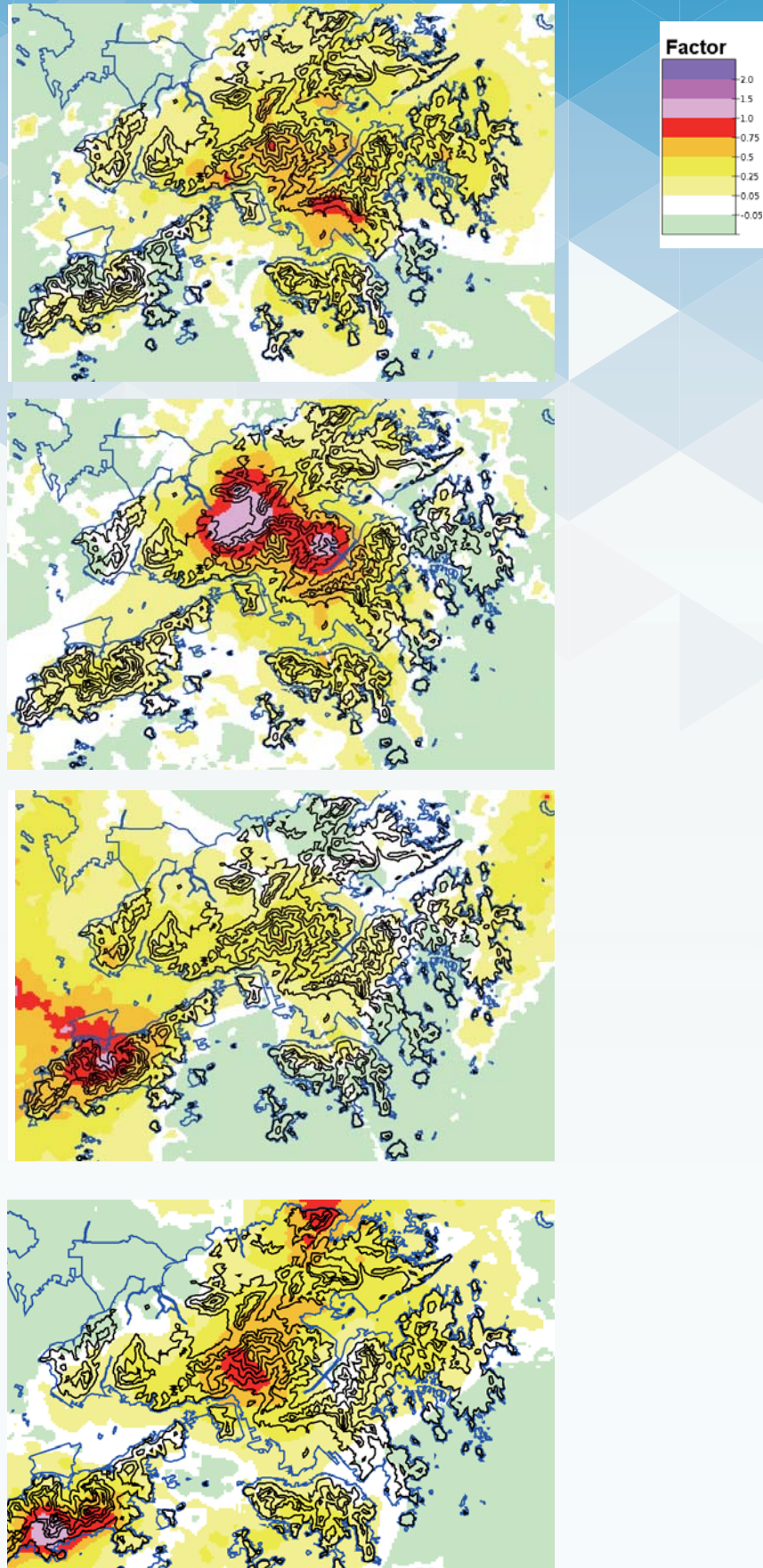


Fig. 8 Combined (maximum) orographic enhancement maps for the four wind regimes (from top to bottom), N+NE, E+SE, S+SW, and W+NW, in the windiest class.

A Review of Climate Change Studies for Southern China

LEE Sai-ming¹, LIU Jin-luan², TONG Si-man³

¹Hong Kong Observatory

²Guangdong Climate Center

³The Meteorological and Geophysical Bureau of Macao

Abstract

Climate change has become a major challenge of our time. Each of the last three decades has become successively warmer. The first decade of the 21st century has been the warmest since 1850. The warming of the climate system is expected to continue in the future with the unabated increase in the atmospheric concentration of greenhouse gases. Against a backdrop of global warming, the climate of China overall has also experienced a warming trend, and southern China is no exception. As southern China is densely populated, the impact of climate change there should not be overlooked. In this connection, the meteorological authorities of Guangdong, Hong Kong, and Macao have conducted climate change studies to understand the impacts of climate change on southern China. This paper presents a concise summary of the climate change studies conducted by the meteorological authorities of Guangdong, Macao, and Hong Kong in recent years, revealing the changes in climate and extreme weather in different parts of southern China.

1. Introduction

Given the dense population and the vibrant economy in southern China, climate change will inevitably impact its natural environment and agricultural output (Du *et al.*, 2004; Du *et al.*, 2010). In recent years, meteorological authorities of Guangdong, Hong Kong, and Macao have conducted in-depth climate change studies on various meteorological variables such as temperature and rainfall over the past several decades or the past century. A concise summary of these studies is presented in this paper, with Section 2 highlighting the observed climate change in the past several decades, Section 3 discussing the observed changes in extreme weather events, and Section 4 providing a conclusion and discussion.

2. Observed climate change

2.1. Temperature

The warming trends over Guangdong, Macao, and Hong Kong, as well as the global average, are tabulated in Table 1. The warming trends in the past few decades over Guangdong, Hong Kong, and Macao were 0.21 °C per decade (Composing Team for Assessment Report on Climate Change of Guangdong, 2007), 0.16 °C per decade (Ginn *et al.*, 2010), and 0.10 °C per decade (Fong *et al.*, 2009), respectively. The warming rate of Macao was slightly lower than that of Guangdong and Hong Kong, which

could be a reflection of the slower pace of urbanization in Macao.

Chen *et al.* (2006) analyzed the temperature trend of Guangdong in the past 50 years and found abrupt warming in 1987 and 1998. Du *et al.* (2004) also pointed out that the rate of temperature increase became more pronounced after the 1970s. Tang (2008a) and Ginn *et al.* (2010) examined the time series of temperatures of Macao and Hong Kong, respectively (Table 1 and Figure 1), pointing out that the rate of temperature increase apparently accelerated in the 1970s and 1980s, which could be attributed to rapid urbanization during these periods in addition to global warming.

Seasonally speaking, the warming trend over Guangdong in the past 50 years was the highest in winter (0.36 °C per decade) and the lowest in summer (0.14 °C per decade) (Composing Team for Assessment Report on Climate Change of Guangdong, 2007). Chen *et al.* (2006) compared the temperature changes over Guangdong during 1987-2004 against the average of 1971-2000 and found that the warming was largest in winter (0.6 °C) but smallest in summer (0.2 °C). The warming in spring and autumn was 0.4 °C and 0.3 °C, respectively. After the 1990s, the warming trend in spring apparently accelerated (Figure 2). Tang (2008a) compared the warming trends of Macao in different seasons and found

that the warming trend of 0.11°C per decade in spring was the largest, followed by 0.08°C per decade in winter. The warming trend was relatively small in summer and autumn. For Hong Kong, the increasing trend of yearly maximum temperature (0.09°C per decade) was lower than that of yearly minimum temperature (0.14°C per decade) during 1885-2005 (Wong *et al.*, 2010), suggesting that warming in summer was less than that in winter. Overall, the warming trend in winter was more apparent, while the trend in summer was relatively small.

Du *et al.* (2004) compared the annual average daily maximum temperature and the annual average daily minimum temperature in recent decades. It was found that the annual average daily maximum temperature over Guangdong showed little variation from the 1960s to the 1980s but exhibited a significant rising trend after the 1990s. The annual average daily minimum temperature had risen since the 1960s and the rate of change was increasing. Macao (Tang, 2008a; Fong *et al.*, 2009) and Hong Kong had similar observations. The increasing trend of the annual average daily maximum temperature was rather small (Macao) or insignificant (Hong Kong) in the 20th century, but the rising trend of the annual average daily minimum temperature was more prominent, leading to the reduction in diurnal temperature range (Figures 3 and 4). Besides global warming, urbanization contributed to this phenomenon as well. Karl *et al.* (1993) and Zhou *et al.* (2004) pointed out that the effect of urbanization on minimum temperature would be larger than that on maximum temperature.

In this connection, the urbanization effect on regions with relatively rapid economic growth such as the Pearl River Delta should not be overlooked, and quantitative assessment of the effect is needed. By comparing the yearly average diurnal temperature range between Guangzhou (urban station) and Foshan airport (rural station) in 1973-2003, Fan *et al.* (2005) estimated the warming rate due to urbanization in Guangzhou to be 0.13°C per decade. Leung *et al.* (2007) found that the difference in annual average temperature between the Hong Kong Observatory (HKO) headquarters and a rural station, Ta Ku Ling (TKL), during 1989-2006 was 0.81°C . Since the headquarters was located in a rural area a century ago, Leung *et al.* (2007) further assumed that the difference in annual average temperature between the headquarters

and TKL was zero at that time (1885) and thus estimated the warming trend due to urbanization to be 0.08°C per decade. This estimate was lower than that for Guangzhou in Fan *et al.* (2005), probably due to a longer period used in Leung *et al.* (2007). Fong *et al.* (2009) compared the annual mean temperature time series of Guangzhou, Hong Kong, and Macao during 1951-2007 and found that the warming trend of Macao was significantly lower than that of Guangzhou and Hong Kong (Figure 5). They argued that if Macao was taken as a rural station of Guangzhou and Hong Kong, then the warming rate due to urbanization for Guangzhou and Hong Kong would be 0.07°C per decade and 0.09°C per decade, respectively.

2.2. Rainfall

The Guangdong Climate Center (GDCC) indicates that the annual rainfall of Guangdong Province as a whole had a statistically insignificant increasing trend of 1.15 mm per decade from 1961 to 2006 (Figure 6a). Regionally, the eastern and southern (western and northern) parts of Guangdong saw insignificant increases (decreases) in annual rainfall (Figure 6b). The annual rainfall increased at a faster rate in the "post-flooding" period than in the "pre-flooding" period (Figure 6c). For Macao and Hong Kong, the annual rainfall did show an increasing trend over the past 100 years or so (Figures 7 and 8). However, the rainfall trend of Hong Kong became statistically insignificant after 1947, and the annual rainfall of Macao even showed a slight decrease after the 1970s (Tang, 2008a). In addition, large interannual variation of annual rainfall was noted at both locations. Seasonally, the increasing trend of rainfall in Macao was most prominent in summer. After the 1970s, the rainfall in both spring and autumn displayed a statistically insignificant decreasing trend. Tang (2008a) speculated that this could be related to less frequent cold air intrusion from the north and thus less frequent frontal rain.

Wu *et al.* (2011a) also analyzed the number of rain days and average rainfall intensity over southern China. They defined days with rainfall exceeding or equal to 0.1 mm as rain days and average rainfall intensity as annual rainfall divided by the number of rain days. It was found that the number of rain days decreased at a rate of 4.8 days per decade during 1961-2008 (Figure 9a), but the average rainfall intensity significantly increased at a rate of 0.4 mm per day per decade (Figure 9b). This finding

was consistent with the increasing number of flood events in Guangdong in recent years. In Macao, the rainfall intensity also showed an increasing trend (Tang, 2008a). In Hong Kong, the number of rain days has significantly declined but the number of heavy rain days (daily rainfall ≥ 30 mm) has significantly increased in the past 50 years (Figures 10 and 11), suggesting that rainfall intensity has been enhanced.

As for the urbanization effect on precipitation, Li *et al.* (2009) utilized satellite data such as TRMM and QuikSCAT to investigate the characteristics of spatial rainfall distribution over the Pearl River Delta and its vicinity. They found that precipitation over the urban regions was significantly more abundant than in neighboring areas at the same latitude. Mok *et al.* (2006) also had a similar finding, that the difference in annual rainfall between the urban and rural areas in Hong Kong was growing at a significant rate of 63 mm per decade (Figure 12). They hypothesized that this could be attributed to a more convective atmosphere due to an urban heat island effect and a higher number of condensation nuclei in the urban areas.

2.3. Visibility, cloud amount, and duration of sunshine

Wu *et al.* (2011b) analyzed surface observation data from 192 weather stations over southern China during 1961-2008 and found that the number of hazy days¹ significantly increased at a rate of 5.8 days per decade (Figure 13a). This increasing trend was most prominent over the Pearl River Delta, the northwestern part of Guangdong, and the central and northeastern parts of Guangxi. A peak value of 38.8 days per decade was centred at Shenzhen (figure not shown), suggesting a close relationship with rapid urbanization and economic development. Hazy weather² was rare in Macao before the 1990s, but the number of hazy hours increased at a rate of 37 hours per year after the 1990s (Figure 13b). Deteriorating visibility was also a concern in Hong Kong. During 1968-1987, there was no significant trend (53 hours per decade) in the annual number of hours of reduced visibility observed at HKO headquarters³. However, during 1988-2008, the trend increased to 554 hours per decade (Figure 13c). Visibility in Hong Kong correlates well with the concentration of suspended particles larger

than $2.5 \mu\text{m}$ in diameter (Leung and Lam, 2008), and the major sources of suspended particles in Hong Kong and southern China are linked mostly with human activities such as construction, vehicle exhaust, and coal-fired electricity generation.

Cloud amount over Hong Kong and Guangdong exhibited an increasing trend (Composing Team for Assessment Report on Climate Change of Guangdong, 2007; Ginn *et al.*, 2010), which could be attributed to an increase in the concentration of condensation nuclei (Ginn *et al.*, 2010). Along with the increase in cloud amount, sunshine duration also declined (Ginn *et al.*, 2010; Wu *et al.*, 2011c). The sunshine duration in Macao also displayed a decreasing trend after the 1960s (Fong *et al.*, 2010).

3. Observed changes in extreme weather

A changing climate leads to changes in the frequency of extreme weather events. Taking temperature as an example, the frequency of occurrence of extremely high (low) temperatures will increase (decrease) if the average temperature rises.

Wu and Du (2010a) investigated the variation in extremely high and extremely low temperatures at 110 weather stations over southern China during 1961-2008 and found that the warming trend of the yearly minimum temperature was faster than that of the yearly maximum temperature. In other words, the probability of extremely low temperature decreased. Wu and Du (2010b) found that the number of extremely strong and moderate cold surges⁴ gradually declined after the 1980s, while the occurrence of weak cold surges significantly increased.

The annual number of extremely hot days in Guangdong (daily maximum temperature $\geq 35^\circ\text{C}$) displayed a significant rising trend of 0.27 days per year (Composing Team for Assessment Report on Climate Change of Guangdong, 2007). On the other hand, the annual number of extremely cold days (daily minimum temperature $\leq 5^\circ\text{C}$) exhibited a significant decreasing trend. Hong Kong saw a similar trend, with the annual number of very hot days (daily maximum temperature $\geq 33^\circ\text{C}$) and hot nights (daily minimum temperature $\geq 28^\circ\text{C}$) increasing significantly and the number of cold days (daily minimum temperature \leq

¹ Visibility below 10 km caused by suspended particles based on GDCC's definition.

² Visibility below 5 km and relative humidity below 80% based on the definition specified by the Meteorological and Geophysical Bureau of Macao.

³ Visibility below 8 km, excluding fog, mist, rain, or relative humidity $\geq 95\%$, based on HKO's definition.

12 °C) decreasing significantly (Wong *et al.*, 2010). By applying the generalized extreme value theory, Wong *et al.* (2010) found that the return period of daily minimum temperature ≤ 4 °C increased from 6 years in the early 20th century to 163 years in the early 21st century. The number of very hot days in Macao (daily maximum temperature ≥ 33 °C) exhibited a multidecadal variation without any significant trend. Similar to Guangdong and Hong Kong, Macao showed a significant rising trend in the number of hot nights (daily minimum temperature ≥ 27 °C), while the number of cold days (daily minimum temperature ≤ 12 °C) significantly declined (Tang, 2008a).

For extreme precipitation, the number of rain events of hourly rainfall ≥ 40 mm in Guangdong increased from 1.3 in the 1960s to 1.8 in recent years (Composing Team for Assessment Report on Climate Change of Guangdong, 2007). In Macao, the frequency of occurrence of daily rainfall ≥ 20 , 50, and 100 mm significantly increased in the 20th century. The return period of daily rainfall ≥ 250 mm shortened from 30 years in 1901-1930 to 5 years in 1978-2007. The frequency of occurrence of extreme hourly, two-hourly, and three-hourly rainfall in Hong Kong also increased significantly in the past century. The return period of hourly rainfall ≥ 100 mm shortened from 37 years in the early 20th century to 18 years in the early 21st century. The hourly rainfall record at the HKO headquarters has been broken more frequently in recent times (Figure 14), reflecting the increasing likelihood of extreme rainfall.

4. Conclusion

Against a backdrop of global warming, various aspects of climate change impact were studied and observed over southern China. In summary, the research results of meteorological authorities in Guangdong, Hong Kong, and Macao showed:

Temperature

- 1.) in the past 50 years or so, the increasing trends of temperature in Guangdong, Hong Kong, and Macao were all significant, albeit with different magnitudes;
- 2.) the rate of temperature rise accelerated in the 1970s and 1980s;
- 3.) the warming trend was more prominent in winter but relatively mild in summer; and

- 4.) the increase in daily maximum temperature was smaller than that in daily minimum temperature, with urbanization being a factor on top of global warming, and the extent and pace of urbanization leading to regional differences in temperature increase.

Precipitation

- 1.) the changes in annual rainfall over southern China in the past 50 years or so were less coherent than temperature changes, and there were regional differences;
- 2.) in Macao, the increasing trend was significant in summer, but the decreasing trends in spring and autumn were insignificant; and
- 3.) the number of rain days in southern China significantly decreased, but average rainfall intensity increased.

Other meteorological variables

- 1.) visibility over southern China significantly deteriorated, mainly due to human activities; and
- 2.) cloud amount increased and the duration of sunshine decreased.

Extreme weather

- 1.) extremely hot events became more frequent while extremely cold events became rarer; and
- 2.) intense rainfall became more frequent, and return periods of extreme rainfall events shortened.

Macao and Hong Kong have century-long meteorological data records, while Guangdong has had a dense observation network since the 1950s. Such data records with extensive spatial coverage provide precious information for climate change research, and the meteorological authorities of Guangdong, Hong Kong, and Macao will all benefit from closer collaboration. A data-sharing platform will facilitate the comparison of climate information, and in terms of methodology, adopting a common reference period for climate studies will render the comparison of results more direct and meaningful. Owing to climatological differences, the definition of extreme weather events may vary from region to region. For comparison purposes, changes in the return periods of extreme weather events need to be reliably analyzed to facilitate interpretation and application of the study results.

Reference

- Chen X., G. Qian, T. Chen, C. Li and K. Yu, 2006: Characteristics of climate warming and impact on climate belts change in Guangdong. *J. Trop. Met.* 22(6) 547-552 [in Chinese].
- Composing Team for Assessment Report on Climate Change of Guangdong, 2007: Assessment report on climate change of Guangdong (selection). *Guangdong Meteorology*, 29(3) 1-7 [in Chinese].
- Du, Y., L. Song, H. Mao, H. Tang and A. Xu, 2004: Climate warming in Guangdong Province and its influences on agriculture and the adaption measures. *J. Trop. Met.* 20(3), 302-310 [in Chinese].
- Du, Y., H. Duan and L. Tang, 2010: Adaptability of citrus in subtropics of China under future climatic scenario. *Chinese Journal of Ecology*, 29(5) 833-839 [in Chinese].
- Fan, S., J. Dong, L. Guo, A. Wang, L. Song, A. Liu and J. Xie, 2005: A study on the urbanization effect on the temperature of Guangzhou city. *J. Trop. Met.*, 21(6) 623-627 [in Chinese].
- Fong *et al.*, 2009: Analysis of surface air temperature change in Macao during 1901-2007. *Advances in Climate Change Research*, 5(1), 12-17 [in Chinese].
- Fong, S. K., C. S. Wu, A. Y. Wang, T. Wang, X. J. He, K. C. Leong, J. Liu and B. Q. Leong, 2010: Multiple time scale analysis of climate variation in Macao during the last 100 years. *J. Trop. Met.*, 26(4) 452-474 [in Chinese].
- Ginn, W. L., T. C. Lee and K. Y. Chan, 2010: Past and future changes in the climate of Hong Kong. *Acta Meteor. Sinica*, 24(2), 163-175.
- Guangdong Climate Center (Internal reference): 氣候變化對廣東極端事件的物理風險和影響評估, 21pp [in Chinese].
- IPCC 2007: Climate Change 2007: The Physical Basis. Contribution of the Working Group I to the Fourth Assessment Report of the Intergovernmental Panel on Climate Change. Solomon, S., D. Qin, M. Manning, Z. Chen, M. Marquis, K. B. Averyt, M. Tignor and H. L. Miller (eds.). Cambridge University Press, Cambridge, United Kingdom, and New York, NY, USA, 996pp.
- Karl, T. R., P. D. Jones, R. W. Knight, G. Kukla, N. Plummer, V. Razuvayev, K. P. Gallo, J. Lindsay, R. J. Charlson, and T. C. Peterson, 1993: A new perspective on recent global warming asymmetric trends of daily maximum and minimum temperature. *Bull. Amer. Meteor. Soc.*, 74, 1007-1023.
- Leung, Y. K., M. C. Wu, K. K. Yeung and W. M. Leung, 2007: Temperature projections in Hong Kong based on IPCC Fourth Assessment Report. *Bull. HK Met. Soc.*, 17, 13-22
- Leung, Y. K. and C. Y. Lam, 2008: Visibility impairment in Hong Kong- a wind attribution analysis. *Bull. HK Met. Soc.*, 18, 33-48.
- Li, W., Y. Du, G. Wang, M. Wu and Y. Xu, 2009: Urbanization effects on precipitation over the Pearl River Delta based on satellite data. *Chinese Journal of Atmos. Sci.* 33(6) 1259-1266 [in Chinese].
- Mok, H. Y., Y. K. Leung, T. C. Lee, and M. C. Wu, 2006: Regional rainfall characteristics of Hong Kong over the past 50 years. Conference on "Changing Geography in a Diversified World", Hong Kong Baptist University, Hong Kong, China, 1-3 June 2006. Hong Kong Observatory Reprint No. 646.
- Tang, I. M., 2008a: 澳門氣候變化狀況，澳門地球物理暨氣象局 (for internal use only), 17pp [in Chinese].
- Tang, I. M., 2008b: 澳門氣候的變化趨勢預測，澳門地球物理暨氣象局 (for internal use only), 20pp [in Chinese].
- Wong, M. C., H. Y. Mok and T. C. Lee, 2010: Observed changes in extreme weather indices in Hong Kong. *Int. J. Climatol.*, Published online in October 2010, DOI: 10.1002/joc.2238, 12pp.
- Wu, H. and Y. Du, 2010a: Asymmetric changes of extreme temperature in South China in 1961-2008. *Chinese Journal of Ecology* 29(11) 2241-2248 [in Chinese].
- Wu, H. and Y. Du, 2010b: Climatic characteristics of cold waves in South China in the period of 1961-2008. *Adv. Clim. Change Res.*, 6(3), 192-197 [in Chinese].
- Wu, H., Y. Du, Z. Chen, W. Pan and H. Duan, 2011a: Climatic variations of wet days and rain intensity in south China. *J. Trop. Met.*, 27(6), 877-888 [in Chinese].
- Wu, H., Y. Du, J. He and W. Pan, 2011b: Climatic characteristics and variations of hazy days and foggy days in south China. *Meteorological Monthly*, 37(5) 607-614 [in Chinese].
- Wu, H., Y. Du and W. Pan, 2011c: The change and characteristics of sunshine duration in the recent 48 years in south China. *Acta Scientiarum Naturalium Universitatis Sunyatseni*, 50(6), 18-23. [in Chinese].
- Zhou, K. M., R. E. Dickinson Y, H. Tian *et al.*, 2004: Evidence for a significant urbanization effect on climate in China. *Proceedings of the National Academy of Sciences*, 101(26), 9540-9544.

	Global	Guangdong	Macao	Hong Kong
Period	1906-2005		1901-2007	1885-2008
Rate of temperature increase (°C/decade)	0.07 ^[1]		0.07 ^[3]	0.12 ^[5]
Period	1956-2005	1961-2007	1952-2007	1947-2008
Rate of temperature increase (°C/decade)	0.13 ^[1]	0.21 ^[2]	0.10 ^[3]	0.16 ^[5]
Period			1971-2007	1979-2008
Rate of temperature increase (°C/decade)			0.34 ^[4]	0.27 ^[5]

[1]: IPCC (2007)

[2]: Composing Team for Assessment Report on Climate Change of Guangdong (2007)

[3]: Fong *et al.* (2009)

[4]: Tang (2008a)

[5]: Ginn *et al.* (2010)

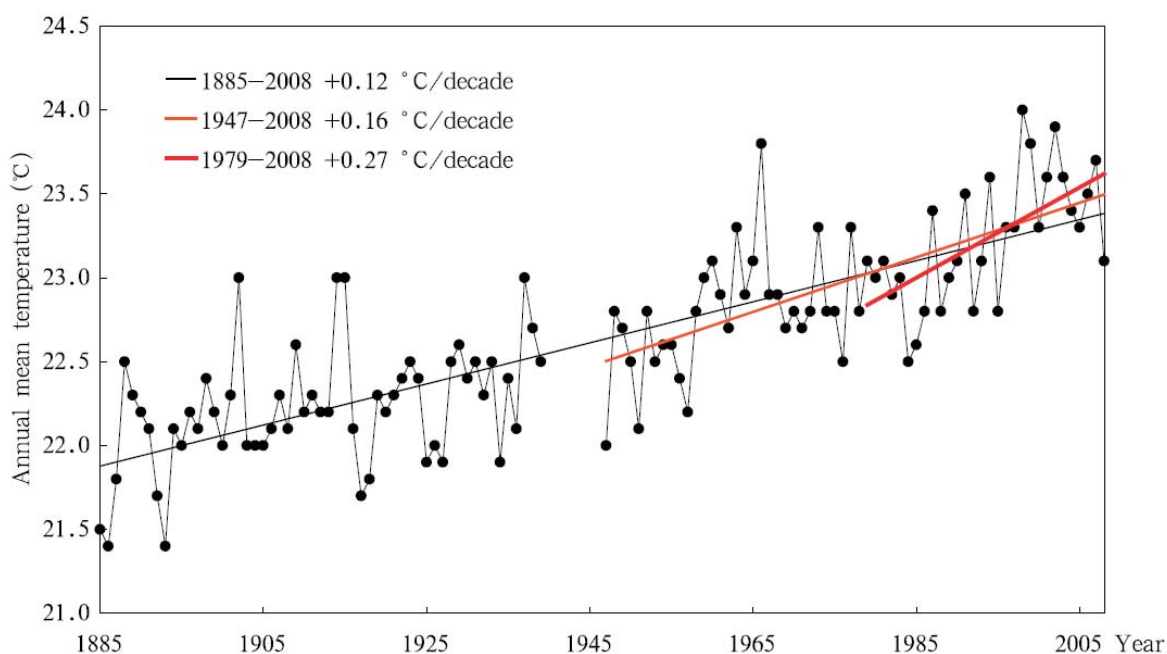


Figure 1 Annual mean temperature recorded at the Hong Kong Observatory headquarters (1885-2008). Data are not available from 1940 to 1946 due to World War II. Black line represents the linear trend of 1885-2008. Thin (thick) red line represents the linear trend during 1947-2008 (1979-2008). Source: Ginn *et al.* (2010).

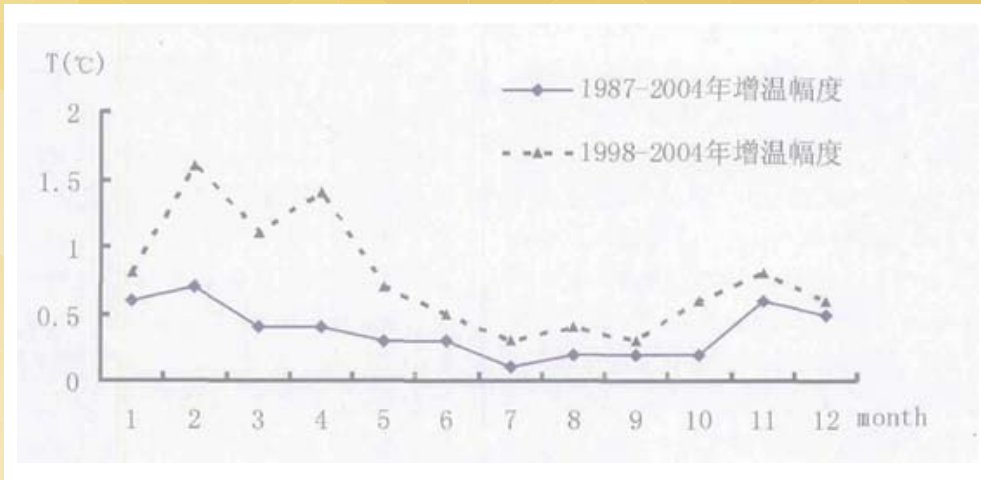


Figure 2 Monthly surface air temperature increase of Guangdong in 1987-2004 (solid line) and 1998-2004 (dashed line) relative to the average of 1971-2000. Source: Chen et al. (2006).

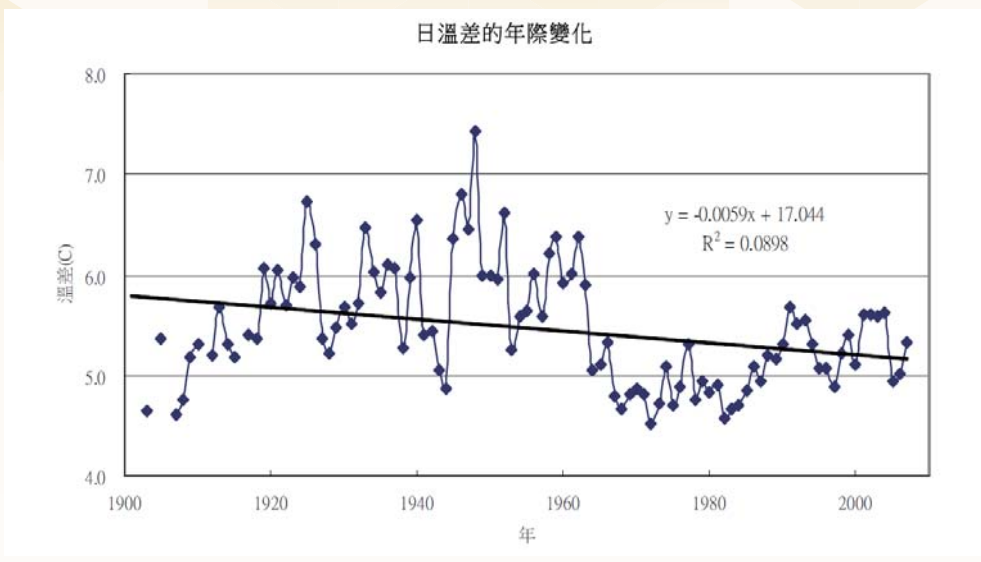


Figure 3 Annual average diurnal temperature range of Macao in 1901-2007. The black line indicates the linear trend. Source: Tang (2008a).

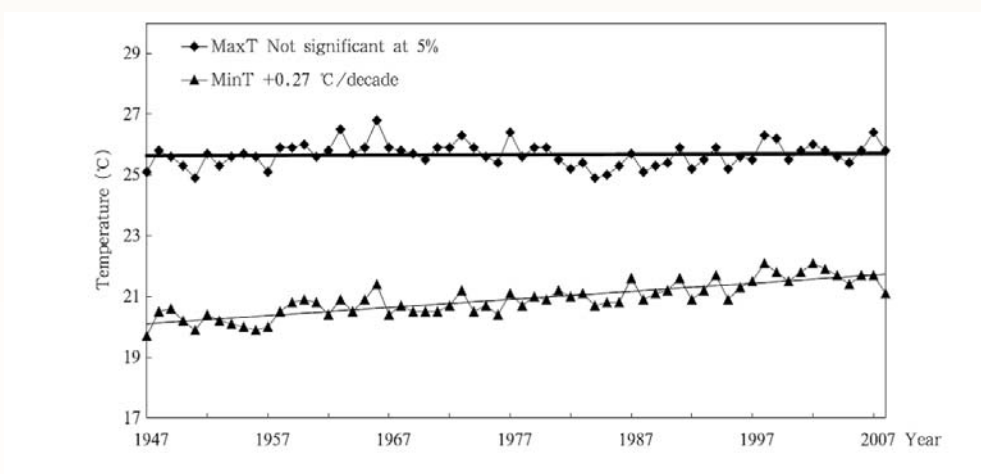


Figure 4 Annual average daily maximum temperature and annual average daily minimum temperature recorded at the Hong Kong Observatory headquarters in 1947-2008. Source: Ginn et al. (2010).

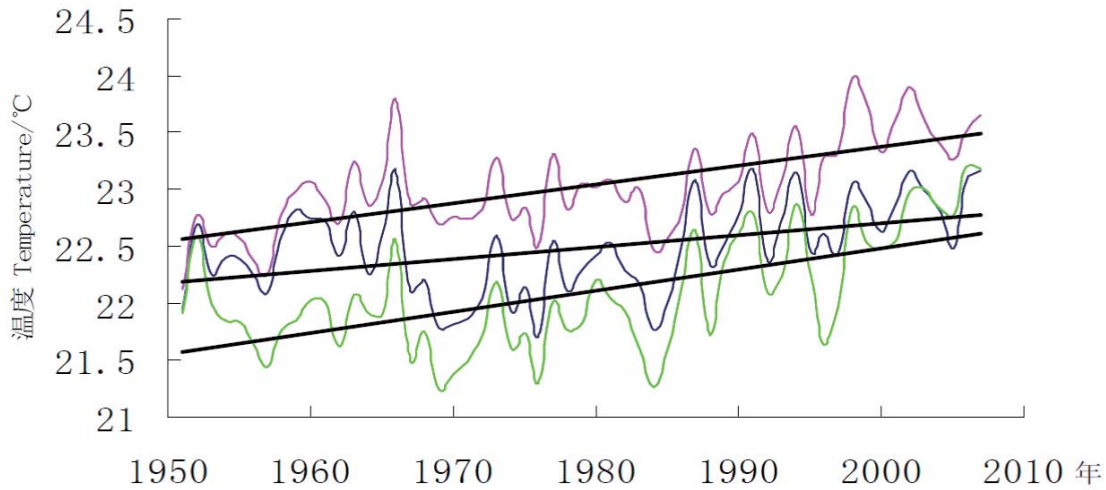
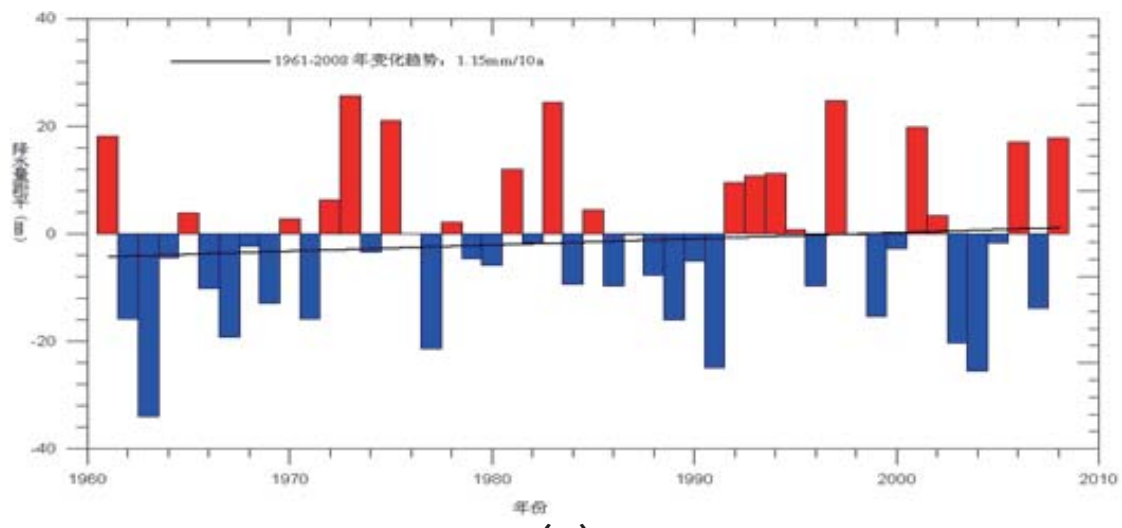
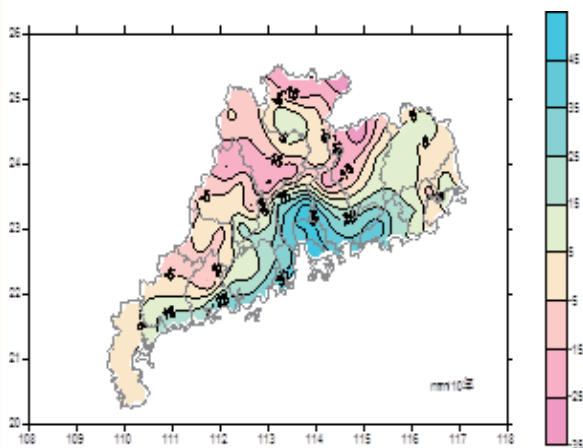


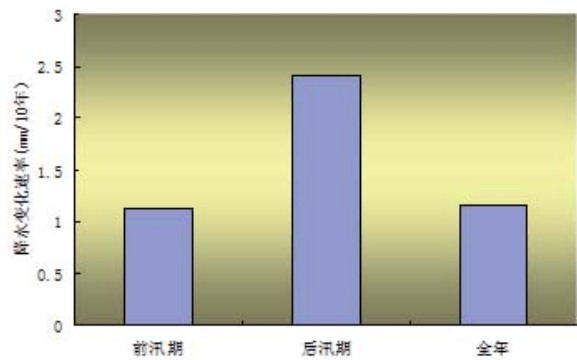
Figure 5 Annual mean temperatures of Hong Kong (red), Guangzhou (green), and Macao (blue) in 1951-2007. The thick black lines indicate the linear trends. Source: Fong et al. (2009).



(a)



(b)



(c)

Figure 6 (a) Annual rainfall anomalies of Guangdong during 1960-2009. Black line represents the linear trend. (b) Spatial variation of rainfall trend (mm/decade) over Guangdong in 1960-2009. (c) Rainfall trend (mm/decade) of Guangdong in the "pre-flooding" period (left), the "post-flooding" period (middle), and annual terms (right). Source: Guangdong Climate Center.

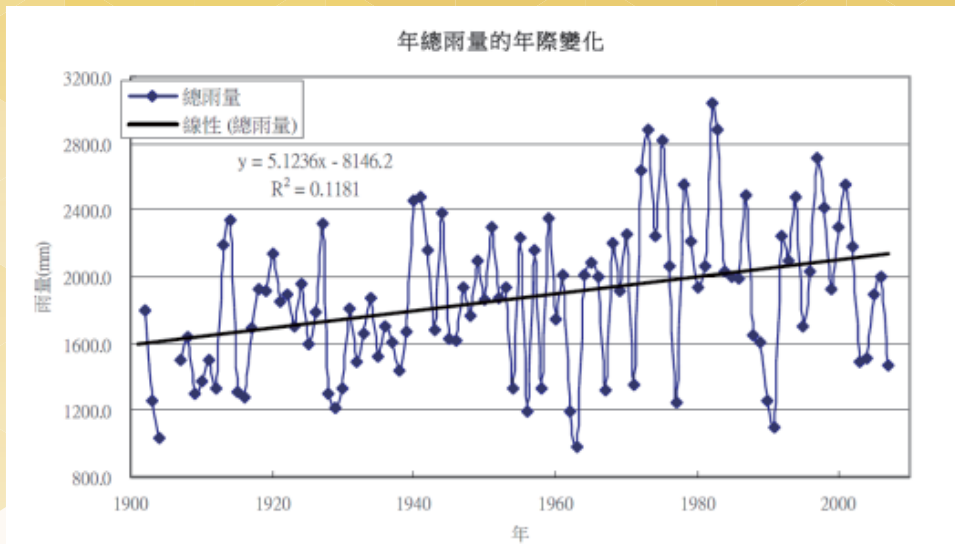


Figure 7 Annual rainfall in Macao during 1901-2007. The black line indicates the linear trend. Source: Tang (2008a).

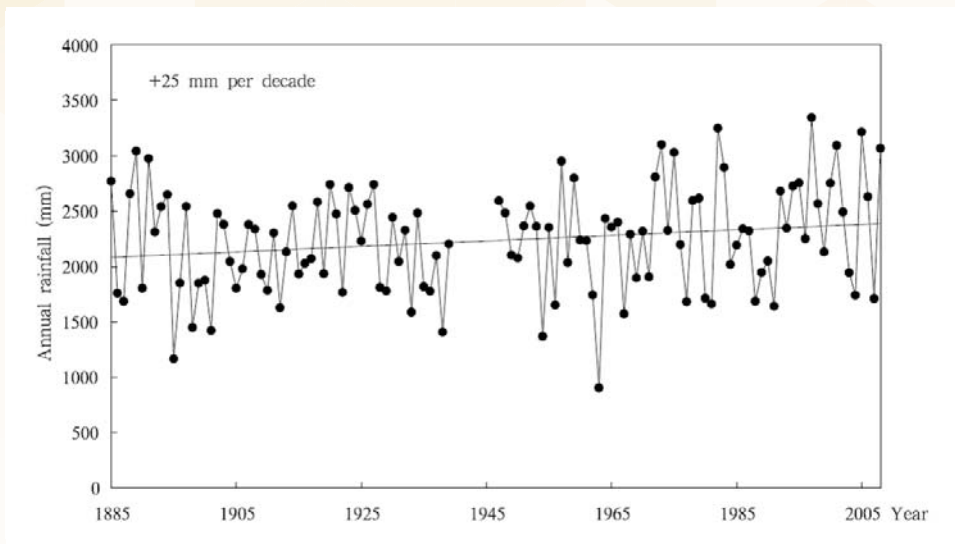


Figure 8 Annual rainfall recorded at the Hong Kong Observatory headquarters (1885-2008). Data are not available from 1940 to 1946 due to World War II. Source: Ginn et al. (2010).

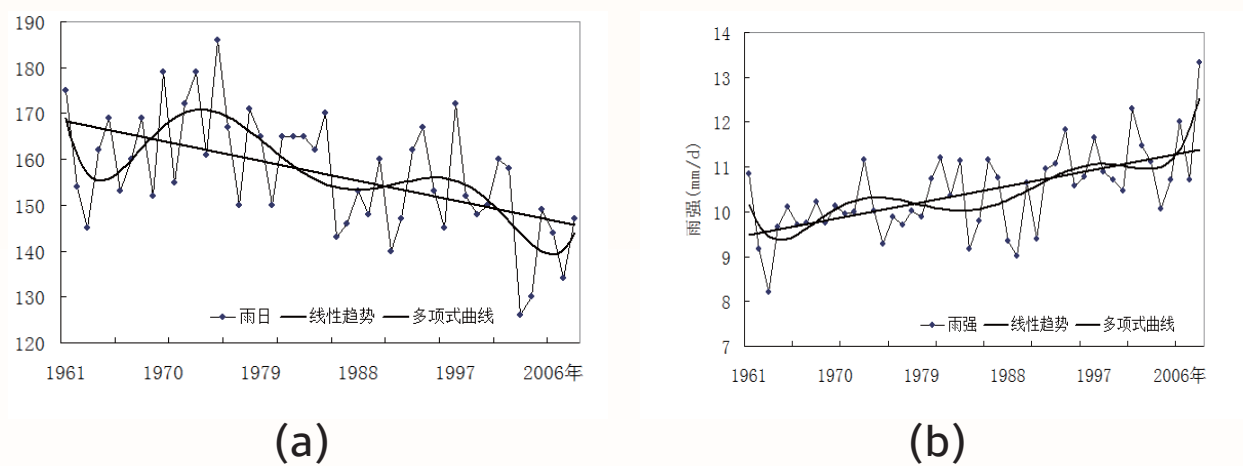


Figure 9 (a) Annual number of rain days and (b) average rainfall intensity in southern China during 1961-2008. Source: Wu et al. (2011a)

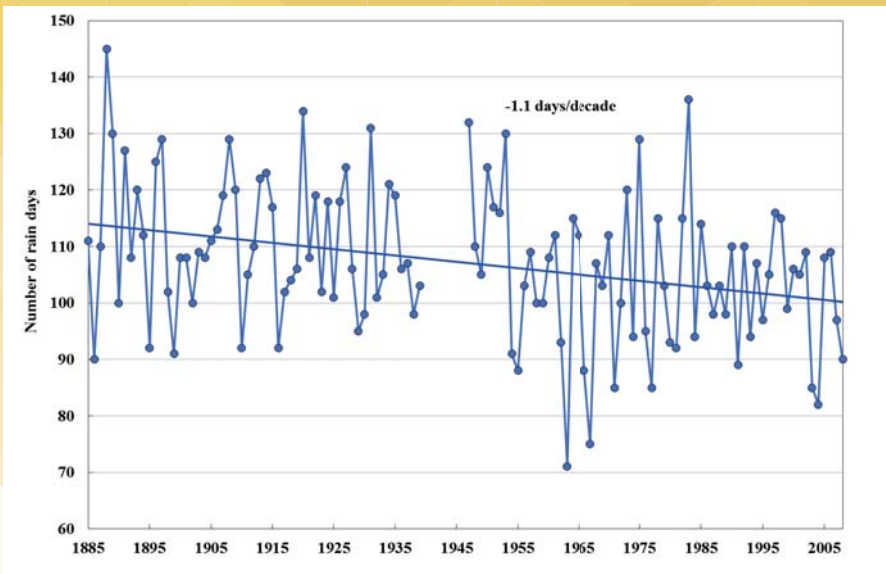


Figure 10 Number of rain days in Hong Kong during 1885-2008. The solid blue line indicates the linear trend.

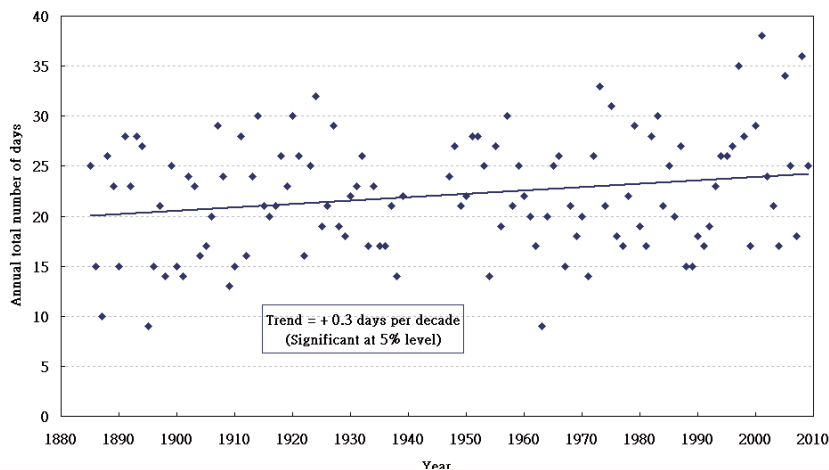


Figure 11 Number of days with daily rainfall ≥ 30 mm in Hong Kong during 1885-2010. The solid blue line indicates the linear trend.

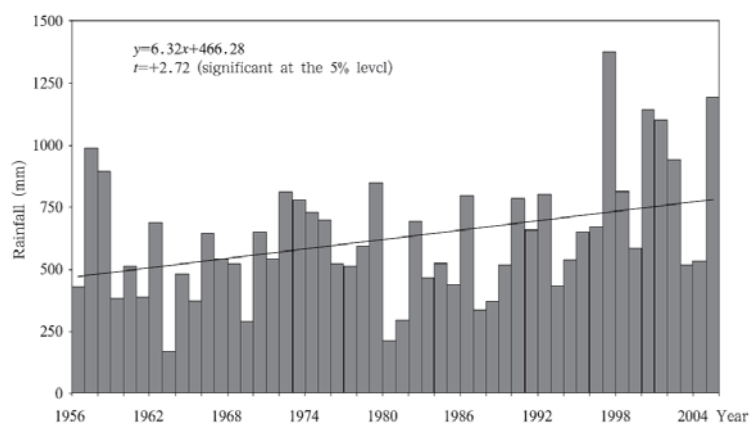
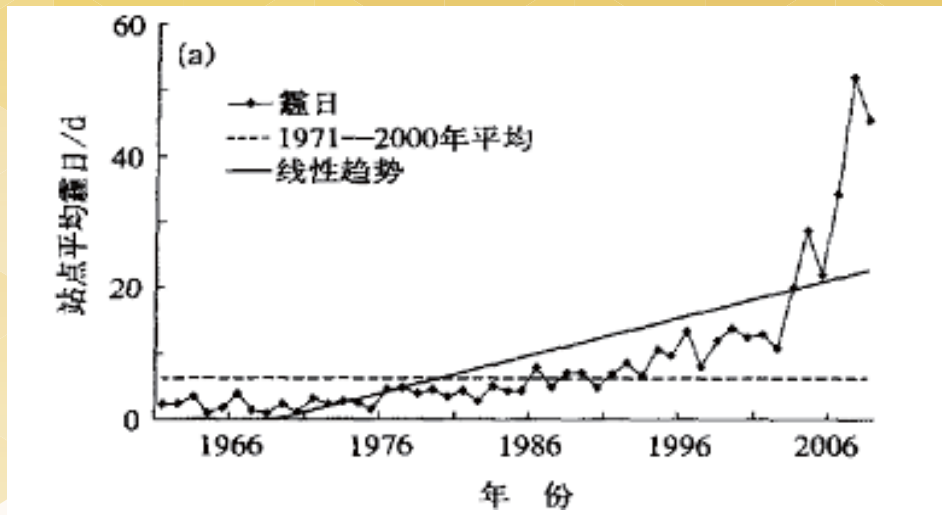
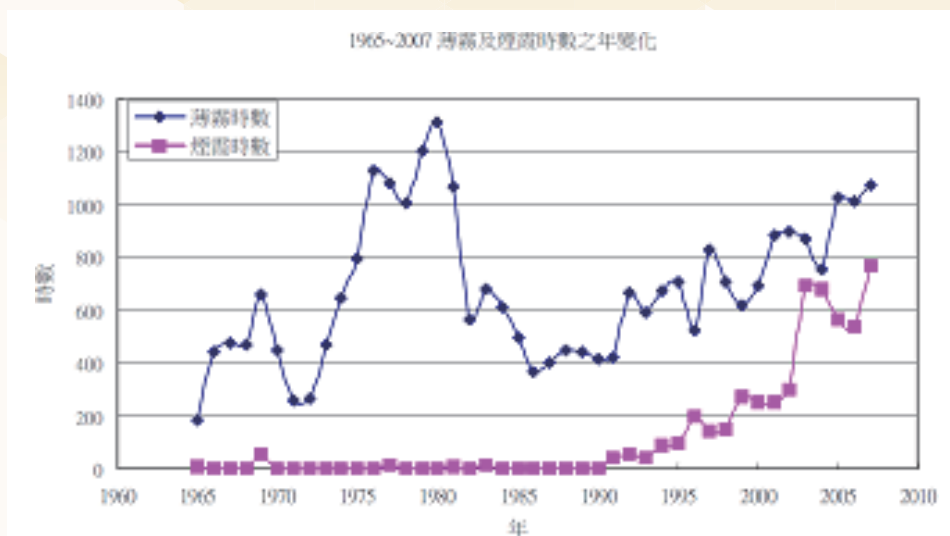


Figure 12 Time series showing the annual rainfall difference between the urban region and offshore region (urban minus offshore). The solid line indicates the linear trend during 1956-2005. Source: Mok et al. (2006).

(a)



(b)



(c)

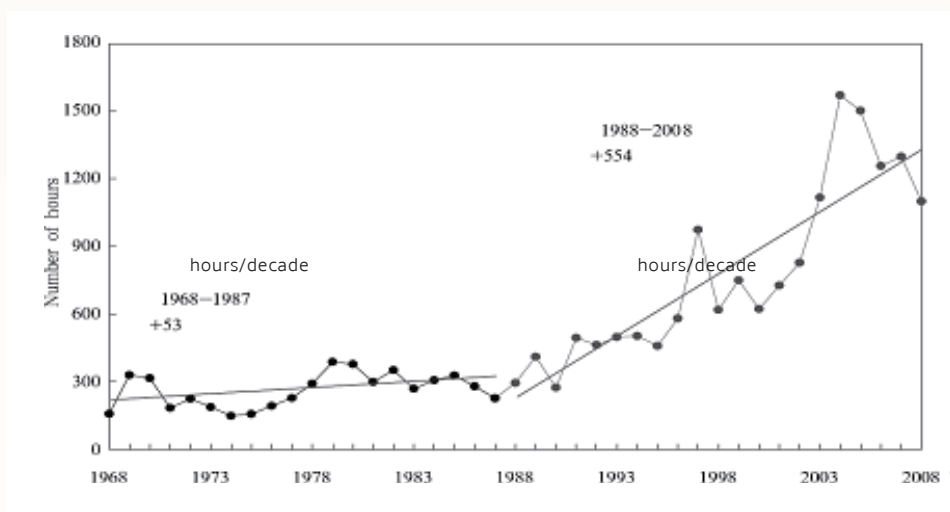


Figure 13 (a) Number of hazy days in southern China during 1961-2008. The solid line indicates the linear trend while the dashed line indicates the 1981-2000 average. Source: Wu et al. (2011b). (b) Number of misty days (blue) and hazy days (red) in Macao during 1965-2007. Source: Tang (2008a). (c) Annual number of hours with visibility at the HKO headquarters below 8 km during 1968-2008 (relative humidity below 95% and excluding cases of rain, mist, or fog). Source: Ginn et al. (2010).

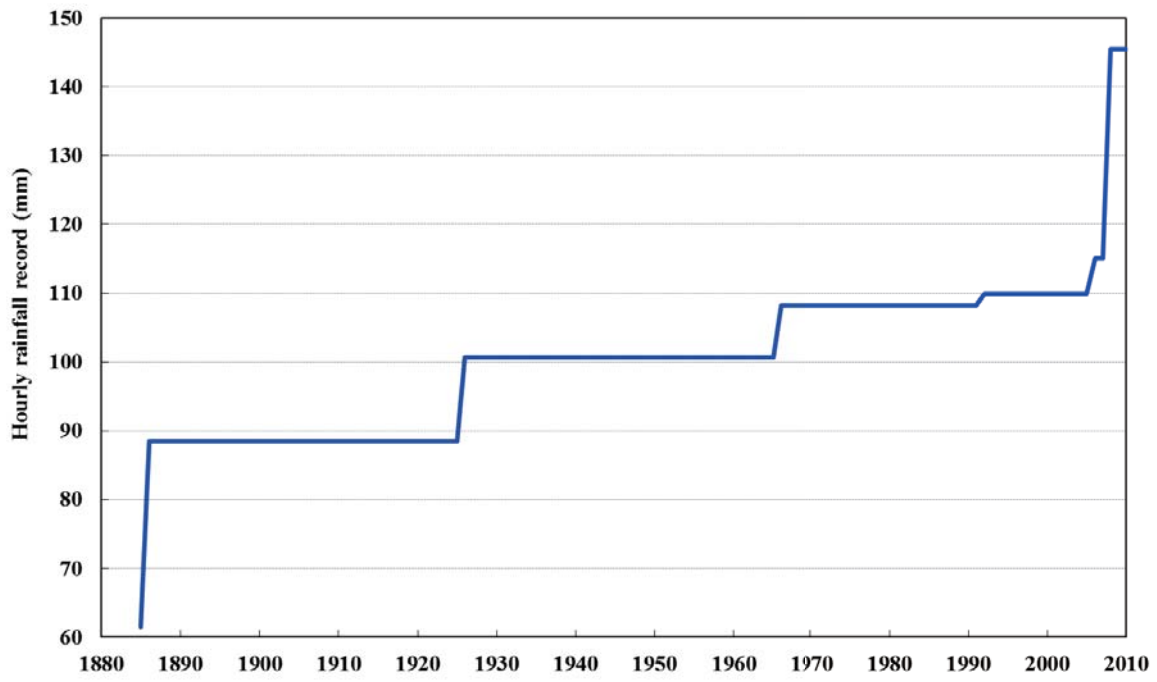


Figure 14 Hourly rainfall record at the HKO headquarters during 1885-2010.

SOCIETY EVENT

Popular Science Lecture Series



推廣活動
EXTENSION ACTIVITIES

普及科學講座
Popular Science Lectures

「海天與地 - 生活氣象縱橫談」講座系列
"Ocean, Sky and Earth - Meteorology in Our Life Daily" Lecture Series

從太空到天空，從海洋到陸地，氣象與我們的生活息息相關。在這套普及科學講座系列裡，我們邀請了在航空氣象、太空天氣、海洋氣象、及生物氣象四個方面的專家，為大眾講解天氣和氣候怎樣從不同的途徑影響我們日常的生活。透過這些講座，希望大家對氣象有更深入的了解，從而可以在日常生活中有效地應用各種氣象資訊。

題目及講者 Topic and Speaker	日期 Date	時間 Time
航空天氣 Aviation Weather 李智明先生 (香港天文台台長、香港氣象學會會長及世界氣象組織「航空氣象學委員會」主席)	13.10.2012 (星期六 Saturday)	10:00am - 11:00am
太空天氣預報對現代生活的影響 Space Weather Forecast and its Impact on Modern Living 陳炳林教授 (香港科技大學數學系)	13.10.2012 (星期六 Saturday)	11:00am - 12:00noon
海洋與氣候 Ocean and Climate 周文教授 (香港城市大學能源與環境學院)	13.10.2012 (星期六 Saturday)	2:00pm - 3:00pm
天氣與健康 Weather and Health 陳英潔教授 (香港中文大學醫學院)	13.10.2012 (星期六 Saturday)	3:00pm - 4:00pm

* 所有講座均免費入場

語言：粵語 (conducted in Cantonese)
地點：香港科學館演講廳

免費活動，即場入座，座位先到先得。
查詢電話：2732 3223 (星期一至五：上午九時至下午一時；下午二時至五時，公眾假期除外)
Free admission on a first come, first served basis.
Enquiries: 2732 3223 (Mon to Fri: 9:00a.m. to 1:00p.m., 2:00p.m. to 5:00p.m., except public holidays)

14

COLOUR FIGURES

Mascot Design Competition for Primary School Students

香港氣象學會主辦、香港美術教育協會協辦、香港天文台協辦

「天氣吉祥物」

平面設計比賽結果 - (初級組)

由評判團選出冠、亞、季軍及優異獎共 7 名，結果如下：

名次	姓名	學校
冠軍：	陳芷遙	香港浸信會聯會小學
亞軍：	彭展晴	香港浸信會聯會小學
	何彥青	嘉諾撒聖方濟各學校
季軍：	林澄儀	Yellow House Children' s Art Programme
	莊子燁	北角循道學校 (小學)
優異： (排名不分先後)	陳熹緩	香港浸信會聯會小學
	林卓盈	Yellow House Children' s Art Programme

冠軍



陳芷遙 (香港浸信會聯會小學)

亞軍



何彥青 - 嘉諾撒聖方濟各學校



彭展晴 - 香港浸信會聯會小學

季軍



莊子燁 - 北角循道學校 (小學)



林澄儀 - Yellow House Children's Art Programme

優異



陳熹緩 - 香港浸信會聯會小學



林卓盈 - Yellow House Children's Art Programme

香港氣象學會主辦、香港美術教育協會協辦、香港天文台協辦
「天氣吉祥物」

平面設計比賽結果 - (高級組)

由評判團選出冠、亞、季軍及優異獎共 6 名，結果如下：

名次	姓名	學校
冠軍：	吳思諭	北角循道學校 (小學)
	譚詩蔚	香港浸信會聯會小學
亞軍：	楊凱晴	大埔舊墟公立學校
季軍：	黃悅然	香港浸信會聯會小學
優異： (排名不分先後)	布希敏	北角循道學校 (小學)
	蔡曉晴	香港浸信會聯會小學



冠軍



譚詩蔚 - 香港浸信會聯會小學



吳思諭 - 北角循道學校 (小學)



亞軍

季軍



楊凱晴 - 大埔舊墟公立學校



黃悅然 - 香港浸信會聯會小學



優異



布希敏 - 北角循道學校 (小學)



蔡曉晴 - 香港浸信會聯會小學



HONG KONG METEOROLOGICAL SOCIETY

Office Bearers:
(2012-2013)

Chairman
Mr. C.M. Shun

Vice Chairman
Dr. P.W. Li

Hon. Secretary
Mr. Terence Kung

Hon. Treasurer
Dr. David Lam

Executive Committee Members

Mr. William Cheng
Dr. K.S. Lam
Dr. C.N. Ng
Dr. Francis Tam

Mr. Clarence Fong
Dr. Alexis Lau
Dr. Edward Ng

INFORMATION FOR CONTRIBUTORS TO THE BULLETIN

Technical or research articles, as well as reviews and correspondence of a topical nature are welcome. In general contributions should be short, although exceptions may be made by prior arrangement and at the sole discretion of the Editorial Board. Copyright of material submitted for publication remains that of the author(s). However, any previous, current, or anticipated future use of such material by the author must be stated at the time of submission. All existing copyright materials to be published must be cleared by the contributor(s) prior to submission.

Manuscripts must be accurate and preferably in the form of a diskette containing an electronic version in one of the common word processing formats. WORD is preferred but others are also acceptable. Whether or not an electronic version is submitted, two complete manuscript copies of the articles should be submitted. These should be preceded by a cover page stating the title of the article, the full name(s) of the author(s), identification data for each author (position and institution or other affiliation and complete mailing address). An abstract of about 150 words should be included. Manuscripts should be double-spaced, including references, single-side only on A4 size paper with a 2.5 cm margin on all sides, and be numbered serially. All references should be arranged in alphabetical and, for the same author, chronological order. In the text they should be placed in brackets as (Author'(s) name(s), date). In the reference list at the end the Author'(s) name(s) and initials followed by the date and title of the work. If the work is a book this should be followed by the publisher's name, place of publication and number of pages; or, if a journal article, by the title of the periodical, volume and page numbers.

Submission of electronic versions of illustrations is encouraged. Originals of any hardcopy illustrations submitted should be in black on tracing material or smooth white paper, with a line weight suitable for any intended reduction from the original submitted size. Monochrome photographs should be clear with good contrasts. Colour photographs are also accepted by prior arrangement with the Editorial Board. Originals of all illustrations should be numbered consecutively and should be clearly identified with the author(s) name(s) on the back. A complete list of captions printed on a separate sheet of paper.

All submitted material is accepted for publication subject to peer review. The principal author will be sent comments from reviewers for response, if necessary, prior to final acceptance of the paper for publication. After acceptance the principal author will, in due course, be sent proofs for checking prior to publication. Only corrections and minor amendments will be accepted at this stage. The Society is unable to provide authors with free offprints of items published in the Bulletin, but may be able to obtain quotations from the printer on behalf of authors who express, at the time of submission of proofs, a desire to purchase a specified number of offprints.

Enquiries and all correspondence should be addressed to the Editor-in-Chief, Hong Kong Meteorological Society Bulletin, c/o Hong Kong Observatory, 134A, Nathan Road, Kowloon, Hong Kong.

